UNIVERSITY OF TRENTO - Italy

DEPARTMENT OF PHYSICS
Nanoscience Laboratory

Novel materials and optical waveguide systems for silicon photonics

Romain Guider

December 2009

Supervisor

Professor Lorenzo Pavesi

A mon grand-père et ma famille,

Acknowledgments

First I would like to express my complete gratitude towards Professor Lorenzo Pavesi, my supervisor and the head of the Silicon Photonic group at University of Trento. He has given me the possibility to get the PhD Thesis in his group, and he gave me constant support and help. I learn a lot during these three years and thank him to have supported “jojo” during these three years.

I would like to thanks specially three people of the Nanophotonics group for their precious help in my research and their friendship: Dani, Alessandro P. and Paolo.

I am grateful to the Polycernet project and the European Union, which supported financially this project.

I would like also to thank Dr. Nicola Daldosso which was always open to help and teach me the fundaments of guided optics.

In Trento, I have a lot of people to thank, especially Nikola, Mattia and Alessandro M., which now are more than friends, but also Tania, Massimo, Evelyne, Oleksiy, Sylvia, Arshan, the Chinese band, Marco, Manga and all the others.

I would like also to make a special thank to Aylin who really support me during these three years and would like to say to her, now you’re free.

In France, I would like to thank all my friends Karine, Desch, Tiche, Bab, Jay, Toc, Will, Lolo but also Sebastien and Rémi.

In Trento, I do not forget all my friends, Yoann, Aleksandar, Jasna, Silviya, Loredana, Ivana, Paola, Ludo and Iryna.

Final but not the least, I would like to thank heartily my mother, my father, my two brothers and my five dogs. They made unforgettable every minute of my life.

Table of contents

Chapter one: Introduction to Silicon Photonics

1.1 Photonics and Nanophotonics …………………………………………………………..p1

1.2 Role of Silicon in the photonics field...p2

1.3 Overview of the thesis and collaborations……………………………………………p4

References…………………………………………………………………………...p8

Chapter two: Silicon Oxycarbide thin films: preparation, surface properties and photoluminescence measurements

2.1 Introduction………………………………………………………………………...p9

2.2 Sol-gel method and synthesis of SiOC thin films……………………………………...p10

2.3 Characterisation of the films

2.3.a Surface properties……………………………………………………………p12

2.3.b Absorption coefficient measurements………………………………………..p14

2.4 Optical Characterisation

2.4.a Photoluminescence of SiOC samples……………………………………...p16

2.5 Effects of Boron addition on SiOC thin films

2.5.a Surface properties……………………………………………………………p24

2.5.b Photoluminescence of Boron added SiOC…………………………………...p25

2.6 External Quantum Efficiency of SiOC samples………………………………………p28

2.7 Conclusion………………………………………………………………………….p35

References…………………………………………………………………………….p37

Chapter three: Silicon on Insulator waveguides and building blocks

3.1 Sample processing…………………………………………………………………..p41

3.2 Experimental set-up

3.2.a Coupling system…………………………………………………...………....p43

3.2.b Collection system…………………………………………………………….p45

3.3 Waveguide losses

3.3.a The Cut-back Method………………………………………………………..p46

3.3.b Propagation losses of SOI waveguides………………………………………p47

3.4 Basics components-losses characterization

3.4.a Splitters 1x2

3.4.a.1 Y-junction…………………………………………………………..p48

3.4.a.2 Multimode Interferometer (MMI)…………………………………p50

3.4.b Splitters 1x8…………………………………………………………………p52

3.4.c Bends…………………………………………………………………………p52

3.5 Conclusion………………………………………………………………………..p54

References………………………………………………………………………………p55

Chapter four: NanoSi slot waveguides

4.1 Theoretical approach of the slot waveguides………………………………………..p58

4.2 Processing of Slot waveguides

4.2.a Vertical Slot waveguides………………………………………………...…...p60

4.2.b Horizontal Slot waveguides…………………………………………………p61

4.3 Waveguide losses

4.3.a Propagation Losses on Vertical slot waveguides……………………………p62

4.3.b Propagation Losses on horizontal slot waveguides…………………...……..p64

4.4 Ring Resonator

4.4.a Theory of ring resonator……………………………………………………...p67

4.4.b Free Spectral Range…………………………………………………………p72

4.4.c Quality Factor of a ring resonator……………………………………………p72

4.4.d Experimental results…………………………………………………………p73

4.4.e Effect of Si-nc in ring resonators…………………………………………….p77

4.4.f Group index …………………………………………………………………p77

4.5 Double ring resonators

4.5.a Experimental results…………………………………………………………p79

4.6 Slow light effect in Slot waveguides

4.6.a Slow light in vertical slot waveguide………………………………………..….p81

4.6.b Slow light in horizontal slot waveguides……………………………...…...p82

4.7 Conclusion…………………………………………………………………..…………p85

References…………………………………………………………………………...……...p86

Chapter five: Silicon on Insulator coupled-resonators measurements

5.1 Serially coupled ring resonator theory

5.1.a Add-Drop configuration…………………………………………………..…….p89
5.1.b Serially double coupled-ring………………………………………………....p93
5.2 Electromagnetically-induced transparency (EIT) and Coupled Resonator Induced Transparency (CRIT)
5.2.a EIT in an atomic configuration…………………….……………………...p95
5.2.b Coupled resonators induced transparency…….……………………..……p96
5.3 Ring and Disk Resonators……………………………………………………………..p97
5.4 Experimental Results
5.4.a Sample Description……………………………………………………………..p98
5.4.b Ring/disk comparison……………………………………………………..…p98
5.4.c Coupled Disks resonators……………………………………………...…....p100
5.4.d CRIT in a double-disk resonators structure………………………………...p104
5.5 Side-Coupled Integrated Spaced-Sequence of Resonators (SCISSOR)
5.5.a Description and principle of a SCISSOR…………………………………...p107
5.5.a Single channel SCISSOR…………………………………………………...p109
5.5.b Double Channel SCISSOR…………………………………………………p111
5.6 Top-view system
5.6.a Description of the Set-up…………………………………………………...p114
5.6.b Experimental results………………………………………………………...p115
5.6.c Effects of structural disorders on the EIT-like peaks………………………p116
5.7 Conclusion……………………………………………………………………………p117
References……………………………………………………………………………...p119

General Conclusion…………………………………………………………………….p121

Appendix……………………………………………………………………………..p123

Publications…………………………………………………………………………p127

Chapter one

Introduction to Silicon photonics

Silicon photonics is an emerging and very interesting field of research and technology. In this chapter, we will introduce the concept of photonics and describe the role of Silicon in this field. We will take a look at the prospective in the field and, finally, give an overview of the plan of the thesis.

1.1 Photonics and Nanophotonics

Photonics is about the study of the light, from generation to transmission, manipulation, control and detection of photons. When we consider electromagnetic waves interacting with a medium whose features are of the order of the wavelength, the electromagnetic field feels the photonic structure in all its details. In this case, the photonic effects become very interesting, because they enable to conceive physical systems to mold the flow of the electromagnetic field itself [1].

The study of photonic devices have shown in the last fifty years very interesting progress, leading to many crucial discoveries about light generation, processing and detection. All these discoveries have dramatically changed the vision on how to exploit light. For example, concerning the wireless networks, the invention of laser sources and optical fibers allows the transfer of a huge mass of data by modulating optical signals propagating in optical fibers. Until 1990, the bit rate of an optical communication system was limited to 10 Gb/s due to dispersive and non linear effects occurring in optical fibers and the limits set by the regeneration of transmitted signals in the electrical domain (Fig.1.1). In recent years, the interest in Integrated Optical Technologies has grown rapidly and considerable advantages are allowed by Photonics over its discrete, microoptical and fiber-based counterparts, in terms of compactness, reliability, performance, and significant cost reduction. A very significant increase in transmission capacity of optical telecommunication systems has been achieved with the introduction of optical amplifiers, with which optical signals are amplified in the optical domain, and multiplexing techniques such as Wavelength Division Multiplexing (WDM) and Optical Time Division Multiplexing (OTDM) permit a very significant increase in the transmission capacity as well up to some Terabit by seconds.

But one of the most important reasons of the success of photonic is the fact that it's a very good alternative to electronic. If we take a look at the sate of the art of integrated electronics, the length of a gate in a single transistor is around 42nm. The problem is, as their number in a chipset is around hundred millions, the length to connect all these elements together is of the order of ten kilometers. This distance can represent a dissipative power of around one kilowatt. If we think that, in the next years, this power will continue to grow, a possible solution to this problem is to use photons to transport the information in our system. There are multiples advantages to this, from the elimination of the heating powers and the electromagnetic interference to the information capacity, which is more than six orders of magnitudes in case of the optical fibers compared with coaxial cables (Fig.1.1).

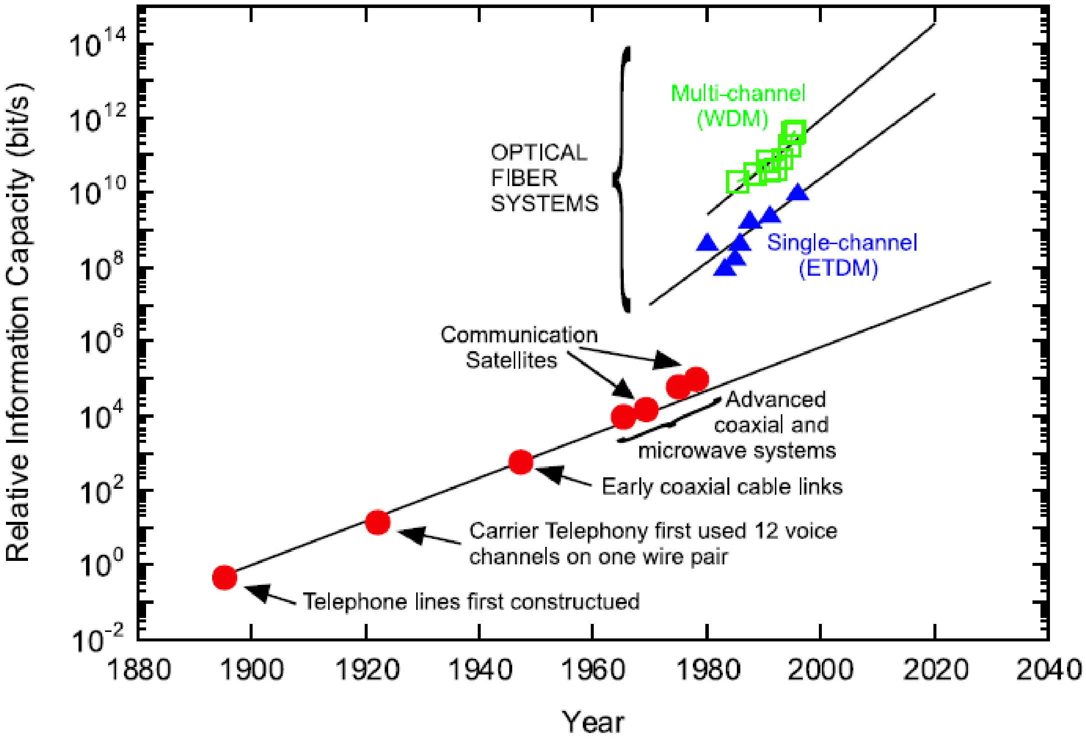

Fig. 1.1. Information capacity in function of the year (Francesco Riboli Thesis 2005)

In the case of telecommunications, the characteristic length scales of the devices are at submicron level, for an application with infrared light signals. Such photonic devices are the fundamental components for integrated optic. In this case, we will not speak any more about Photonics, but about *Nanophotonics*.

1.2 Role of Silicon in the photonic field

Today, most optical components are made from III–V-based compounds, like indium phosphide (InP) or gallium arsenide (GaAs), and are often custom-made and assembled from discrete components. The net result of all this is that these optical devices are relatively expensive. Silicon photonics (or better CMOS Photonics) is a viable way to tackle the problem by developing a small number of integration technologies with a high level of functionality that can address a broad range of applications.

The Si band gap (about 1.1 eV) is such that silicon is transparent to typical wavelengths of optical communications (1.3-1.6 μm). Moreover, Si refractive index is about 3.5 and the Si/SiO_2 system has a very high refractive index contrast. The high Si refractive index is an advantage for realizing strong guiding structures (such as waveguides), very sharp waveguide bends, photonic band gap materials and, at the end, it determines the physical dimensions of the whole integrated photonic device. The origins of Silicon Photonics date back to the 80’s and have been pioneered by Soref [2, 3]. In these last years, very interesting research on the field have been achieved [4-7]. If we take a look at the industrial field in the world of Silicon Photonics, we can observe that globally, the companies used two different approaches of integration. In the first case, Si was only used to channel the light signal. This technology, with waveguide dimensions typically in the μm range, is actually used by several companies, like Kotura and INTEL. The second approach is to integrate silicon, germanium and III-V semiconductors together. Luxtera Inc. used this hybrid technology to create recently a monolithic optoelectronic Optical Active Cable.

Fig. 1.2 represents a possible “All Silicon” integrated optical circuit. This structure should be able to produce, guide and detect optical signals. We noted that the light is generated by a continuum Si laser based on Raman effect [8]. In this laser, the role of the photon battery is played by a III-IV semiconductor laser. The SiGe detector has for objective to monitor the input signal. The role of the modulator based on the Mach-Zender interferometer is to encode the data into the optical signal. The signal is then directed to an amplifier realized with erbium-doped silicon waveguide [9]. The amplified digital signal is then manipulated by Si-based photonic crystal components and, finally, it is addressed to a fiber optical line by DWDMs (Dense Wavelength Division Multiplexer/Demultiplexer) components. The photonic circuit is complemented by power splitters and combiners, bends and straight waveguides, all Silicon-based. This is the state of the art for a photonic chip and the development perspectives are very large for all these components.

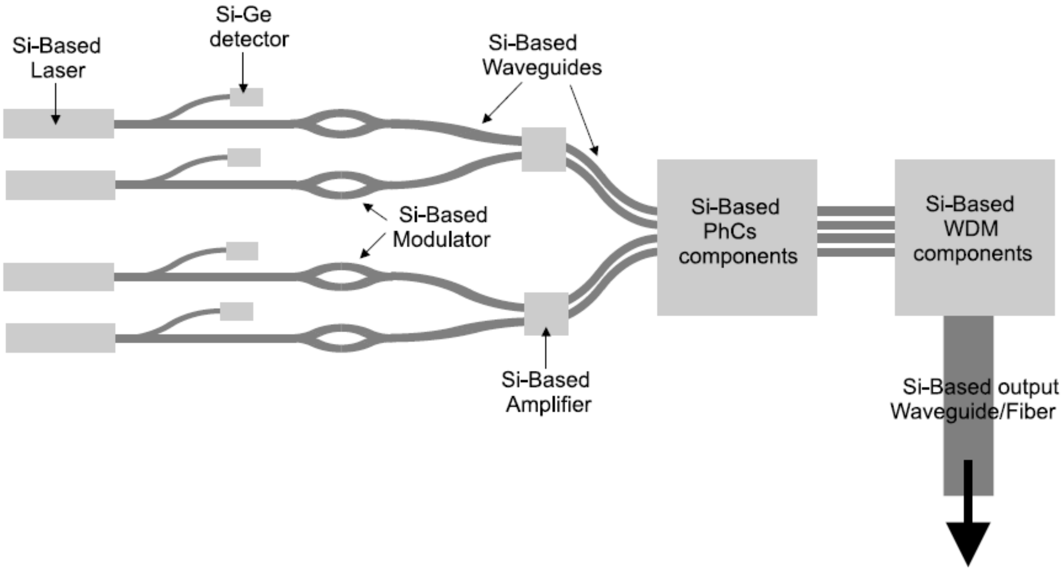

Figure 1.2. "All Silicon"-integrated optical circuit

On the other hand, silicon shows some disadvantages like the difficult coupling of light in the photonic device due to the high refractive index mismatch between Si itself and conventional SiO_2 based fibers or air, the untransparency to visible wavelengths and the transparency in the infrared makes detection difficult of typical telecom wavelengths and especially the indirect electronic band gap that makes silicon a bad light emitter,.

1.3 Overview of the thesis and Collaborations

My research in these three years has been mainly focused on the characterization of structural and optical properties of three kinds of Si-based materials and devices.

The first one is the study of SiOC thin films, carried within the TMR-POLYCERNET project financed by the European community. The scientific objective of this project is to create molecularly-tailored, nanostructured SiOC ceramics with unusual multifunctional properties, including photoluminescence. In addition these novel, polymer-derived ceramics, or PDCs, will have high resistance to oxidation, degradation, corrosion and deformation at temperatures above 1400^{o}C.

The aim of our work is focused on the optical characterization of PDCs. The PDCs are constituted from polymeric precursors which can be tailored and designed at the molecular level. These multifunctional properties are then carried over into the ceramic phase by self-assembly and controlled pyrolysis. Thus, these novel materials are apparently polymer-like in their structure (for example, they are seemingly amorphous but contain nanodomains) but have the chemical, mechanical and functional properties of high temperature ceramics. The photoluminescence will be the most important property that will be studied and optimized. The specific objective of this work is to optimize chemistry and processing to achieve bright emission and high external quantum efficiency in high-quality thin film.

In the second chapter of the thesis, starting from a brief description of SiOC glasses and the sol-gel process to introduce our work, we explained how the thin films were prepared and characterised. A study on the absorption coefficient of the films is reported, in order to compare it with results in literature of similar samples. The major part of this chapter was focalized on our work on the photoluminescence of the films. At high annealing temperature, we observed a very high yellow luminescence from the films, most notably due to the presence of SiC nanoclusters and C clusters in our samples. A well detailed discussion on the origin of the strong emission is reported. A study of the effects of Boron addition on the photoluminescence of our thin films was also effectuated and by comparing the evolution of the B-free (SiOC) and B-containing samples (SiBOC), the important role of boron in promoting the evolution of nanostructure in our thin films is described. Finally, to have an idea of the potential of our films, their external quantum efficiency (E.Q.E.) was measured. A detailed description of the measurement technique is reported and the results are compared with Si-nc samples whose EQE is well-known. Very high EQE were found for T^H films pyrolysed at 1200 °C (11.5 %) and T^HD^H2 films pyrolysed at 1200 °C (5%). These external quantum efficiency values are very promising and make SiOC a very interesting material for LED applications.

Another part of the work was devoted to the study of Si-based waveguides, and more particularly Silicon on Insulator (SOI) waveguides and Slot SOI waveguides. This work was carried out within the European project PHOLOGIC. The general objective of the PHOLOGIC project is to explore the mass-manufacturing feasibility of Silicon Nanocrystals inside SiO_2 matrix in terms of CMOS technology compatibility for a highly scalable photonic logic gate structure. A XOR gate was chosen as functional validation device. The third and fourth chapters of this thesis are dedicated to this work.

In the third chapter, we characterized various building blocks like splitters, MMI and bends made in Silicon on Insulator technology. The loss figures found for these building blocks were useful as a benchmark for further development of silicon microphotonics components and circuits on SOI platform like photonic crystals and ring resonators. In effect, the results of this chapter are basic to the development of the SCISSOR structures based on SOI technology, described in chapter five.

In the fourth chapter, we studied nano-Si slot waveguides. Horizontal slot waveguides filled with Si-nc have been realized and characterized in terms of propagation losses as a function of the layer deposition conditions (i.e. Si excess and annealing temperature). We were able to reach propagation losses as low as 3 dB/cm which is the best result reported so far for slot waveguides of very small width (50 nm). We presented also experimental results of resonant optical cavities such single and double ring resonators coupled to the horizontal slot waveguides with very high quality factors. The importance of this works relies on the fact that by optimizing the annealed SRSO (i.e. Si-nc) in the slot, we have significantly reduced the propagation losses and at the same time we can add new functionalities related to the Si-nc optical properties (i.e. light emission and/or non-linear optical effects). Finally, a one-dimensional photonic crystal structure based on horizontal slot waveguide with a photonic band gap around 1.55 μm has also been designed and optically characterized.

Finally, the last part of this thesis will be devoted to the characterization of Silicon on Insulators Multi-Resonators. This work is a continuation of the study of SOI building blocks described above, and was carried within the European project WADIMOS. The main goal of the WADIMOS project is to build a complex photonic interconnect layer incorporating multi-channel microsources, microdetectors and different advanced wavelength routing functions directly integrated with electronic driver circuits. Our work in this project is to test innovative optical waveguide division multiplexing circuits based on coupled ring resonators. In the last part of this thesis, we will characterize various coupled ring/disks resonators structures, from simple double coupled rings until eight coupled ring SCISSOR.

In the last chapter, we measured and compared the characteristic of the light propagation of different connection geometries for sequences of microrings (or microdisks) resonators.

In this work, we studied various configurations of coupled disk/ring resonators. With these various structures, we observed the differences in the transmission spectrum between rings and disks resonators, we noticed the whispering gallery modes and the effect of the gap in the CRIT effect for a serially double-disks resonator.

On a first time, we studied the serially coupled configuration CROW where each ring resonator is coupled to one another. For this structure, we restrict our attention to two ring/disk based units. We observed the differences in the transmission spectrum between rings and disks resonators and we noticed the whispering gallery modes and the effect of the gap in the electromagnetically induced transparency effect for a serially double-disks resonator.

The second configuration that was studied is the SCISSOR configuration. In this case, all resonators are coupled to both the input and drop port waveguides. We characterized the behaviour of complex eight-resonators SCISSOR devices in the case of microdisks and microrings resonators. In order to facilitate the characterization of these complex structures, a new set-up was also build up, which allowed us to study the scattered light of the resonators from the top as a function of the wavelength. Finally, with this technique, for the first time, we demonstrated the presence of EIT-like band even in complex structures. Extremely small differences between adjacent rings can give rise to the appearance of EIT states, delocalized over only few rings and with a great Q-factor and strong out-of-plane scattering.

Reference

[1]. Jhon D. Joannopoulos, Robert D. Meade, Joshua N. Winn, *Molding the Flow of Light*, Princeton University Press (1999).

[2]. R. Soref and J. Lorenzo, *IEEE J. Quantum Electron.* **22**, 873 (1986).

[3]. R. Soref, J. Schmidtchen and K. Petermann, *IEEE J. Quantum Electron*. **27**, 1971 (1991).

[4]. *Silicon Photonics*, edited by L. Pavesi and D. Lockwood, *Topics in Applied Physics* **94** (Springer-Verlag, Berlin 2004).

[5]. M. Lipson, *J. Lightwave Technol.* **23**, 4222 (2005).

[6]. B. Jalali and S. Fathpour, *J. Lightwave Technol.* **24**, 4600 (2006).

[7]. R. Soref, *IEEE J. Selected Topics Quantum Electronics* **12**, 1678 (2006).

[8]. H. Rong, A. Liu, R. Jones, O. Cohen, D. Hak, R. Nicolaescu, A. Fang and M. Paniccia, *Nature* **433**, 292-294 (2005).

[9]. D. Navarro-Urrios et al., *Journal of Luminescence* **121,** 249–255 (2006).

Chapter two

Silicon Oxycarbide thin films: preparation, surface properties and photoluminescence measurements

In this chapter, we present a study of SiOC thin films obtained by sol-gel synthesis. Starting from a brief description of SiOC glasses and the sol-gel process to introduce our work, we explain how the thin films were prepared. Then we characterise the surface properties of the films with profilometer, AFM and SEM measurements. We study also the absorption coefficient of the films and compare it with results in literature of similar samples. Then we focus our work on the photoluminescence of the films, and a discussion on the origin of the strong emission is reported. We will also report a study of the effects of Boron addition on the photoluminescence of our thin films. Finally, to have an idea of the potential of our films, we will measure the external quantum efficiency of thus with a new technique create by us and compare them with Si-nc samples. This work was done within the *Polycernet* project.

2.1 Introduction[1]

Silicon oxycarbide is a term used to denote an alloy with a chemical structure in which silicon is simultaneously bonded with carbon and oxygen. These tetrahedral network species can be generally described as $[C_xSiO_{4-x}]$ where x=1, 2, or 3. The incorporation of carbon in silicate glasses presents the possibility of replacing some oxygen, which is only twofold, with carbon which can be fourfold. This increased bonding per anion is expected to strengthen the molecular structure of the glass network, and thereby, to improve its thermal and mechanical properties. These oxycarbide glasses have applications themselves, or they can be further processed to obtain dense glasses, porous glasses, powders, glass-ceramics or composites.

To synthesize silicon oxycarbide glasses, starting from a polymer pyrolysis at high temperatures is required in order to dehydrogenate and cross-link the terminal organic groups, and to achieve the

---

[1] This chapter results from a collaboration with the Material Engineering Department of the University of Trento where the samples were produced and most of the structural measurements performed. The sample production was due to Aylin Karakuscu and the chemistry modeling followed discussion with Professor Gian Domenico Sorarù.

original goal of coordinating the carbon atoms to two, three or four Si atoms. The resulting *silicon oxycarbide glasses* are shiny, black, X-ray amorphous materials. The black colour is most certainly due to the presence of an elemental form of carbon, but the unique characteristic of these silicon oxycarbide glasses is due to the presence of [$CSiO_3$], [C_2SiO_2], [C_3SiO] and [C_4Si] configurations in the glass network structure [1].

In general, the chemical characteristics of these glasses change continuously with the temperature used to process the precursor silicon oxycarbide polymer. These changes are associated with the thermal instability of the organic component and its chemical interaction with the inorganic component of the material and the processing atmosphere. These include redistribution and decomposition reactions as well as crystallization. This chapter will describe the sol-gel processing of silicon oxycarbides thin films and the characterization of their chemical and optical structure from the as-deposited state up to 1250°C. A model of the final (micro)structure is proposed.

2.2 Sol-gel method and synthesis of SiOC thin films

The sol-gel method is a low-temperature technique used for synthesizing solid glass bulks or thin films. It is based on the hydrolysis and polycondensation reactions of organometallic compounds, such as silicon alkoxides. These synthetic conditions allow for addition of dopants such as organic dyes, inorganic ions, and nanoparticles. The resulting materials are finding a very interesting use in optical and sensing applications. A large number of sophisticated materials has been prepared and studied using the sol-gel process, and significant experimental and theoretical insights have been gained. For example, recent publications report luminescent solar concentrators; photochromic, electrochromic, and gasochromic plates for smart windows; sensors for environmental and biological impurities; solid lasers tunable in the visible spectral range; active waveguides; materials for linear and nonlinear optics; semiconductor quantum dots; and complexes of rare earth ions that can be used as diagnostic and biological markers [2–7].

The sol-gel process has enabled the low-temperature synthesis of silicon oxycarbide glasses without the problems of decomposition and oxidation during the melting phase. This is achieved through the use of polymeric precursors containing SiC bonds. These precursors provide a direct Si-C bond in the starting solution which is preserved in the gel and glass structures; this is in contrast to the alkoxysilanes $Si(OR)_4$ which are commonly used for sol/gel synthesis of silica glass. In the case of these modified-alkoxysilanes, one or more of the alkoxy groups are replaced by saturated (e.g.,

CH_3, C_2H_5, C_3H_7) or unsaturated (e.g., C_2H_3, C_6H_5) radicals. The carbon chain-length, and the number and nature of the 'R' group modifications, allow a control of the amount of carbon introduced. An additional degree of compositional control is afforded by mixing the organically-modified alkoxysilanes, in desired molar ratios, with other alkoxysilanes. The gel, obtained after hydrolysis and condensation of the precursors, contains Si atoms bonded simultaneously to oxygen and carbon atoms. The silicon oxycarbide gels are commonly heat treated at intermediate temperatures (around 1000°C) to obtain silicon oxycarbide glasses.

The object of this work was to conduct the structural characterization of nearly stoichiometric silicon oxycarbide glasses, with compositions close to the tie-line between SiC and SiO_2, and to study their crystallization behaviour under Argon atmosphere between 800 and 1250 °C. To understand the effect of Si and C on the luminescence behaviour of the SiOC system, precursor compositions were chosen to give C-rich, stoichiometric and Si-rich SiOC films. According to previously published data [8], such glasses can be obtained from sol gel-derived polysiloxanes containing various amounts of Si-H and Si-CH_3 groups. The precursors used to create the gels are the triethoxysilane T_H and the methyldiethoxysilane D_H. The precursor ratios will be used to label the samples. In the present work, two gels, called T_HD_HX (X corresponds to the value of ratio T_H/D_H) have been created with molar ratios of 1:1 and 2:1. They have been pyrolyzed at 800 °C to give SiOC glasses, which were found to be, respectively (see Figure 2.1): (i) inside the SiO_2-SiC-C triangle, suggesting the presence of an excess of C (T_HD_H1), (ii) close to the stoichiometric SiC-SiO_2 line, indicating the formation of an almost pure silicon oxycarbide glass (T_HD_H2). On the other hand, Si-rich SiOC films were prepared from T^H without any addition of D^H.

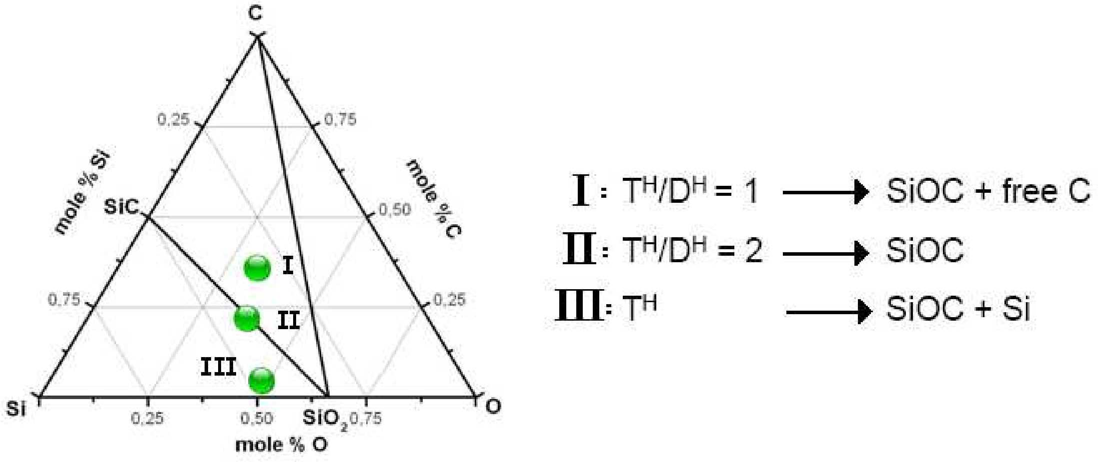

Figure 2.1. Si-C-O phase diagram showing the binary stable thermodynamic phases (SiO_2 and SiC), and the composition of the stoichiometric silicon oxycarbide glasses

For all compositions, ethanol was used as solvent with a ratio of EtOH/OEt=2. Proper amount of H_2O (pH =4.5, HCl) was added to the alkoxide solutions in order to induce hydrolysis and to have a gelling period long enough to allow sufficient time for film production. The selected solution was spun at 3000 rpm for 1 minute on ultrasonically cleaned SiO_2 (Heraeus-HSQ300) and Si (n-type) substrates. The gel films were stabilized at 80°C for 24 hours before pyrolysis. The pyrolysis process was carried out in a C-furnace under Ar flow (100 ml/min) with a heating rate of 5°C/min at different temperatures, in the range 800-1250 °C with 1 hour holding time at the maximum temperature.

2.3 Characterisation of the films

2.3.a Surface properties

Film thicknesses were determined by using a Hommel tester T8000 profilometer and Atomic Force Microscopy (AFM). Surface qualities and roughness of the films were investigated by Jeol JSM-5500 Scanning Electron Microscopy (SEM) and NT-MDT P47H Atomic Force Microscopy (AFM), with a scanning size of 50 μm. The transmission spectra of the SiOC films were recorded over the region 190–800 nm using a Carry 3 UV–vis spectrophotometer. Profilometer measurements and Scanning Electron Microscopy were done at the Engineering faculty by Aylin Karakuscu and AFM and spectrophotometer measurements in our laboratory.

We measured the thickness (d) and shrinkage as a function of the pyrolysis temperature. Results are shown in Figure 2.2. Film thicknesses were determined with a profilometer by measuring the depth of a scratch created with a razor blade on the film. We found that the thickness of the as deposited film was 910 nm and after pyrolysis at 1200 °C the thickness decreased to 490 nm. The errors shown in the graph are due to the precision of the profilometer equipment. For pyrolysis temperatures larger than 1100 °C, we can see that the thickness of the films is constant at 490 nm and the shrinkage reached a maximum value of 46 %. This shrinkage value is lower than the reported shrinkages of polycarbosilane-derived SiOC thin films in the literature [9].

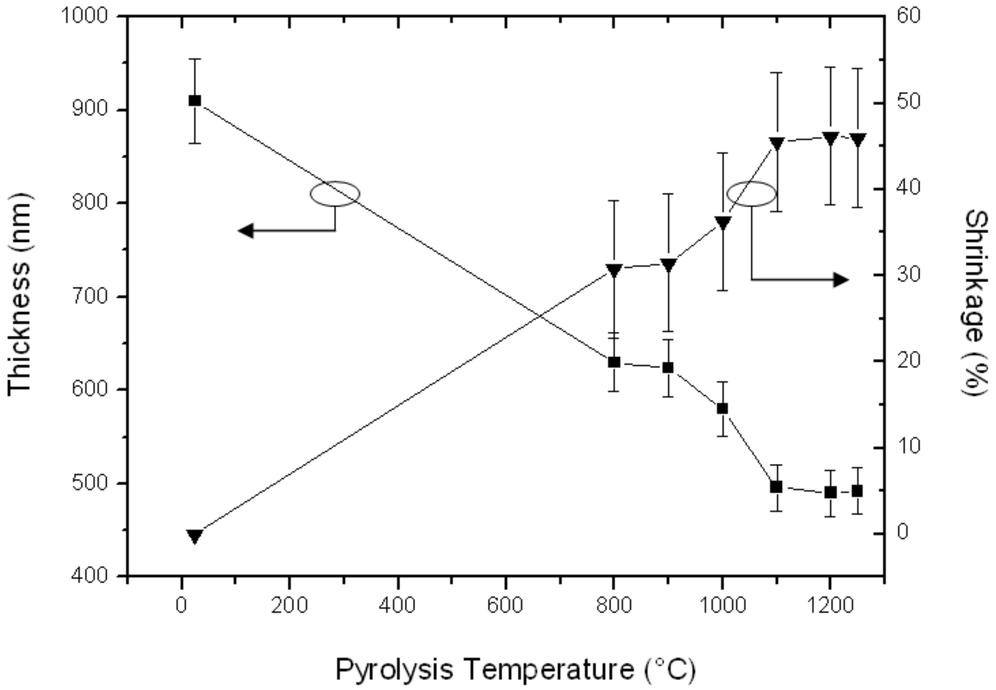

Figure 2.2. Thickness (squares) and measured shrinkage (triangles) of the films pyrolysed at different temperatures.

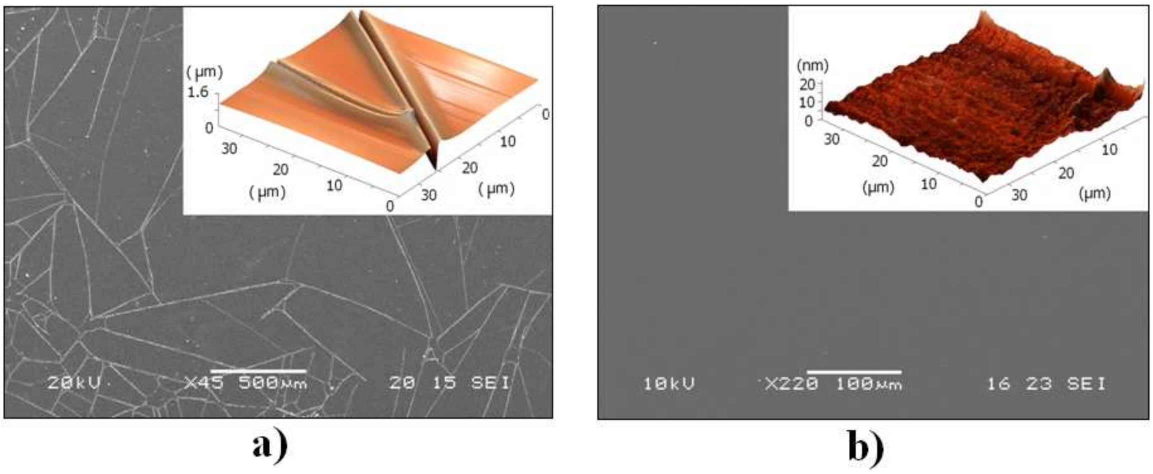

Figure 2.3. SEM images of samples annealed at 1200°C (a) before and (b) after optimisation. The inset shows AFM images of the two samples.

Surface properties of the films were examined by SEM and AFM. In order to produce homogeneous thin films, an optimisation procedure of the drying step was finalized. After an optimum drying step, SEM analysis showed that homogeneous and crack free films were produced at every pyrolysis temperature even at the edges of the specimen. The roughness of the films was measured by AFM and it was found an average roughness of 2.5 nm for all the pyrolysed samples. These results were obtained after using a drying step at 80 °C for 24 hours. In fact, Figure 2.3 shows the SEM and AFM images for films deposited without (Figure 2.3.a) and with (Figure 2.3.b) the drying step. It is observed that the large cracks present in the film in Figure 2.3.a are completely disappeared in Figure 2.3.b.

2.3.b Absorption coefficient measurements

Optical studies were performed on these films to determine the effect of pyrolysis treatments on the energy bandgap. The absorption coefficient α was determined from transmission measurements by neglecting light diffusion.

$$\alpha(\hbar\omega) = \frac{1}{d}\ln\left(\frac{1}{T}\right) \qquad (2.1)$$

where *d* is the film thickness and *T* the transmittance of the film.
The optical band gap E_g, for the annealed films was calculated by fitting the experimental data with the following equation:

$$(\alpha\ (\hbar\omega))^{1/n} = \text{constant}\ (\hbar\omega - E_g) \qquad (2.2)$$

where $\hbar\omega$ is the incident photon energy, α is the absorption coefficient, and the exponent n depends on the type of optical transitions involved: n=1/2, 2, 3/2 and 3 for allowed direct, allowed indirect, forbidden direct and forbidden indirect transitions, respectively [10,11].

In disordered states, the concept of band gap does not exist. But in case of the Silicium, as it yields a quasi-continuous distribution of states, we can speak about optical gap, which defines Eq. 2.2. In Fig. 2.4, we notice that the states that absorb bellow the optical gap (in our case bellow 4.3eV) are localised states du to the disordered matrix of our system. This will be these states that will give us the strong luminescence, and so that will be study afterwards.

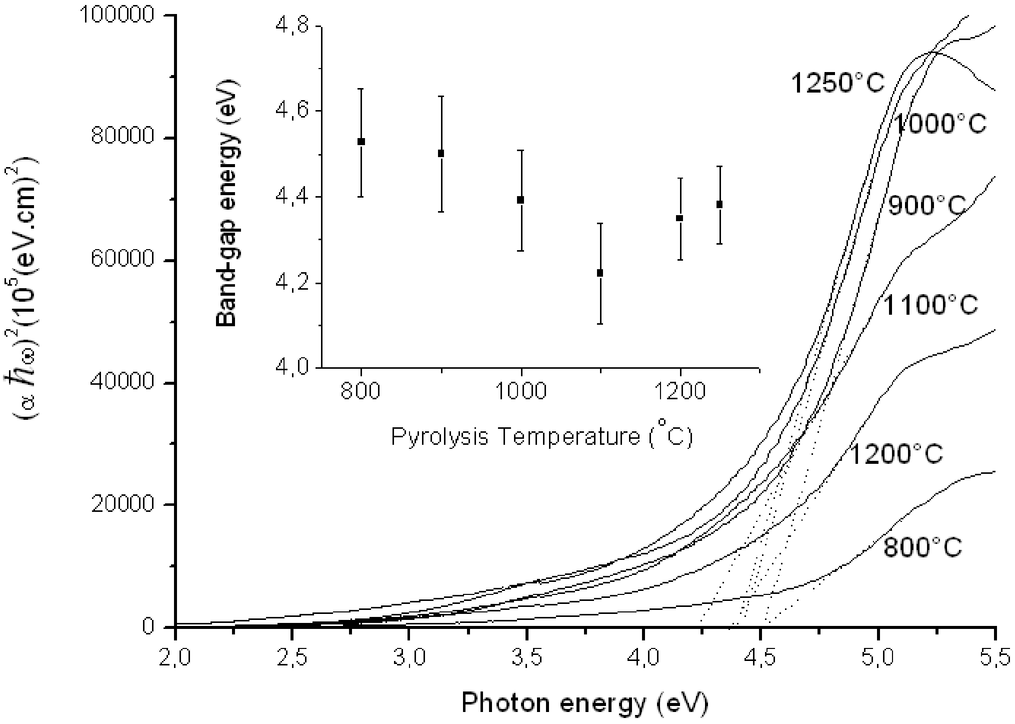

Figure 2.4. Plot of $(\alpha\hbar\omega)^2$ *versus photon energy of thin film annealed at the indicated temperatures. The dashed lines are fittings with equation (2.2). The inset shows the band-gap energies as a function of the pyrolysis temperature.*

Figure 2.4 shows the experimental absorption data with the corresponding fittings. In the high energy region of absorption edge, $(\alpha\ (\hbar\omega))^2$ versus $\hbar\omega$ plot was taken as an evidence for direct band gap. The intercept of the straight line on the $\hbar\omega$ axis gives the optical bands gaps which are shown in the inset at Fig. 3. We notice that the value of α at a fixed photon energy, let say 5.0 eV, increases from 800 °C to 1000 °C and then decreases. Only thin films annealed at 1250 °C do not follow this trend. We also noticed that the value of E_g slightly decreases from 800 °C to 1100 °C and then increases.

We postulate that the amorphous film is having a phase separation due to the annealing: the film gradually becomes a mixture of SiC–SiO_2. Note that this phase separation occurs in absence of external oxidation, i.e. the pyrolysis is not performed in an oxygen atmosphere. If we assume that the band gap of the composite is an average between that of SiC (2.3 eV) and of SiO_2 (8 eV), this will cause a decrease in band gap when more SiC is formed. Note that 1100°C, which separates the two observed trends (α strength and E_g) is also the temperature at which no more shrinkage in the film was observed (Figure 2.2). Let us note that a model calculation of amorphous silicon oxycarbide, with a composition similar to the one we are using, yields an energy band gap of 3.7 eV [12]. This value was found for an ordered amorphous network. When structural disorder or defects are introduced, the band gap raised to 5 eV. Considering the complexity of the system, we can argue that these model calculations are consistent with our experimental results.

2.4 Optical Characterisation

The continuous wave photoluminescence measurements were effectuated in the Luminescence Laboratory, where we can measure luminescence, reflectivity, absorption and excitation of the luminescence in the visible and near infrared range. It is equipped with various excitation sources, in our case we used an Ar Ion laser UV extended at a wavelength of 365nm. The light of the laser is sending on the sample with an angle of 45°. The photoluminescence is collected by a lens positioned in front of the sample and collected by a spectrometer. All the measurements were done at room temperature (300°K) and are controlled by computers.

2.4.a Photoluminescence of SiOC samples

Photoluminescence (PL) spectra of the films pyrolysed at different temperatures are given in Figures 2.5 and 2.6. The PL spectra showed two main bands: one at about 420 nm (2.9 eV named UV-blue peak) and one centred at 545 nm (2.3 eV named yellow peak). Note that the UV-blue peak occurs at the edge of the sensitivity range of our detection system and its lineshape cannot be resolved.

For a pyrolysis temperature of 800 °C, the films showed a strong UV-blue PL peak at 426 nm with a broad green-yellow tail. As the pyrolysis temperature was increased, the intensity of the peak at 426 nm decreases and the green-yellow tail evolves into a separate band centred at about 545 nm. The position of the UV peak does not change with the increase of the pyrolysis temperature; its intensity decreases and, eventually, this peak disappears at higher temperatures.

When we increase the pyrolysis temperature up to 1200 °C, as shown in Figure 2.6, the yellow band position does not change and its peak intensity increases. When the pyrolysis temperature rises to 1250 °C, the PL intensity decreases abruptly. A new flat broad band dominates the PL spectrum.

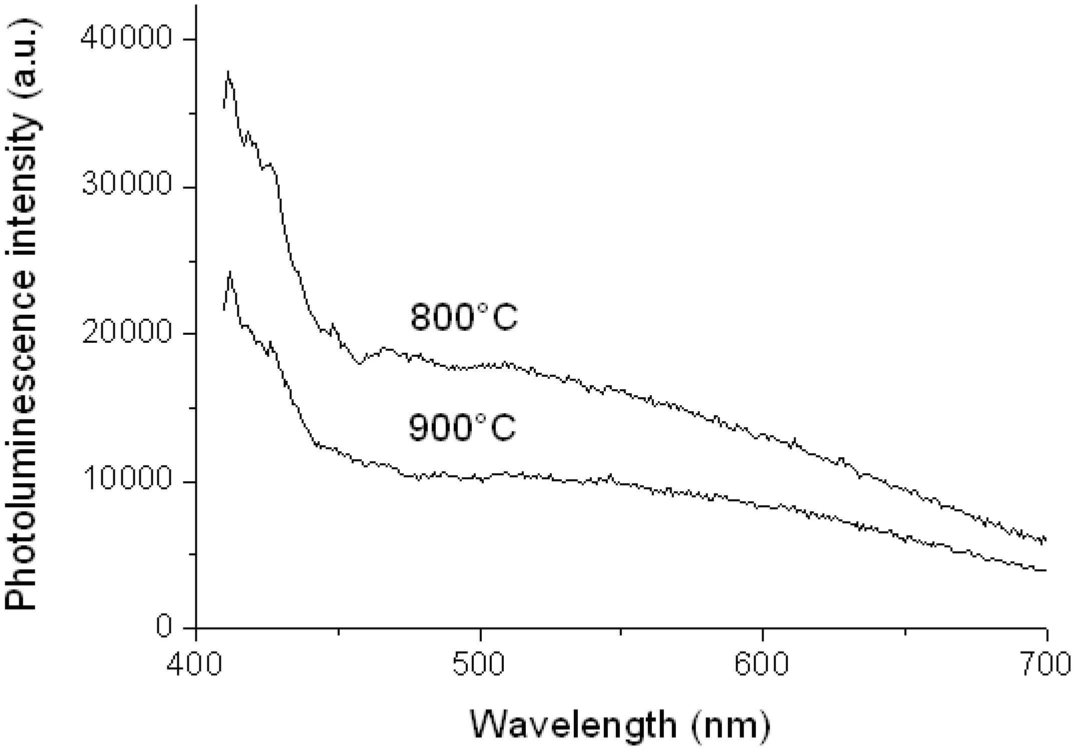

Figure 2.5. PL spectra of the films pyrolysed at 800 °C and 900 °C

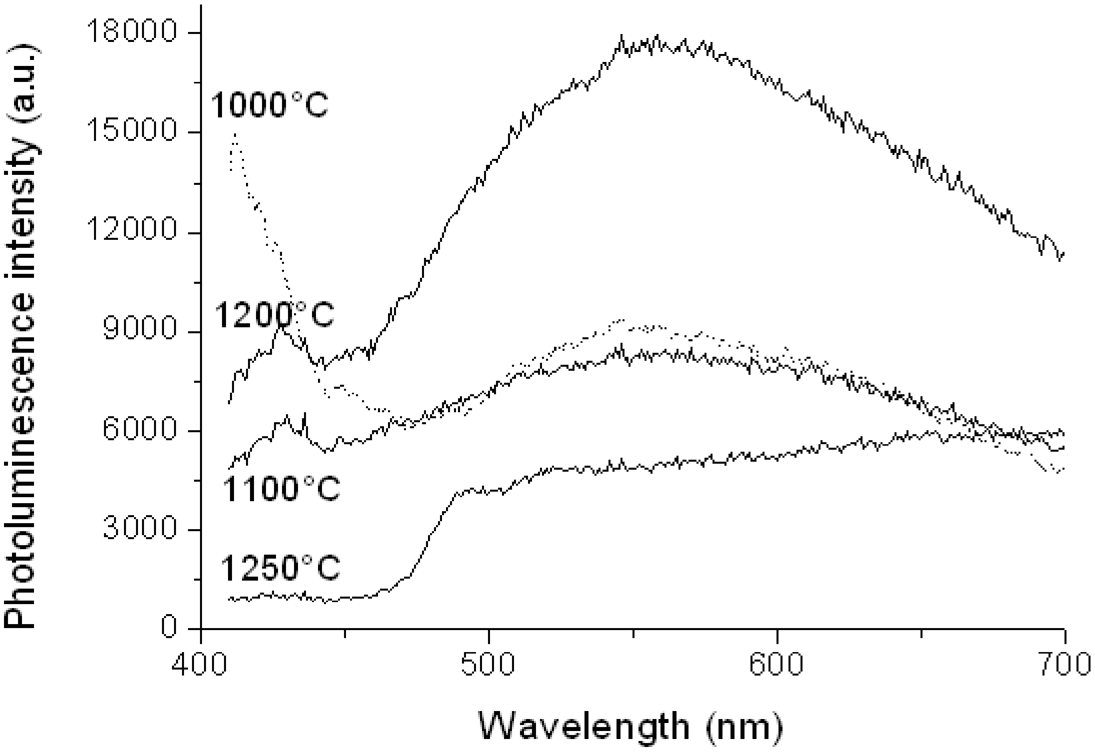

Figure 2.6. PL spectra of the films pyrolysed between 1000 °C and 1250 °C

To discuss the luminescence of the pyrolysed SiOC films we consider for simplicity that it is due to the interplay between an UV-blue band at about 420 nm (2.9 eV) and a yellow band centred at 545 nm (2.3 eV). As shown in Figure 2.5, the UV-blue weak band appears in thin films annealed at low temperatures, lower than 1100 °C. This band may relate to some intrinsic defects like carbon or silicon dangling bonds.

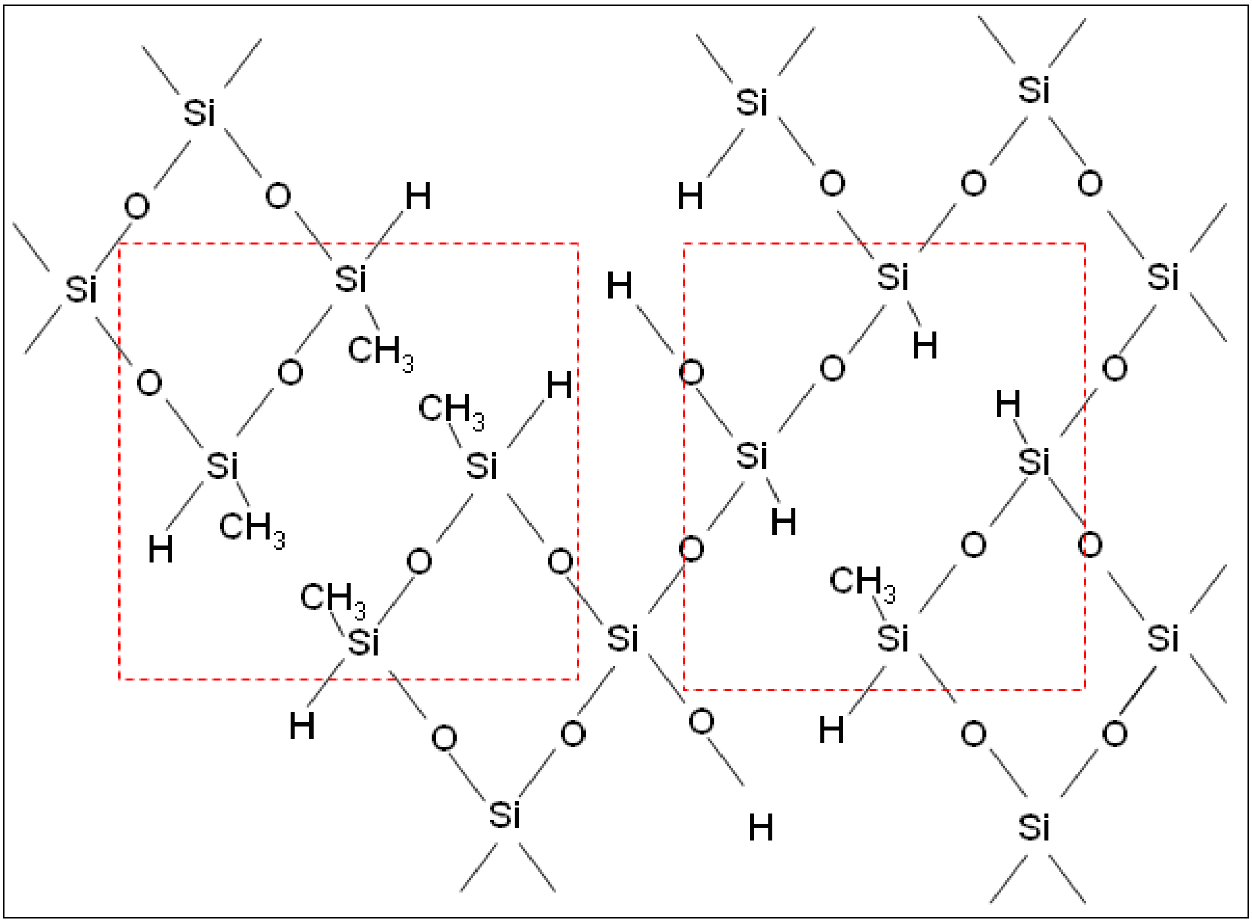

Figure 2.7. Chemical Structure of SiOC thin film as coated

A possible evolution of the chemical structure of the film during the pyrolysis process is shown in Figures 2.7, 2.8 and 2.9. The left side shows the starting local chemical bondings which eventually produces C clusters, while the right side shows the situation which yields SiC clusters. In the left side, the presence of CH_3 bonds favours the formation of CH_4, whereas in the right side, the Si-H bonding favours the H_2 release.

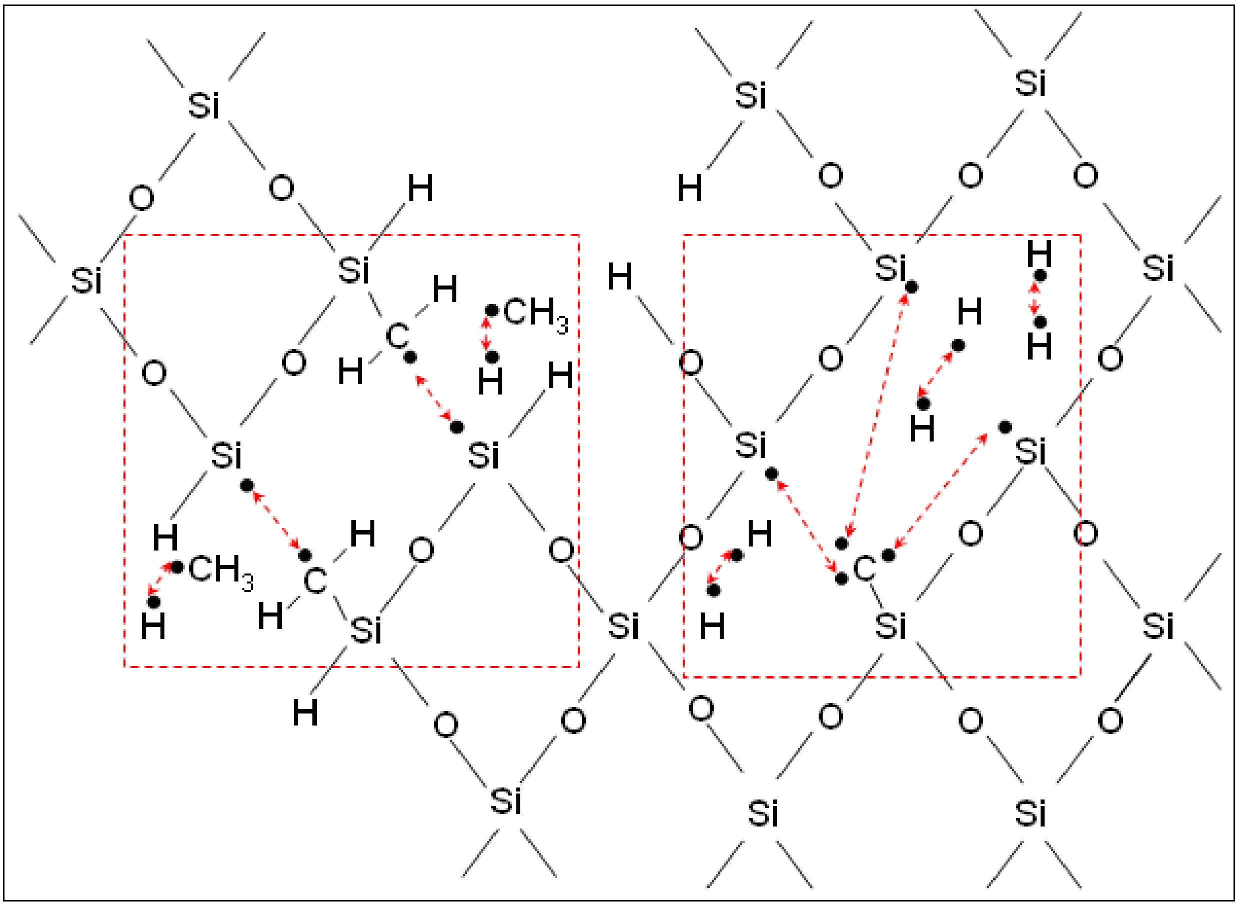

Figure 2.8. Chemical Structure of SiOC thin film at low annealing temperature.

An annealing at low temperatures (Figure 2.8) creates some free dangling bonds by removing hydrogen or CH_3 radicals. We propose that the origin for the UV-blue weak band may correlate with Si–O–C defects like Silicon or Carbon dangling bonds during the thermal treatment which are known to be present in SiOC system [13]. Similar PL emission originating from Si–O–C complex has previously been observed in C^+-implanted SiO_2 film [14] and amorphous SiOC film [15].

For temperatures higher than 1100 °C, the UV-blue band vanishes and the yellow band dominates the emission spectra. The dangling bonds left by Hydrogen diffusion (Fig. 2.8) recombines through the formation of stable Si-C or C-C bonds (Fig. 2.9). In fact, we have some evidence of formation of SiC nanoclusters embedded in SiO_2 films by transmission spectrum FTIR and XPS studies (see next chapter). It is known that the phase separation of SiCO into SiC and SiO_2 starts at temperatures close to 1200 °C [16].In our case the phase separation occurs at lower temperature due to the fact that we are working with thin films. We believe that the yellow band is partially due to emission from SiC nanoclusters with small diameters [17]. SiC nanoclusters emission occurs usually at 2.2 eV. In addition high pyrolysis temperature causes an increase in the size of the clusters and as a consequence their emission intensity decreases. This effect concurs to the decrease of the PL intensity in the film annealed at 1250 °C.

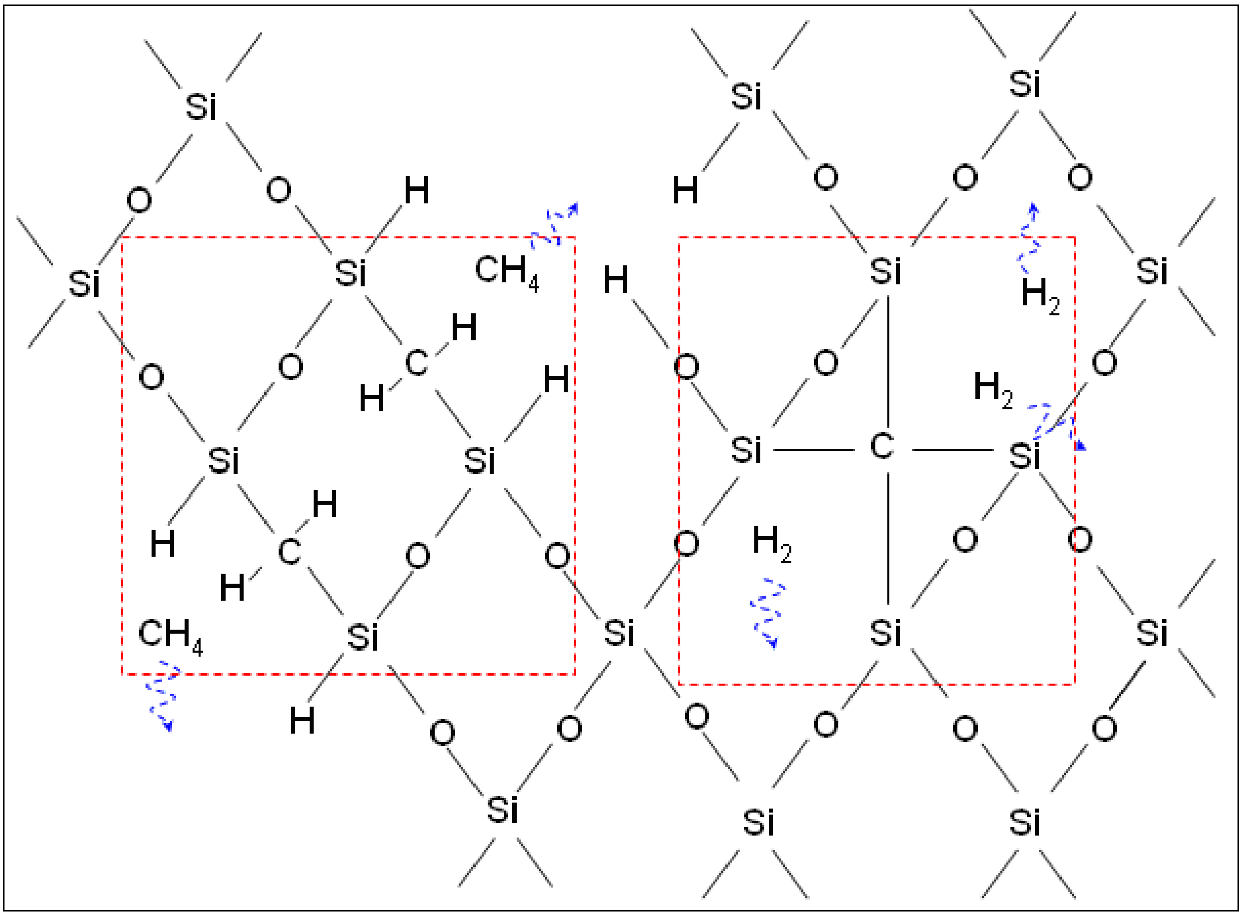

Figure 2.9. Chemical Structure of SiOC thin film at high annealing temperature.

In addition, very small amount of free carbon clusters may remain in the films after pyrolysis. As it is showed in Figure 2.9 on the left, some CH_4 residuals are still inside our samples at high annealing temperature. After pyrolysis, these residuals yield some carbon clusters by elimination of the hydrogen. These clusters can give resets luminescence in the yellow range (580 nm) and can influence the photoluminescence by broadening the emission band [18].

Finally, there is no presence of Si nanocrystals in our films after annealing process. As shown in Fig. 2.6, there is no band in the near infrared range, which is the characteristic band of Si nanocrystals. All experimental data confirmed the hypothesis that all the Silicon atoms bind either to O or C by formation of SiC bonds at high annealing temperature (Figure 2.9).

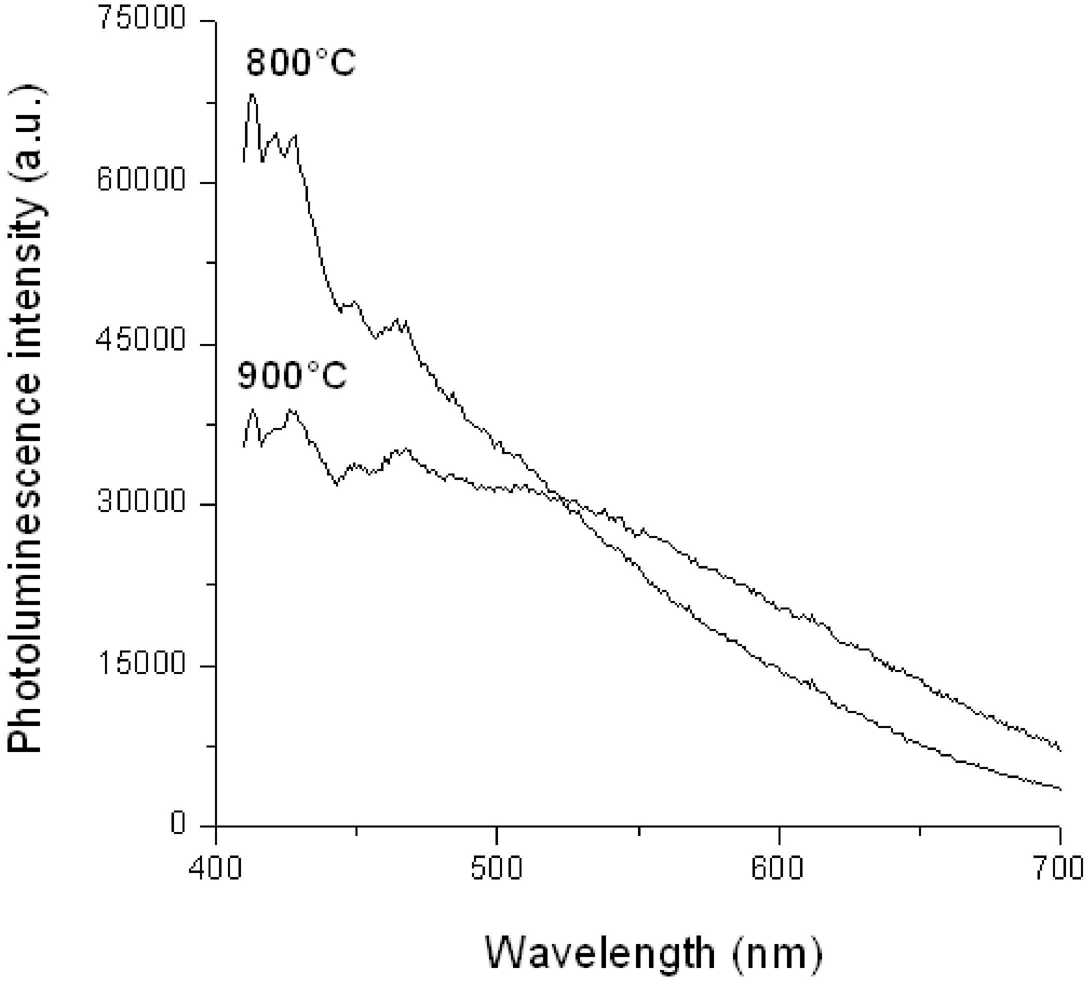

Figure 2.10. PL spectra of the T^H films pyrolysed at 800 °C and 900 °C

In order to complete our study on the evolution of the photoluminescence spectra in the low temperature range (800-1000 °C) for various thin films compositions , the PL spectra of the T^H films are given in Figure 2.10. A trend similar to the one observed for the T^HD^H2 films is reported. The disappearance at elevated temperatures of the UV-blue peak can be explained by the fact that in the amorphous state (800-1000 °C) SiOC ceramics are rich in defects, such as dangling bonds, whereas the high temperature annealing (1100-1200 °C) allows the reorganization of the structure and leads to a reduction of such defects [19].

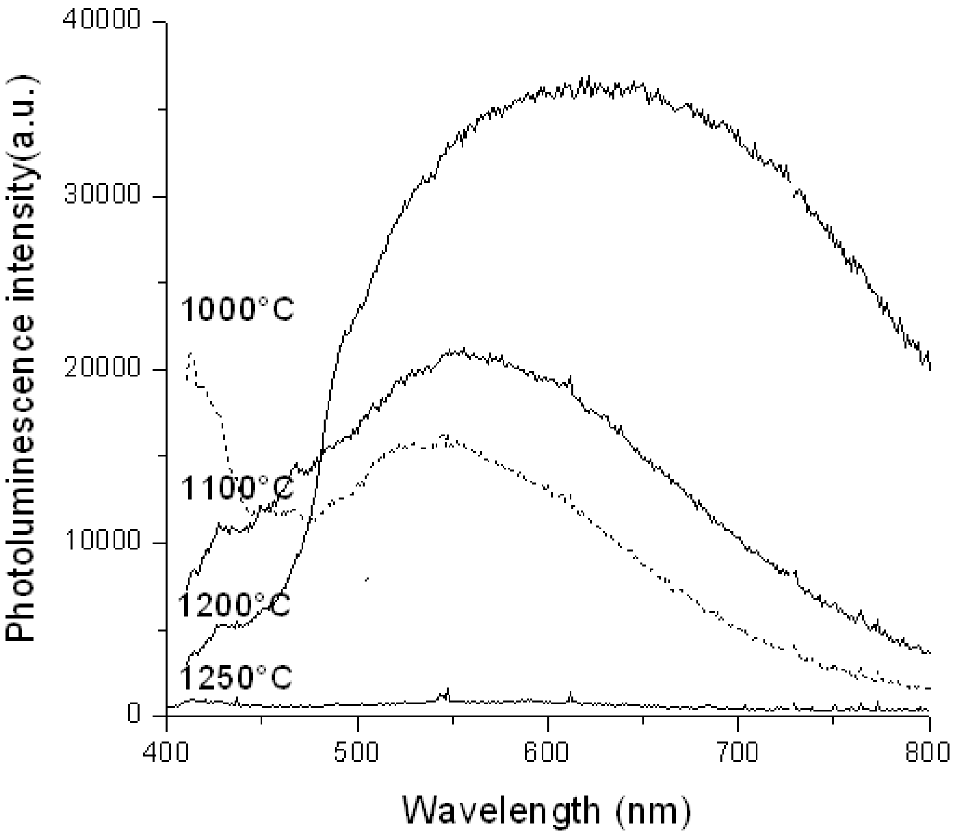

Figure 2.11. PL spectra of the T^H thin films pyrolysed between 1000 °C and 1250 °C

The PL spectra of T^H films, pyrolysed at high temperatures are given in Figure 2.11. Similar to T^HD^H2 films, T^H films showed a green-yellow band at 560 nm up to 1100 °C. The luminescence at 1100 °C can therefore be assigned to the same combination of SiC and C phases as in T^HD^H2. However, at 1200°C Si rich SiOC (T^H) films showed a sudden broadening with an increase in intensity. In previous study [20], a very wide luminescence peak centred at 600 nm was reported at 1050 °C in polymer derived silica based ceramics. Peak emission was explained by very small Si nanocrystals (Si-nc) formation or by silicon-oxide related defect sides but Si-nc formation was shown at higher pyrolysis temperature and caused narrowing PL peak and red shift [20]. Accordingly, in T^H films, the sudden widening at 1200 °C can be explained by phase separation of Si inside silicon oxycarbide network. Moreover, SiC and C phase presence in the system as well as the size distribution of the emitting sites could contribute to further widen the range of optical emission thus explaining the very unusual large width of the measured PL band which extends beyond the visible range (430 nm-900 nm).

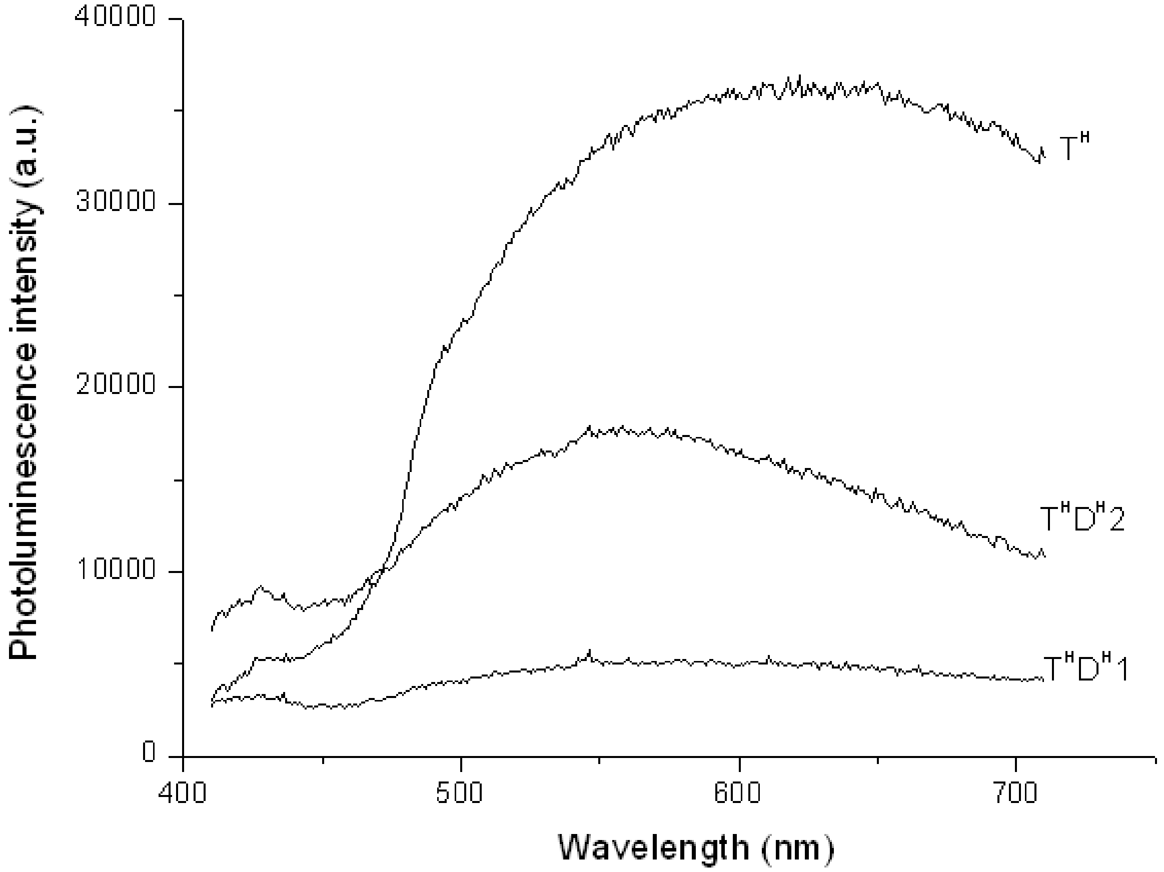

Figure 2.12. PL spectra of the T^H *,* T^HD^H2 *and* T^HD^H1 *films pyrolysed at 1200 °C*

Another study was also made on T^HD^H1 samples. T^HD^H1 is a well known system to produce C rich SiOCs [16]. The PL spectra of the various SiOC films at 1200 °C are shown in Figure 2.12. PL intensity of the T^H and T^HD^H2 films strongly increased with the temperature, reached a maximum at 1200°C and then drastically reduced at 1250°C. Conversely, the weak PL intensity of C-rich SiOC (T^HD^H1) films did not show any increase with the temperature. The low photoluminescence intensity of the T^HD^H1 sample is certainly related to the presence of a high excess of free carbon which absorbs the emitted light.

2.5 Effects of Boron addition on SiOC thin films

Our interest in the preparation and characterization of boron-containing SiOC glasses is due to the beneficial effect that this element has on the thermal stability of similar amorphous silicon carbonitride (SiNC) glasses [21]. Recently, it was reported the sol–gel synthesis of hybrid methyl-, ethyl-, and vinyl-modified SiO_2–B_2O_3 gels in which the B atoms are homogeneously dispersed in the siloxane network via ≡Si−O−B≡ bonds [22]. A great amount of Si−O−B bonds was observed in the samples that were prepared from ethyltriethoxysilane and vinyltriethoxysilane. Because of this homogeneous structure, these gels could be good precursors for the formation of homogeneous amorphous silicon-boron oxycarbide (SiBOC) glasses.

As for the previous samples, to obtain stoichiometric SiOC films, triethoxysilane (T^H) and methyldiethoxysilane (D^H) were used with T^H/D^H molar ratios of 2. Borosilicate gels with a nominal B/Si atomic ratio (0.1) were synthesized from triethylborate (TEB). The silicon alkoxides first were hydrolyzed with water that had been acidified by hydrochloric acid (HCl) (pH = 4.5) in order to induce hydrolysis and to have a gelling period long enough to allow sufficient time for film production. Then, the boron alkoxide was added in the proper amount without any further water addition and the gels were cast in test tubes that were left open for gelation. Details of the synthesis can be found elsewhere [22]. The selected solution was spun at 3000 rpm for 1 minute on ultrasonically cleaned SiO_2 substrate. The gel films were stabilized at 80°C for 24 hours before pyrolysis. Samples were labelled as TEB added SiOC.

2.5.a Surface properties

We measured the thickness and shrinkage as a function of the pyrolysis temperature. Results are shown in Figure 2.13. We found that the thickness of the as deposited film was 1210 nm and after pyrolysis at 1200 °C the thickness decreased to 610 nm. For pyrolysis temperatures larger than 1000 °C, we can see that the thickness of the films is constant at around 600 nm and the shrinkage reached a maximum value of 50 %. By comparison of the boron-containing SiOC glasses with that of pure Si-O-C suggested that the addition of boron to the Si-O-C glass slightly increased the high-temperature stability of the ternary oxycarbide glass (1000°C for SiOBC confront to 1100°C for SiOC).

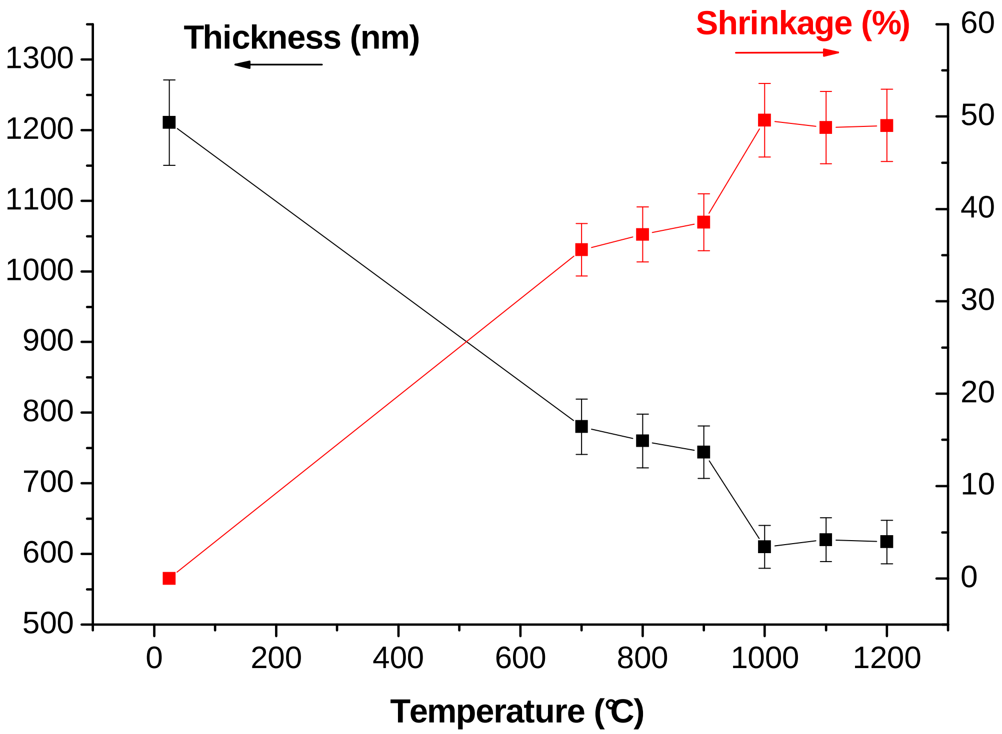

Figure 2.13. Thickness (black curve) and measured shrinkage (red curve) of the Boron added SiOC films pyrolysed at different temperatures.

Previous study shows that the pure Si-O-C glass is more stable toward SiC crystallization than the boron-containing samples [23]. The tendency toward SiC crystallization seems strongly dependent on the boron load, with an increase in SiC crystal size at 1500°C with the increasing B/Si ratio. By comparing the evolution of the B-free (SiOC) and B-containing samples (SiBOC), the important role of boron in promoting the nanostructural evolution has been discovered. In particular, B promotes the graphitization of nanocrystalline sp^2C leading to thicker graphite nanocrystals [24].

2.5.b Photoluminescence of Boron added SiOC

PL spectra of the films pyrolysed at different temperatures are given in Figure 2.14. Note that for PL at 1000°C and 1100°C, we multiplied the spectra by 10.

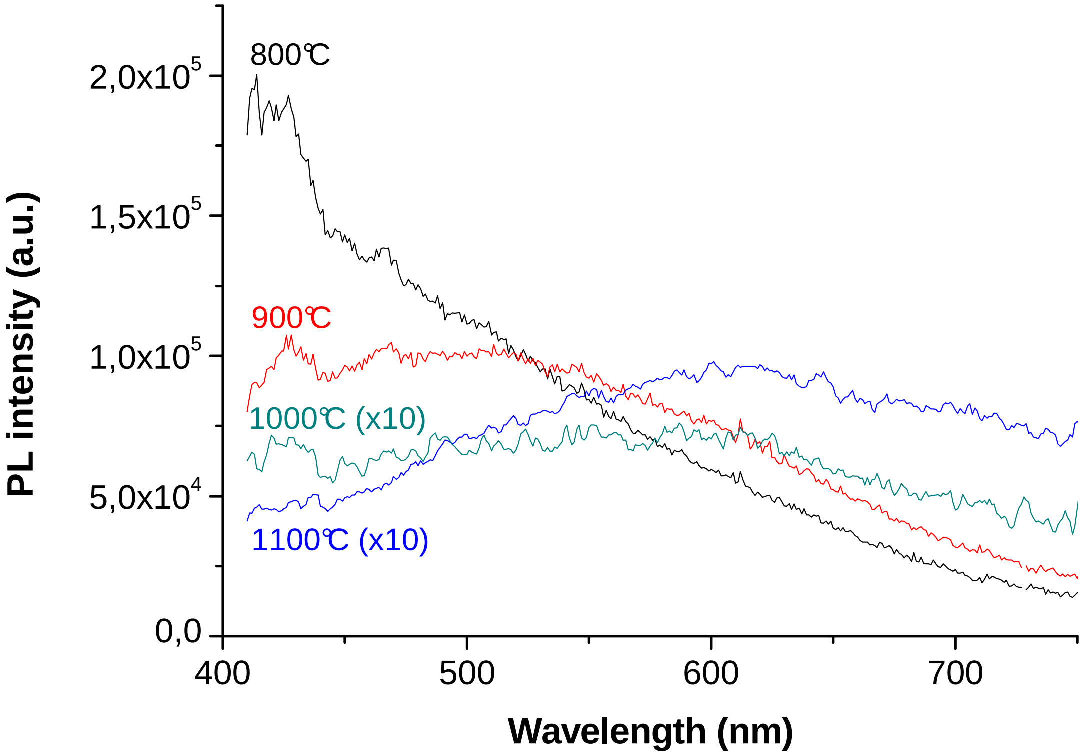

Figure 2.14. PL spectra of Boron added T^HD^H2 *films pyrolysed from 800 °C to 1100 °C*

For a pyrolysis temperature of 800 °C, the films showed a strong UV-blue PL peak at 426 nm with a broad green-yellow tail. As shown in Figure 2.14, the UV-blue weak band appears only in thin films annealed at low temperatures, lower than 1100 °C. This band may relate to some intrinsic defects like Si–O–C defects like Silicon or Carbon dangling bonds during the thermal treatment which are known to be present in SiOC system [13], as for T^HD^H2 films. We remember that similar PL emission originating from Si–O–C complex has previously been observed in C^+-implanted SiO_2 film [14] and amorphous SiOC film [15].

As the pyrolysis temperature was increased, the intensity of the peak at 426 nm decreases and the green-yellow tail evolves into a separate band centred at about 500 nm. The position of the UV peak does not change with the increase of the pyrolysis temperature; its intensity decreases and, eventually, this peak disappears at higher temperatures. For this UV-blue PL peak, we have the same evolution as for the SiOC films studied previously.

When we increase the pyrolysis temperature up to 1100 °C, as shown in Figure 2.14, the yellow band position changes and its peak intensity decreases. This behaviour is very different from the one that we had in SiOC thin films studied previously. When the pyrolysis temperature rises to 1200 °C, the PL intensity decreases abruptly and no luminescence was observed anymore.

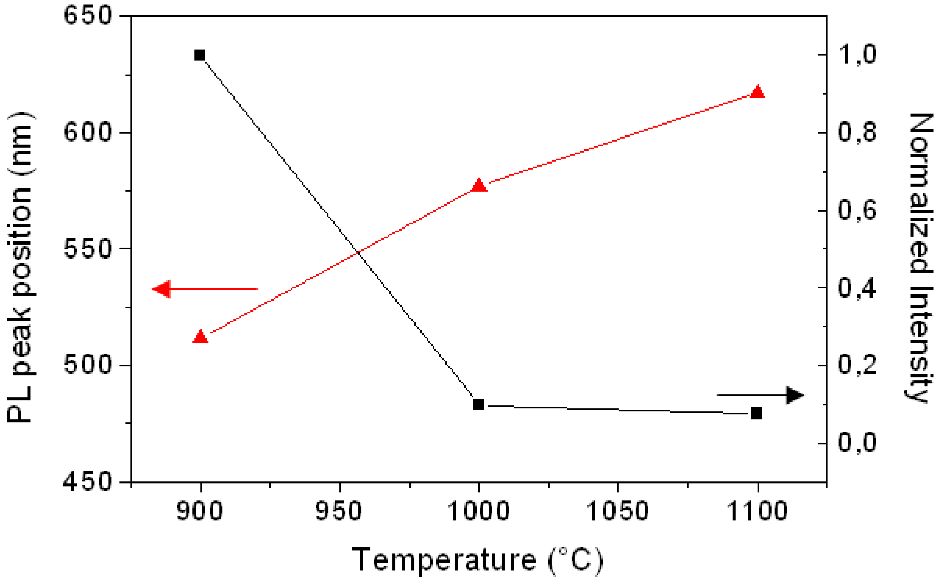

Figure 2.15. PL peak position (left) and normalized intensity (right) of Boron added T^HD^H2 *films in function of the annealing temperature.*

To understand better the evolution of the PL as a function of the temperature, we showed in figure 2.15 the PL peak position and its normalized intensity of for annealing temperatures in the range 900°C - 1100°C (Figure 2.15).

The fact that the normalized intensity decrease as we increase the annealing temperature can be explained by the fact that Boron promotes the graphitization of nanocrystalline sp^2C leading to large graphite nanocrystals. This high excess of free carbon absorbs all the emitted light, as for the T^H films studied previously.

We noted also that with boron addition, green-yellow luminescence occurs at temperature lower than the one for the SiOC films. This behaviour confirms the fact that the addition of boron to the Si-O-C glass slightly increases the high-temperature stability of the ternary oxycarbide glass, as previously reported in the literature [23].

Finally, the red-shift of the photoluminescence observed as we increase the temperature is attributed to the formation of C clusters. It is well know that carbon clusters can give luminescence in the yellow range (580 nm) in the form of a broad emission band [18]. As we observed before, Boron promotes the formation of carbon clusters. This red shift can be explained by the fact that as we increase the annealing temperature. Thus the most dominant PL emitting center shifts from SiC to Carbon clusters. As SiC nanoclusters emission occurs usually at 2.2 eV, i.e. 550nm, we observed a red-shift from 550nm to 580nm-600nm in the emission as the formation of carbon clusters becomes predominant in our system.

As we have very intense luminescent samples, the luminescence properties of conjugated polymers are of considerable interest, both because of the fundamental information that can be obtained about exciton formation and decay, and because of the potential applications for conjugated polymers as the emissive material in light-emitting diodes (LED) [25, 26]. To have an idea of the potential of our films, we will measure the external quantum efficiency of thus with a new technique create by us and compare them with Si-nc samples.

2.6 External Quantum Efficiency of SiOC samples

Measurements of the photoluminescence quantum yield of high refractive index samples are problematic owing to difficulties in determining the angular distribution of the emission, their reflectivity, and absorbance. Usually accurate measurements require calibrated integrating sphere and dedicated set-up. Here we propose a simple method. In the context of our SIOC thin films, there is great interest in establishing the absolute quantum efficiency for PL as this is considered to determine the limits to the efficiency of electroluminescent diodes. A quantitative measurement of external PL efficiency is useful for a number of other reasons. For instance, in conjunction with time-resolved PL measurements, it provides a means of determining the radiative and non radiative decay constants [27]. Competing non-radiative processes provide additional means of decay, and therefore reduce the efficiency of luminescence. Possible non-radiative mechanisms in the solid state include inter-chain processes (e.g. excimer formation), and quenching of excitons by extrinsic or conformational defects. If radiative and non-radiative decay are monomolecular processes with rates $\boldsymbol{\tau_r}$ and $\boldsymbol{\tau_{nr}}$, respectively, the overall luminescence decays will be exponential, with a lifetime, $\boldsymbol{\tau}$, given by

$$\tau^{-1} = \tau_r^{-1} + \tau_{nr}^{-1} \qquad (2.3)$$

The efficiency for radiative decay of excitons is then given by the internal quantum efficiency

$$\eta_{INT} = \frac{\tau}{\tau_r} \qquad (2.4)$$

The efficiency of radiative decay of excitons, η_{INT}, sets an upper limit on the quantum efficiency which can be obtained in our polymer based LED.

In a photoexcitation experiment, a useful figure is the photoluminescence (PL) efficiency, defined as the ratio of the emitted photons versus the absorbed photons. This figure of merit depends both on η_{INT} and on the fraction of photons which are able to escape from the material η_{EXT}. The PL efficiency, or external radiative quantum efficiency, η, is defined by Equation 2.5.

$$\eta = \eta_{EXT}\eta_{INT} = \frac{n_e}{n_a} \qquad (2.5)$$

Where n_e is the number of emitted photons and n_a is the number of absorbed photons.

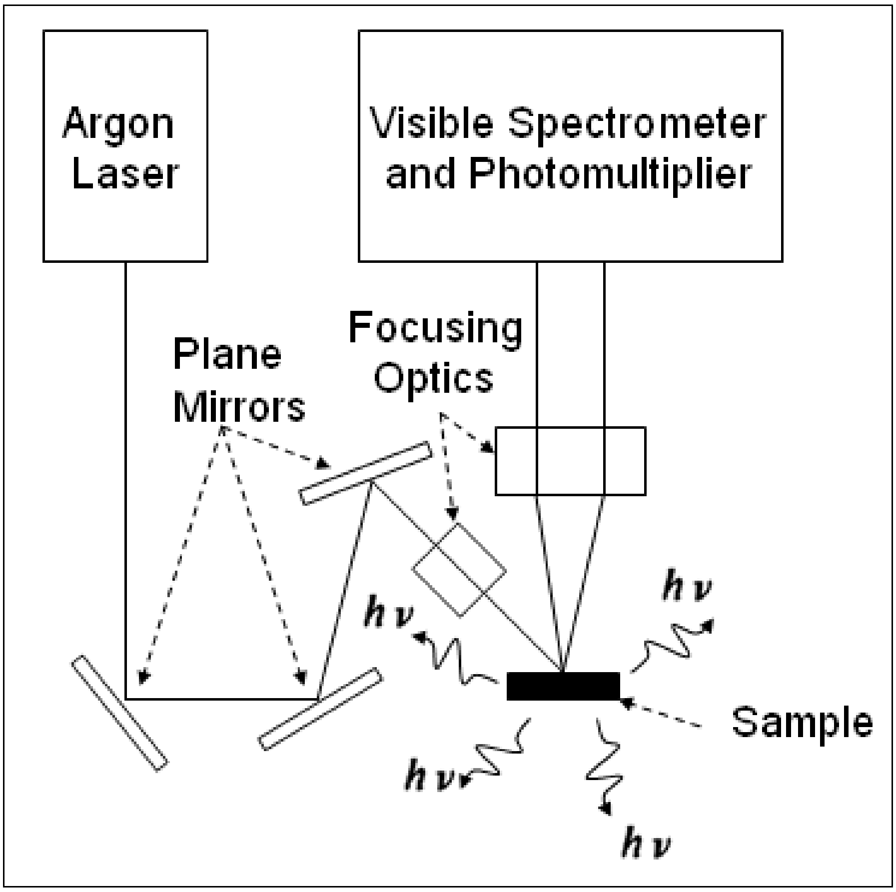

Figure 2.16. Schematic description of the experimental set-up for PL measurements

To measure the photon flux emitted from our samples, we calibrated the collection system described in Figure 2.16 (collecting lenses, monochromator, photomultiplier, photon counting unit) with a red LED whose responsivity is known. By using this calibration, we measured the spectrally integrated luminescence intensity emitted by our films under UV-photo-excitation and converted it into an emitted photon flux. The so-evaluated photon flux was corrected by the numerical aperture of the collecting system by assuming that the film is a lambertian point source. We considered that the total absorbed power by the active thin film is equal to the total laser power incident on the sample (P_{laser}) minus the power transmitted by the sample (P_{trans}), the power reflected by the sample (P_{refl}) and the power absorbed by the quartz substrate (P'_{refl}). We illustrated all these powers in Figure 2.17.

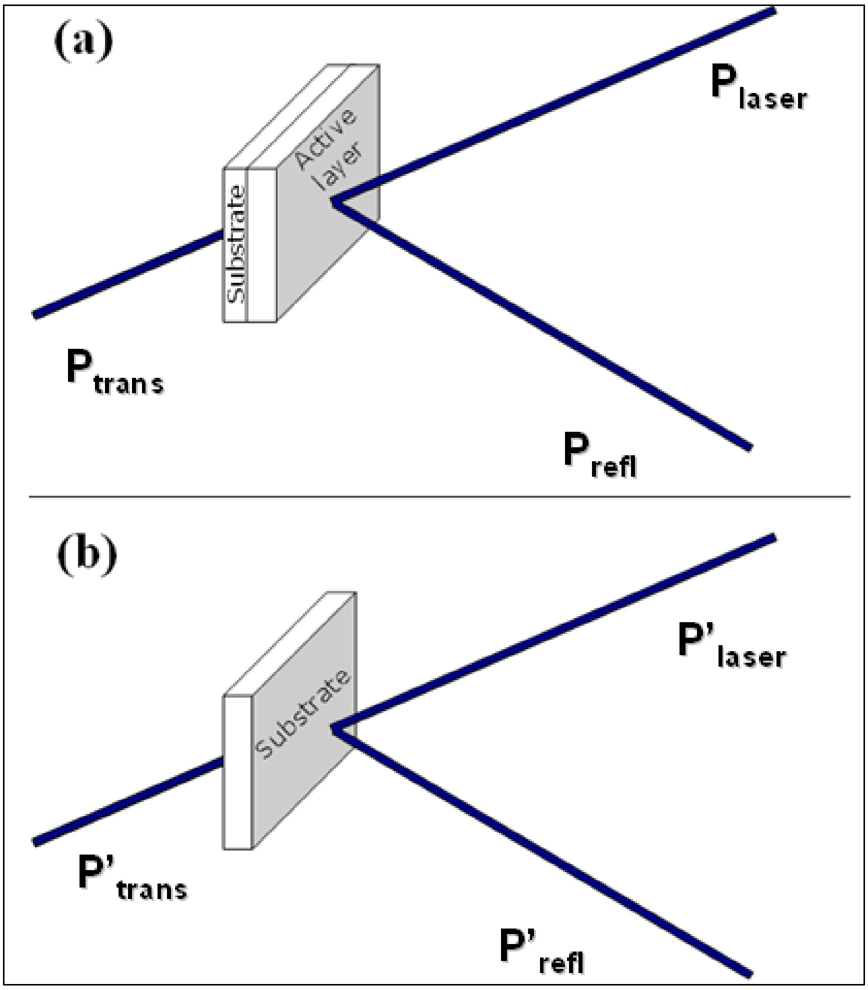

Figure 2.17. Schema of absorption, transmission and reflection powers in a case of a thin film (a) and of a substrate (b)

These quantities are measured with a power-meter calibrated at 365nm. Knowing the wavelength of the laser, we deduced the absorbed photon flux. The ratio between the emitted and the absorbed photon fluxes yields the external quantum efficiency of the film.

The first step of our measurements was the calibration of the spectrometer with a visible red LED. After measuring the power emitted at a known intensity, we measured the spectrum of the LED with the spectrometer (Figure 2.18). Knowing the emitted power, correcting by the collection angle, we calibrated the photomultiplier counts in units of power.

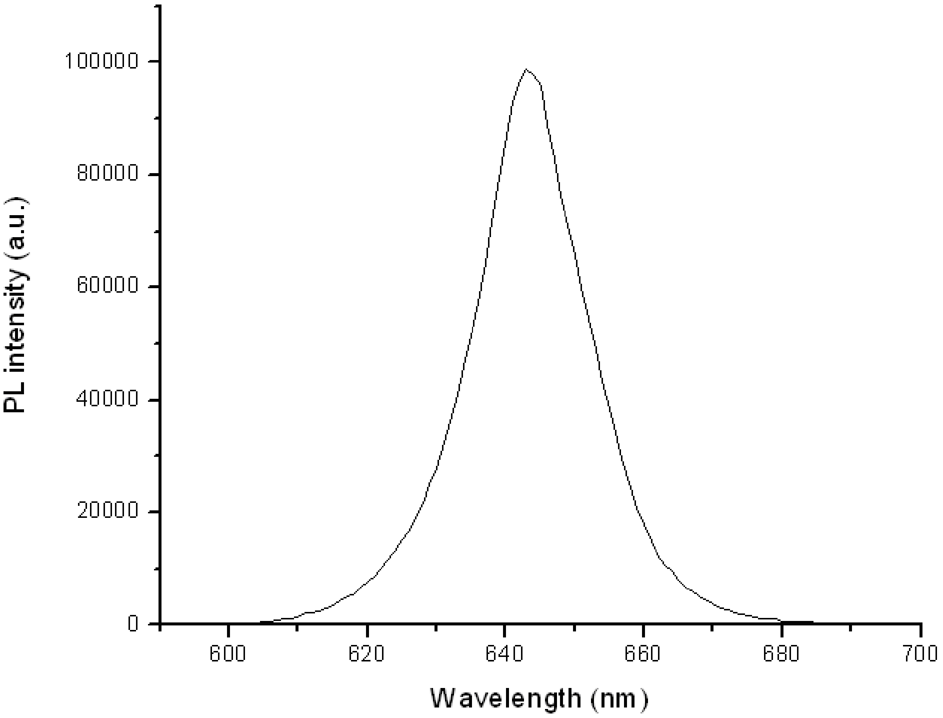

Figure 2.18. Luminescence Spectrum of red LED

The first measurement of External Quantum Efficiency that we made was on colloidal suspension of Silicon Nanocrystals. The external quantum efficiency of these samples is well described in the literature [28, 29]. In our case, these samples will be use as a reference to test the accuracy of the method. Figure 2.19 shows various emission spectra of colloidal suspension of Silicon Nanocrystals with different dilutions ratios of nanocrystals.

The fraction of the emitted light collected by the spectrometer is estimated by assuming an isotropic emission of the Si-nc. Geometrical arguments give that only 0,88% of the light emitted by our sample is collected.

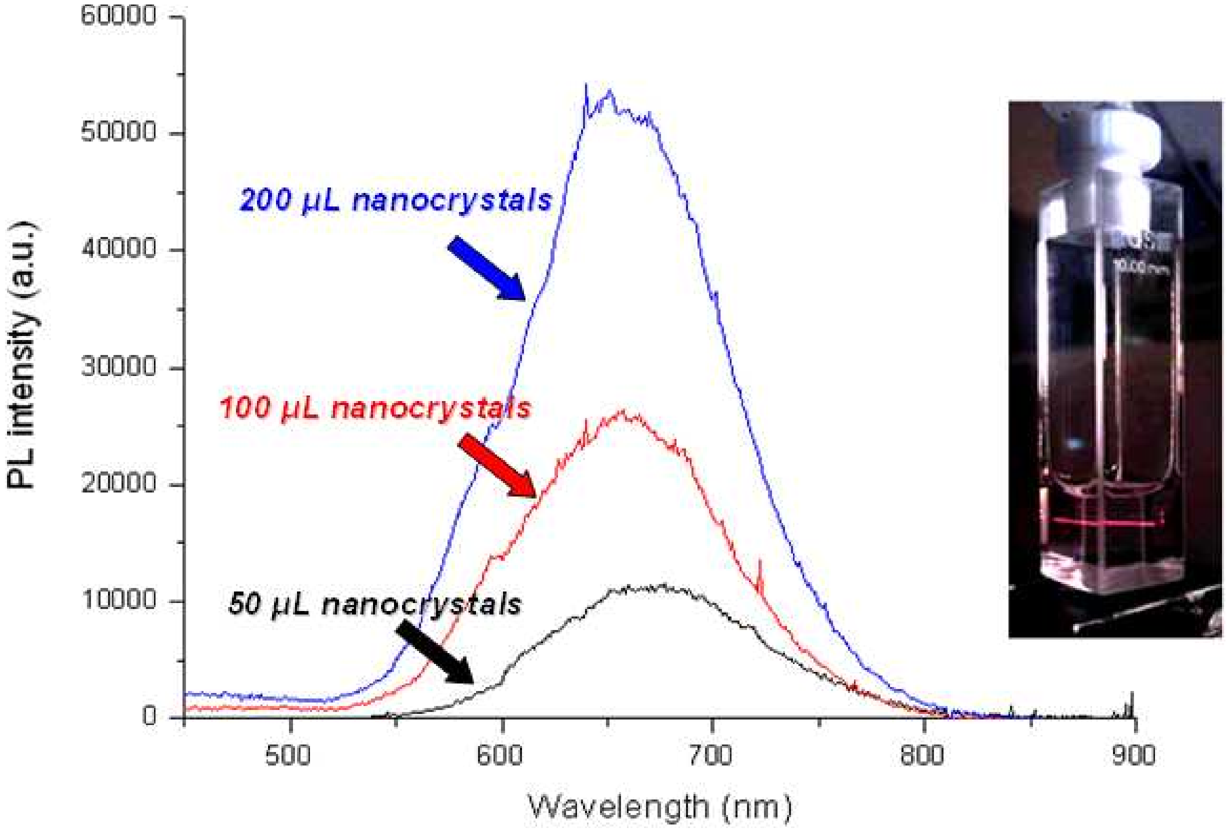

Figure 2.19. PL spectra of colloidal suspension of Si-nc in ethanol for different dilutions ratios. (inset) Photography of the sample under UV laser beam.

We made multiples measurements with various concentrations of nanocrystals, to have a better value of our external quantum efficiency. Table 1 summarized the results.

Quantity of nanocrystals starting solution (µL) in 1mL ethanol solution	P_{abs} (µW)	$P_{emitted}$ (µW)	E.Q.E.
50 µL	14,7 ± 0,1	0,7 ± 0,1	4,6 ± 1%
100 µL	31,8 ± 0,1	1,4 ± 0,1	4.3 ± 1%
200 µL	53,9 ± 0,1	2,8 ± 0,1	5,2 ± 1%
AVERAGE	33,5 ± 0,1	1,6 ± 0,1	4,7 ± 1%

Table 1. External Quantum Efficiency of colloidal suspension of Si-nc for various concentrations

In order to have a more accurate estimation of the external quantum efficiency of our nanocrystals, we measure the depth of focus *D.F.* of our collection lens, which is the range of focus of our collection lens, using Eq. 2.6, in order to measure the volume of the sample from which we collect the luminescence with the collecting lens (Fig. 2.20).

$$D.F. = 2N.\frac{f}{1000} \tag{2.6}$$

where N is the f-number of our lens and f is the lens focal length.

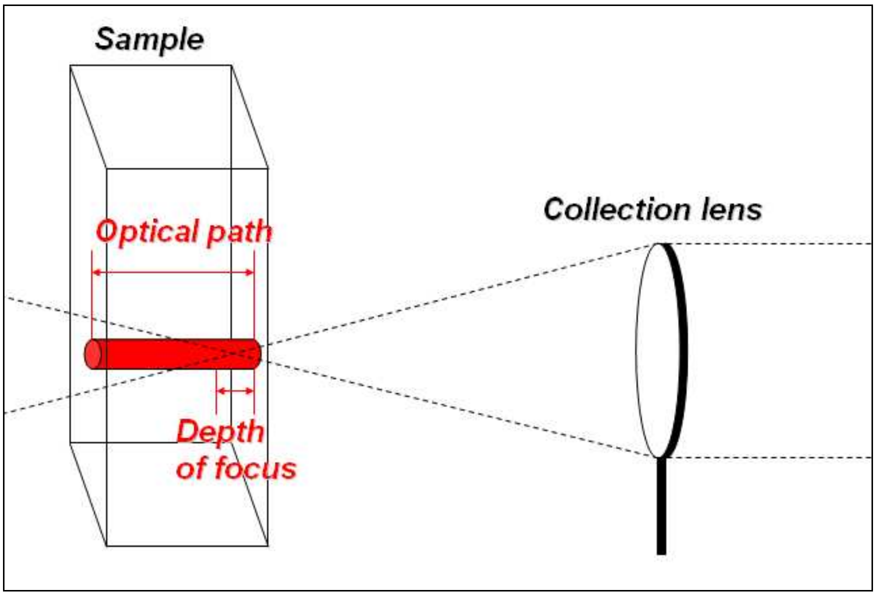

Figure 2.20. Schema of the Optical path and the Depth of focus in case of a tube sample

In our case, we found $D.F.$ = 2.6 mm. As the optical path of our quartz cuvette is 1 cm, the external quantum efficiency η is

$$\eta = \frac{P_{emitted}}{P_{abs}\frac{V_{emitted}}{V}} \tag{2.7}$$

where $V_{emitted}$ is the volume of the sample from which we collect light and V is the total volume excited by the laser. In our case, $V_{emitted}/V$ =3.8. Table 1 now reads

Quantity of nanocrystals starting solution (μL) in 1mL ethanol solution	E.Q.E.
50 μL	17,5 ± 4%
100 μL	16,3 ± 4%
200 μL	19,8 ± 4%
AVERAGE	17,9 ± 4%

Table 2. External Quantum Efficiency of colloidal suspension of Si-nc for various concentrations corrected by the depth of focus of our collection lens

To conclude, we can argue that the external quantum efficiency of our colloidal suspension of Si-nc is between 10% and 20%. This result is very close to various results found in the literature, which oscillate between 1% and 20% [28, 29].

We repeated the measurements on the SiOC samples. We found a value of 5.0 ± 1% for the T^HD^H2 film annealed at 1200°C. This value is encouraging as it compares to the best results reported in the literature about Si nanomaterials so far [30, 31].

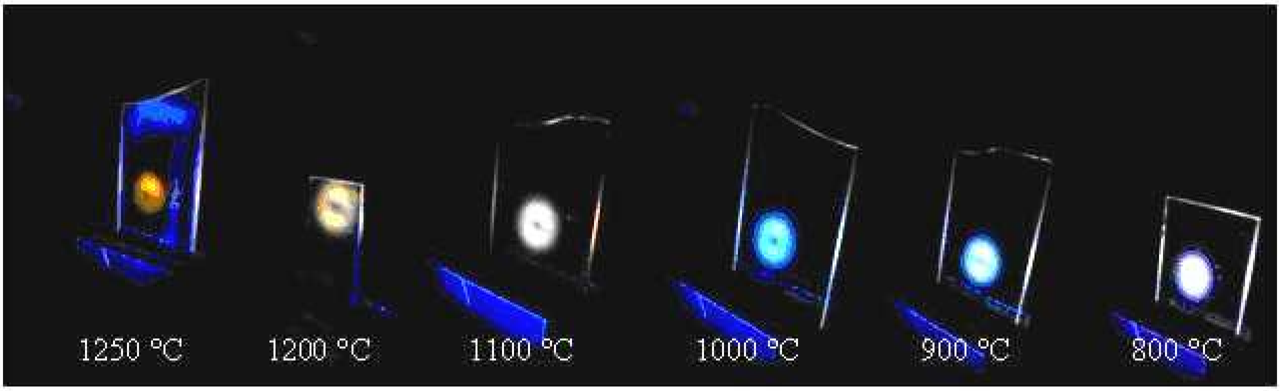

Figure 2.21. Photographs of the T^H films pyrolysed from 800 °C to 1250 °C under UV laser excitation.

Photographs of the T^H films pyrolyzed at different temperatures from 800 to 1250°C under blue light excitation are shown in Figure 2.21. The strong emission from the edges of the samples is caused by waveguide effects of the quartz substrate. The colours of the visible photoluminescence range from UV-violet for 800 °C to blue at 1000 °C and yellow-orange for 1250 °C. At 1250 °C the substrate starts to show an opaque appearance which could be indicative of thermal stability-related problems and can be the reason of the sudden PL intensity decrease at this temperature.

Table 3 shows the summary of the E.Q.E. results for the various samples at different annealing temperatures.

Sample	Annealing Temperature (°C)	E.Q.E.
T^H	1200	11.5 ± 1 %
T^H	1100	5.8 ± 1 %
T^HD^H2	1200	5.0 ± 1 %
Boron added T^HD^H2	900	2.5 ± 1 %

Table 3. External Quantum Efficiency of SiOC samples annealed at different temperatures

The external quantum efficiency of the T^H films pyrolysed at 1200 °C was 11.5 %; whereas, T^HD^H2 films showed 5% efficiency. Since T^HD^H1 films did not show noticeable luminescence, they had relatively low quantum efficiency. These external quantum efficiency values are very promising and make SiOC a potential material for LED applications.

2.7 Conclusion

SiOC films were produced via polymer pyrolysis of sol-gel derived films. We used various techniques to characterize chemically and optically the samples. Most importantly we followed the evolution of the films as a function of the pyrolysis temperature. The films had different luminescence properties between low temperatures (800 °C-900 °C) and high temperatures (1000 °C-1250 °C). At low temperature, the films are in an amorphous state (800 °C-900 °C) and emit a narrow band in the blue, which is attributed to Carbon and Silicon dangling bonds. The increase of the pyrolysis temperature ($\geq$ 1000 °C) allows the phase separation of SiOC and the formation of SiC and C clusters into SiO_2 matrix. The composite nature of the film yields a rich emission spectrum with recombination due to both phases and to their interfaces. Most notably SiC nanoclusters and C clusters contribute to the yellow luminescence in these films. The interpretation of the photoluminescence is also supported by FTIR and XPS measurements published in [32].

Finally, we studied the effect of Boron incorporation in our thin films. By comparing the evolution of the B-free (SiOC) and B-containing samples (SiBOC), the important role of boron in promoting the nanostructural evolution has been discovered. In particular, B promotes the following:

(i) The graphitization of nanocrystalline sp^2C leading to thicker graphite nanocrystals.

(ii) A stable high-temperature ternary oxycarbide glass .

(iii) A red-shift of the PL due to the fact that Boron promotes the formation of Carbon clusters emitting at 580nm.

A new technique of External Quantum Efficiency was explained in details. The external quantum efficiency of the T^H films pyrolysed at 1200 °C was 11.5 %; whereas, T^HD^H2 films showed 5% efficiency. Since T^HD^H1 films did not show noticeable luminescence, they had relatively low quantum efficiency. These external quantum efficiency values are very promising and make SiOC a potential material for LED applications.

Reference

[1]. C.G. Pantano, A.K. Singh and H.J. Zhang. *J. Sol–Gel Sci. Technol.* **14,** 7 (1999).

[2]. R. Reisfeld, *Sol-Gel Technology (Handbook)* **12,** 239 (2004).

[3]. R. Reisfeld, *Polymery* **51,** 95 (2005).

[4]. R. Reisfeld and Ts. Saraidarov, *Opt. Mater*. **28,** 64-70 (2006).

[5]. R. Reisfeld, M. Zelner, T. Saraidarov, and H. Minti, *Advances in Energy Transfer Processes* (2001), p. 341.

[6]. R. Reisfeld, D. Shamrakov, and C. K. Jorgensen, *Sol. Energy Mater. Sol. Cells* **33** (1994), p. 417.

[7]. R. Reisfeld, *Optical and Electronic Phenomena in Sol-Gel Glasses and Modern Applications, Structure and Bonding* **85,** 99 (1996).

[8]. G.D. Soraru, G. D'Andrea, R. Campostrini, F. Babonneau, *J. Mater. Chem.* **5,** 1363 (1995).

[9]. P. Colombo, T.E. Paulson, C.G. Pantano, *J. Sol.-Gel. Sci. Tech*. **2,** 601 (1994).

[10]. Pankove, J.I., Optical *Processes in Semiconductors, Princeton Press*, N.J. (1971).

[11]. Mott, N.F.and Davis, E.A., *Electronic Processes in Non-Crystalline Materials, Clarendon Press*, London (1971).

[12]. P. Kroll, *J. Mater. Chem*. **13,** 1657 (2003).

[13]. G. D. Soraru, F. Babonneau, and J**.** D. Mackenzie, *J. Mater. Sci.* **25,** 3886 (1990).

[14]. J. Zhao, D. S. Mao, Z. X. Lin, B. Y. Jiang, Y. H. Yu, X. H. Liu, H. Z. Wang and G. Q. Yang, *Appl. Phys.Lett*. **73,** 1838 (1998).

[15]. Fu Z P, Li M, Yang B F and Liu R C, *Thin Solid Films* **339**, 12 (2001).

[16]. H. Brequel, J. Parmentier, S. Walter, R. Badheka, G. Trimmel, S. Masse, J. Latournerie, P. Dempsey, C. Turquat, A. Desmartin-Chomel, L. Le Neindre-Prum, U. A. Jayasooriya, D. Hourlier, H.- J. Kleebe, G. D. Soraru, S. Enzo, F. Babonneau, *Chem. Mater*. **16**, 2585 (2004).

[17]. M.B. Yu, Rusli, S.F. Yoon, Z.M. Chen, J. Ahn, Q. Zhang, *J Appl Phys*. **87,** 8155 (2000).

[18]. J. C. Pivin and M. Sendova-Vassileva, *Solid State Commun*. **106,** 133 (1998).

[19]. G.D. Sorarù, F. Babonneau and J.D. Mackenzie, *J. Mat. Science* **25**, 3886 (1990).

[20]. G. D. Soraru, S. Modena, P. Bettotti, G. Das, G. Mariotto, L. Pavesi, *Appl. Phys. Lett.* **83,** 749 (2003).

[21]. R. Riedel, A. Kienzle, W. Dressler, L. Ruwisch, J. Bill, and F. Aldinger, *Nature (London)* **382,** 796 (1996).

[22]. G. D. Sorarù, N. Dallabona, C. Gervais, and F. Babonneau, *Chem. Mater.* **11,** 910 (1999).

[23]. Schiavon M. A., Gervais C., Babonneau F., Soraru G. D., *J. Am. Ceram. Soc*. ***87,*** 203 (2004).

[24]. R. Penà-Alonso et al., *Chem. Mater.* **19,** 5694 (2007).

[25]. J.H. Burroughes, D.D.C. Bradley, A.R. Brown, R.N. Marks, K. Mackay, R.H. Friend, P.L. Bum and A.B. Holmes, *Nature* **347**, 539 (1990).

[26]. H. Sirringhaus, N. Tessler & R. H. Friend, *Science* **280,** 1741–1744 (1998).

[27]. I. D. W. Samuel, B. Crystall, G. Rumbles, P. L. Burn, A. B. Holmes, R. H. Friend, *Synth. Met.* **54**, 281 (1993).

[28]. G. M. Credo, M. D. Mason, S. K. Burattoa, *Appl. Phys. Lett.* **74**, 1978-1980 (1999).

[29]. Valenta et al., *Advanced Functional Materials* **18**, 2666–2672 (2008).

[30]. C. Turquat, H.J. Kleebe, G. Gregori, S. Walter, G.D. Soraràù, *J. Amer. Ceram. Soc.* **84,** 2189 (2001).

[31]. J. C. Pivin and M. Sendova-Vassileva, *Solid State Commun.* **106,** 133 (1998).

[32]. A. Karakuscu, R. Guider, L. Pavesi, G.D. Soraràù, *J. Am. Ceram. Soc.* **92**, 2969-2974 (2009).

Chapter three

Silicon on Insulator waveguides and building blocks

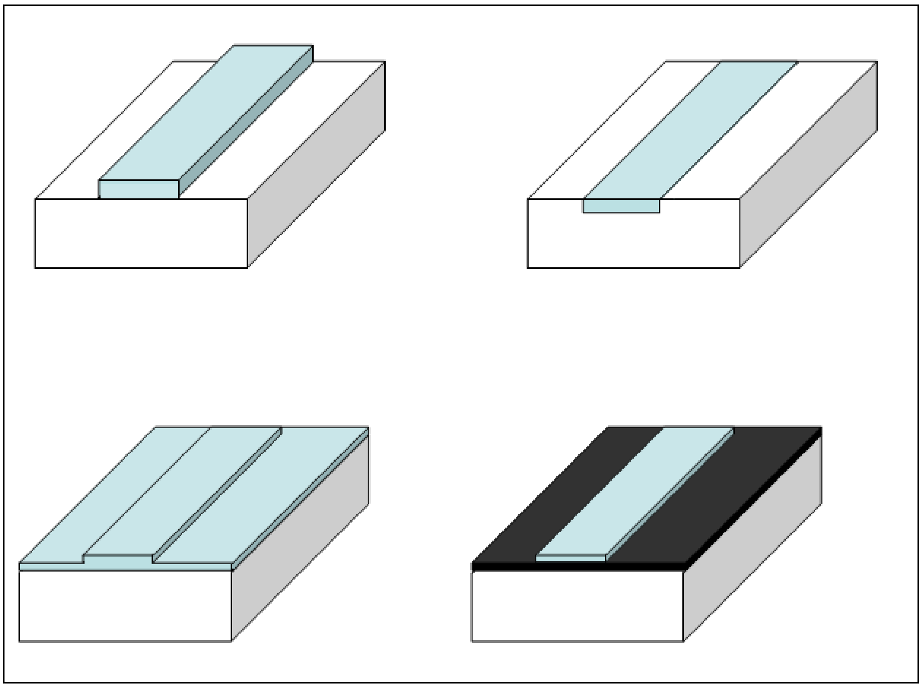

Fig. 3.1. Various types of waveguide geometries: (a) strip; (b) embedded strip; (c) rib or ridge; (d) strip loaded. The darker the shading, the higher the refractive index.

Useful geometries for waveguides include the strip, the embedded-strip, the rib or ridge, and the strip-loaded waveguides illustrated in Fig. 3.1. The exact analysis for some of these geometries is not easy, and approximations are usually used. The reader is referred to specialized books for further readings on this topic [1, 2]. The waveguide may be fabricated in different configurations as illustrated in Fig. 3.1 for the embedded-strip geometry. In this chapter, we will characterize devices based on waveguides splitters, MMI and bends made on Silicon on Insulator technology.

3.1 Sample processing

The waveguides that we will characterize in this chapter are fabricated[2] on SOI wafers (400 nm Si and 1 µm SiO_2). Fig. 3.2 reports a top view image of a chip containing a few structures (Fig. 3.2.a), and a cross section sketch of the Si strip waveguide (Fig. 3.2.b).

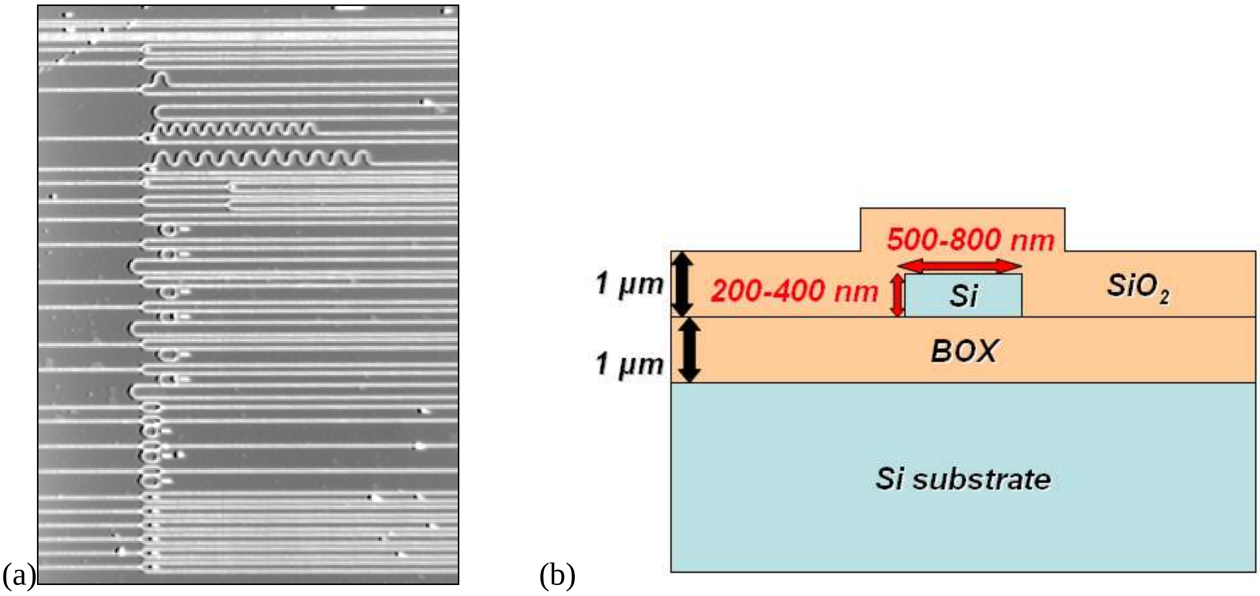

Figure 3.2 Top view image of the sample (a) and cross section of the SOI waveguide (b). Box stands for buried oxide. The top SiO_2 layer is TEOS deposited.

The sample contains regular silicon waveguides. The width of the waveguides varied between 0.5µm and 0.8µm. Different structures were produced such as strip Si waveguides with different lengths and widths, bends and MMI, Y-junctions and splitters 1x8. The samples were diced with polished edges. All these structures were properly matched to a tapering section (about 2 µm wide in-put and in the out-put) in order to optimize the injection of light into and the collection of the light out of each device (Fig. 3.3).

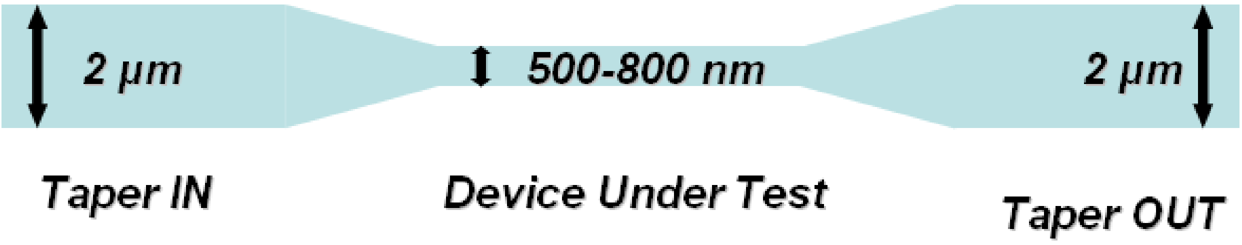

Figure 3.3. Tapering section schema

---

[2] Sample processing and production by Jean Marc Fedeli in LETI (Grenoble, France)

3.2 Experimental set-up

The experimental set-up used for waveguide characterization allows to couple a polarized signal into two-dimensional waveguide devices and to analyze the intensity, the spectrum and the spectral profile of the transmitted light. A schema of the set-up is shown in Figure 3.4.

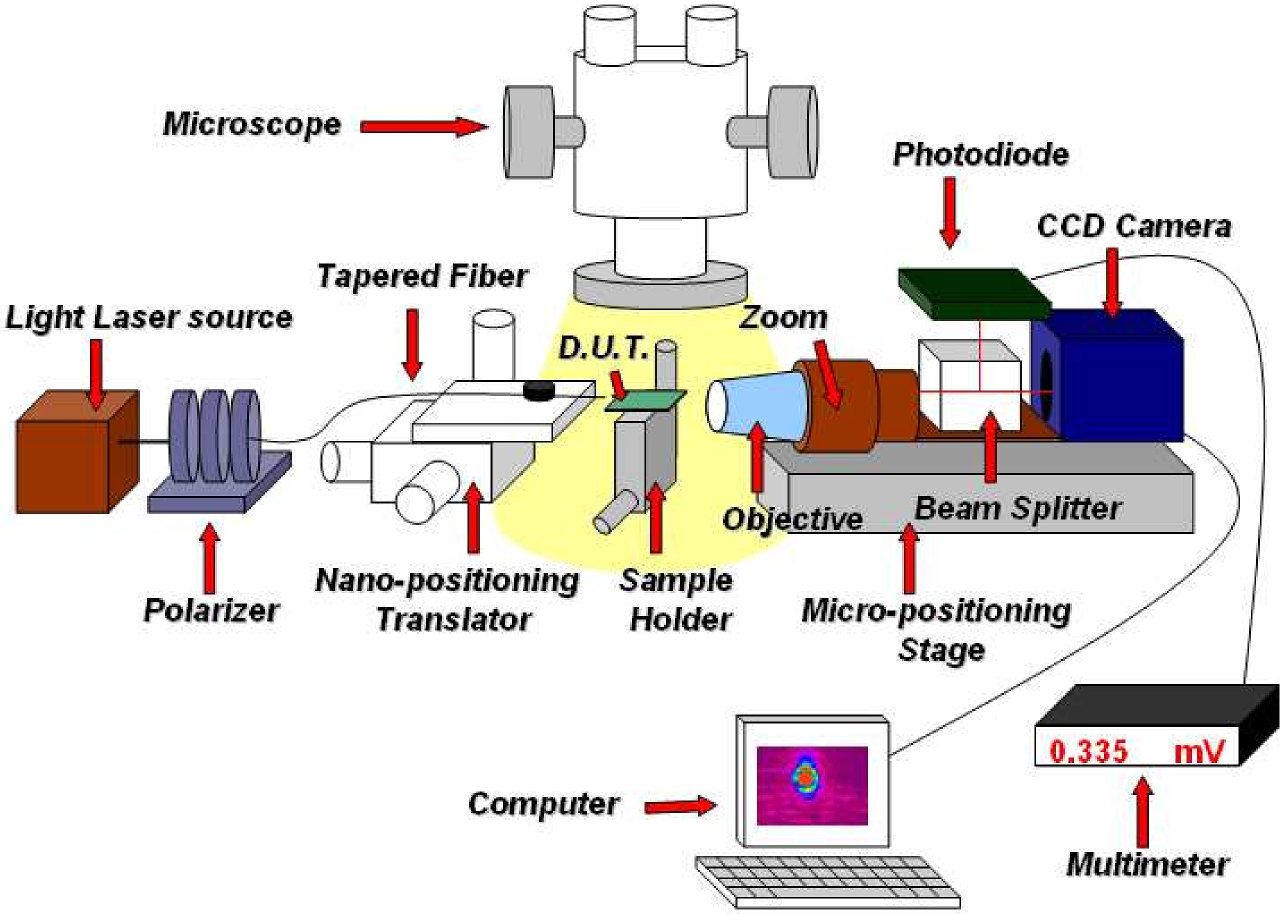

Figure 3.4. Experimental set-up used to characterize waveguides.

3.2.a Coupling system

Light propagation losses through the different passive components were obtained by measurements of the power transmitted as a function of the input signal power. Waveguides and optical devices have been measured by several laser sources according to device materials and geometry. In the case of SOI waveguides, as light laser source, we used a Santec full-band tunable laser (TSL-210F), which is a wide range tunable laser from 1260nm until 1630 nm, with 5 mW of maximum power in the wavelength range. The system is provided by four laser modules: I° module is ranged from 1260 to 1350 nm; II° module 1350-1430 nm; III° module 1430-1530 nm and IV° module 1530-1630 nm. Each module is contained in a box and the laser can be driven by computer software through a GPIB cable. The output light can be coupled to a single-mode optical fiber by a FC/APC connector. To do some measurements with a perfect control of the polarization in our set-up, we directly couple the fiber into a polarization system. The polarization system is made up two polarizers and a half-wave plate, with FC/APC connectors at input and output.

In order to efficiently inject light into thin waveguides, both microscope objectives and tapered/lensed fibers have been used (Fig. 3.5). Single mode optical tapered/lensed fibers offer a convenient way to improve coupling into waveguide devices respect to nearfield microscopic objectives.

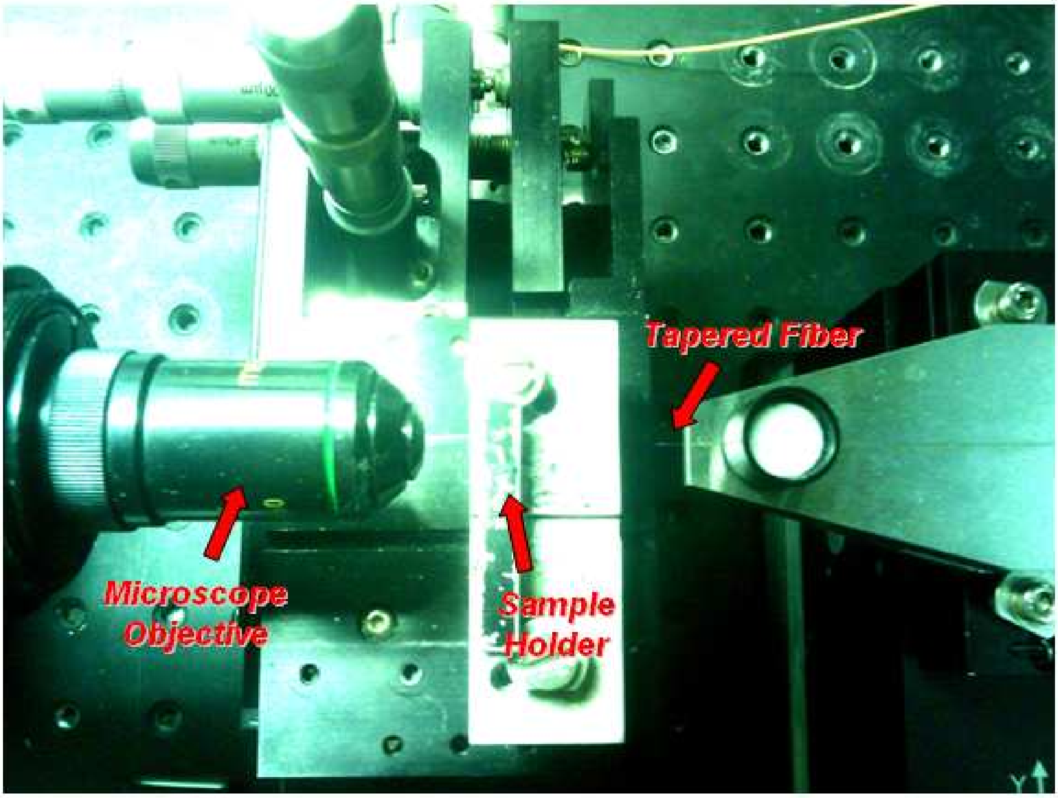

Fig. 3.5. Facilities for coupling the light into the waveguide

To efficiently inject light within thin waveguides, tapered fibers are mounted on a computer-controlled nano-positioning system x-y-z placed on a single track and two angular tilts θy and θz. The smallest displacement of the degree of freedom (x-y-z) is less than 1 nm, if it is performed by the computer-controlled nanopositioning system. Waveguide device sample are also placed on a micro-positioning system with four independent degrees of freedom y, z, θ_y, and θ_z.

In order to align the sample with the mono-mode tapered fiber we dispose of a Stemi 2000-C Zeiss microscope coupled to a CCD camera for a top view. The image in Fig. 3.2.a was actually taken using that camera.

3.2.b Collection system

In front view, i.e. at the sample output facet, we used a microscope objective (40x or 25x) matched to a zoom (x7) mounted on a high-performance CCD camera (in the case of infrared measurements an InGaAs camera) with a video output to a PC or a TV screen in order to image the transmitted light beam coming out from the sample (Fig. 3.6). CCD camera allows to analyze the light beam profile and size at the device output.

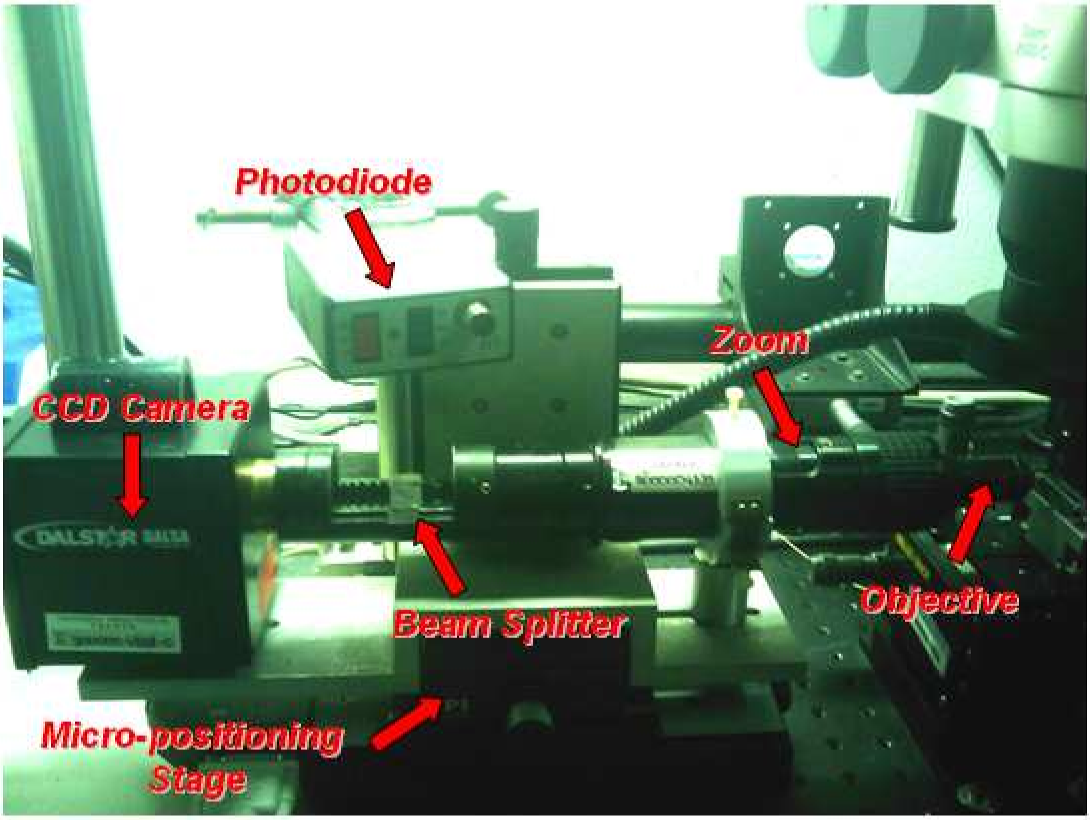

Fig. 3.6. Collection system

Between the objective and the InGaAs camera, a beamsplitter is placed to split part of the output light into a large area photoreceiver with a good sensitivity and a gain tuning. The detector is connected to an optical power-meter to read the power. The microscopic objective, the zoom and camera are mounted on a micropositioning stage motorized along the x-direction or focal direction and manual in the transverse y and z direction. The detector is also mounted on a micro-positioning system placed near the collection system.

3.3 Waveguide losses

There is often confusion between insertion loss and propagation loss of a waveguide. The insertion loss of a device is the total loss associated with introducing that element into a system, and therefore includes both the inherent loss of the waveguides itself and the coupling losses associated with exciting the device. Alternatively, the propagation loss is the loss associated with signal propagation in the device, excluding coupling losses. As the contributions to the loss due to waveguide design or materials properties are associated with the propagation loss, we called all the inherent losses of the waveguides propagation losses. To measure the losses of a waveguide, there are three main experimental techniques, which are the cut-back method, the Fabry-Perot resonance method and the scattered light measurement. In our case, we used the cut-back method, which will be described now.

3.3.a The Cut-back Method

The cut-back method is the simplest method of measuring propagation losses of an optical waveguide. A waveguide of length L_1 is excited by a signal of power I_0 and the output power from the waveguide I_1 is measured. Then the measurements is updated on a waveguide of different lengths either obtained by cutting the waveguide or summing a same coupling loss, then the propagation losses are obtained by a linear fit of the transmitted power versus the waveguide length. In fact, we obtained

$$I_1 = I_0 \exp^{-\alpha L_1} \qquad (3.1)$$

Then a plot in dBs yields both propagation losses in dB/cm and the intercept to zero length the coupling loss.

An important point to notice is the fact that for this calculation, we assumed that the input coupling and the condition of the waveguide end-faces remain constant for all the measurements.

3.3.b Propagation losses of SOI waveguides

The first measurement of propagation losses that we made was on a SOI waveguide of 0.8μm width and 200nm thickness, with tapers input and output of 2μm. The different lengths of channels at our disposition are: 1mm, 2mm, 3mm, 5mm and 7mm. After having traced the curve of the insertions losses as a function of the length of the channel, we found propagation losses (α) of 4.0 ± 1 dB/cm in case of the TE polarization and of 4.1 ± 0.6 dB/cm in case of the TM polarization. The figure 3.7 shows the graph for the TM polarization (β represents the coupling losses).

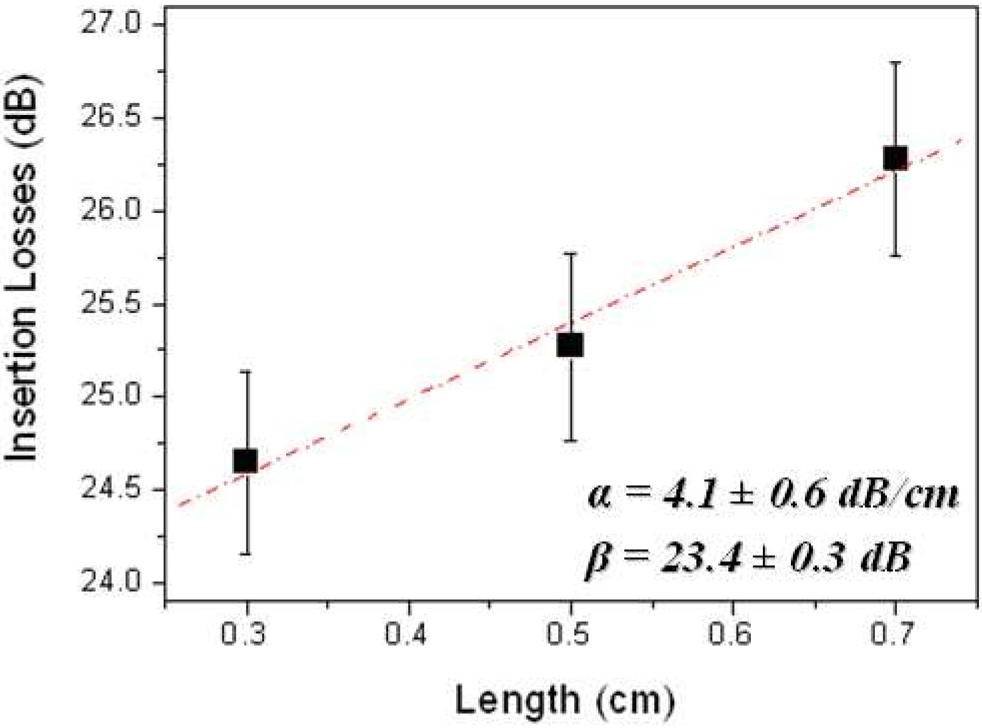

.

Figure 3.7. Propagation losses of 0.8 μm SOI waveguide for TM polarization

3.4 Basics components-losses characterization

3.4.a Splitters 1x2

We characterized splitters 1x2. In this case, a special design was realized to separate the losses due to the propagation along the waveguides from the device under test losses. The design consists in dividing the input signal by a splitter 1x2, and, while one path is just a straight waveguide, the device to be characterized is placed on the other part. Thus the proper losses in the structure are given by comparing the total losses on each path minus 3dB which stands for the ½ split of the signal. An example is given in Fig. 3.8.

3.4.a.1 Y-junction

Y-junctions or Y-branches in optical waveguide are widely used as power divider or combiner in modulator, switches, interferometric devices and semiconductor lasers etc [3]. Its main function is to split the incoming signal into two paths where each path may carry same or different ratio of signal power. It can be considered as the best and simple approach to split light in a planar lightwave circuit. To date, many different designs of Y-junction have been proposed such as sinusoidal bend Y-junction [4], refractive index tapering [5], expanded truncated structural Y branch [6] and asymmetric Y-branch [7]. Sinusoidal bend (S-bend) type perhaps is the most established Y-junction structure due to simplicity in the fabrication process. It uses two flipped S-bend as a building block for its Y-junction structure.

An example of a Y-coupler is shown in Fig. 3.8.a. This example of a Y-coupler comprises single mode waveguides for in- and out coupling with width w = 0.5µm, a taper and a coupling region. The taper region is designed in such a way, that the width at the end is slightly less than 2 times the width of a single mode waveguide. This assures, that only the fundamental mode is allowed to propagate in the beginning of the taper and in the end into the two output waveguides. The next higher mode which would cause additional losses, as it is not supported by the geometry of the single mode waveguides, is not supported in the taper. In the coupling region, both output waveguides have to be treated using coupled mode theory to describe their behaviour. This region is of importance when it comes to design a symmetric Y-coupler with equal power splitting in both output arms. If the angle α is chosen too small, power from one arm is able to couple to the other one being the cause for a different splitting ratio than intended. On the other hand making the angle too large causes additional losses. Therefore, a trade-off has to be found for realizing a specific Y-coupler. Usually S-bends are used to separate the output arms and obtain a good distance between them. Due to manufacturing tolerances like proximity effect and etching, a sharp branching angle is not achieved in most cases and a compromise has to be made to find the optimum angle.

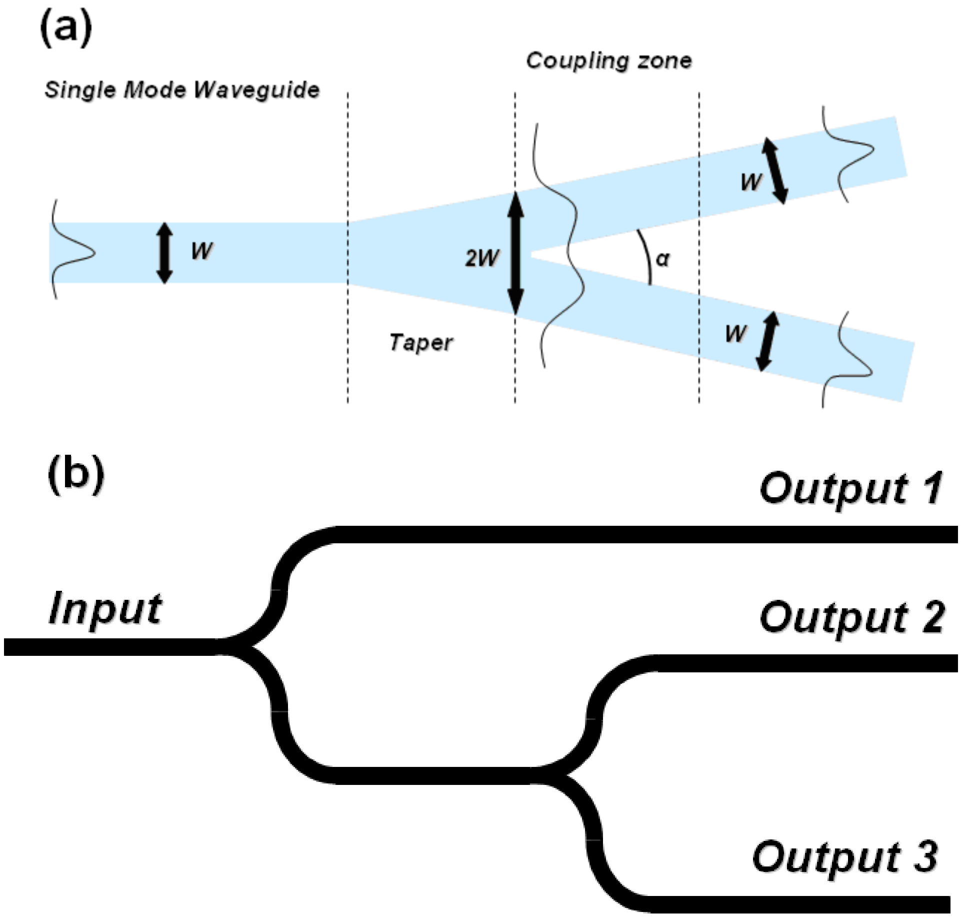

Figure 3.8. Example of Y-junction splitter (a) and design used to measure Y-splitter losses (b)

Table 1 details the measurements performed on Y-junction splitter. Insertions losses values of about 4 and 3dB for TM and TE polarisation, respectively, were found. This adds to the 50% power division among the exit channels. A schematic description of the Y-junction splitter is given on Fig. 3.8.b. It is worth to note that most of these losses are due to the junction point.

Polarization	*TE*	*TM*
Losses Y junction 1 → 2 (0.2µm thickness x 0.5µm width)	3 dB	4 dB

Table 1. Insertions Losses due to the Y-junction for TE and TM polarizations.

The higher TM loss again illustrates the lower confinement of this mode. The same behaviour was found in literature for SOI rib waveguides [4]. The high losses may be reduced if the waveguides are made to initially diverge at a certain rate so that the transition remains adiabatic. Another explanation of the high losses can be due to the fabrication method, which led to a non ideal feature between the two diverging arms of the y-junction. This is likely to scatter light out of the waveguide structure. To reduce the loss caused by this undesirable feature its size may be reduced using finer photolithography and etching methods. It’s important to note that all these measurements were made at 1550nm, and so no wavelengths dependence measurements were done on these structures.

3.4.a.2 Multimode Interferometer (MMI)

Multimode interferometers (MMI) are other kind of splitters 1x2, which could be fabricated with simple input and outputs (standard MMI), or with tapered input and outputs (tapered MMI). Self-imaging of periodic objects illuminated by coherent light was first described more than 150 years ago [8]. Self-focusing (graded index) waveguides can also produce periodic real images of an object [9]. However, the possibility of achieving self-imaging in uniform index slab waveguides was first suggested by Bryngdahl [10] and explained in more detail by Ulrich [11], [12]. The principle can be stated as follows: “*Self-imaging is a property of multimode waveguides by which an input field profile is reproduced in single or multiple images at periodic intervals along the propagation direction of the guide.*”

A complete description of the principle of the multimode interferometer is detailed in appendix. A description of the two MMI structures and the Y-junction is given in Fig 3.9. Using the same method described above, we calculated the losses for each structure in the two optical chips under study. An example of the results on the optical losses in a MMI splitter device is given in table 3.

Figure 3.9. Schematic description of the splitters 1x2.

The results on the proper losses obtained for three different kinds of 1→2 splitters are presented in table 2. The separation of the data for the MMI losses is due to the fact that the waveguides have different dimensions, i.e. the devices have different dimensions (in one case 0.2µm thickness x 0.5µm width and in the other case 0.4µm thickness x 0.7µm width).

Devices	*Polarization*	
	TM	*TE*
MMI taper 1 → 2 (0.2x0.5µm)	5dB	1dB
MMI standard 1 → 2 (0.2x0.5µm)	5dB	1dB
MMI taper 1 → 2 (0.4x0.7µm)	2dB	1dB
MMI standard 1 → 2 (0.4x0.7µm)	2dB	2dB
Y junction 1 → 2 (0.2x0.5µm)	4dB	3dB

Table 2. Insertions losses on basic building blocks.

We looked at both TE and TM polarization, and we obtained comparable values. This result is very important for our study, as we want to characterize SOI based structures for both TE and TM polarizations. Analysing results of table 2, it looks like TE mode propagation is less attenuated in MMI of small dimensions than in Y-junction, while the opposite is true for TM mode propagation. Another important observation is the fact that no important differences between the losses in MMI device with taper inputs or standard inputs have been detected for TE, whatever are the dimensions of the device. As for the Y-splitter, these measurements were done at λ=1550nm, and no wavelengths dependence measurements were done on these structures.

Polarization	*TE*			*TM*		
Output (see Fig. 3.8.b)	1	2	3	1	2	3
Insertions losses (dB)	34.5	38.6	39.6	33.1	41.6	41.6

Table 3.Optical power transmitted and total losses through an MMI standard device (0.2x0.5µm).

The table 3 showed the imbalance in the MMI standard device (the outputs are the same as for the Y-splitter described in Fig. 3.8.b, as the structure is identical for both Y-splitter and MMI). The maximum imbalance found was 1dB in the case of TE polarization, which is a very good value.

3.4.b Splitters 1x8

In Fig. 3.10, a picture of splitters 1x8 (left hand) and a front views images of the transmitted light, TE mode in the top and TM mode in the bottom, respectively are shown. We noticed on Fig. 3.10 that the focus of the camera change if the mode is on the edge of the active area of the CCD confront to when he is centered on it. For the measurements, we focused each optical mode on the center of the active area of our camera, in order to have confrontable values. The total losses including insertions, coupling, intersections and the proper losses in the waveguides are given in table 4 for each one of the eight spots of the splitter. The maximum imbalance found was 7% in TE case and 3.5% in TM case. Two remarks are worth to be made: the intensity and thus the losses are similar in each one of the eight paths for TM polarization, while for TE polarization, the imbalance is significant; and the structure is more transparent for TM mode than TE mode. This last point can be explained by the higher imbalance ratio in case of TE polarization.

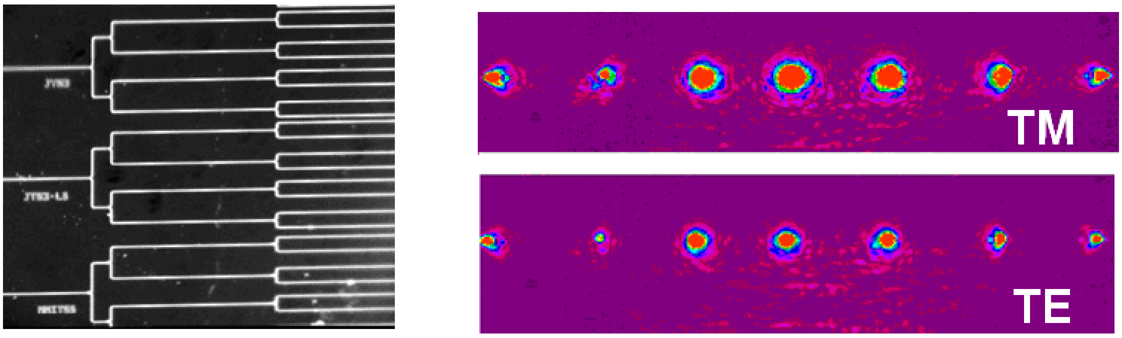

Figure 3.10. Top view image of a splitter 1x8 (left) and CCD image of the transmitted spot lights in both TM and TE modes (right) (λ=1550nm, P_{in}=3mW)

Polarization	TE mode							
Output	1	2	3	4	5	6	7	8
Total Losses (dB)	47	47.7	50.6	48.7	49	48.5	48.2	48.1
Polarization	TM mode							
Output	1	2	3	4	5	6	7	8
Total losses (dB)	42.8	42.8	43.1	42.58	42.2	41.92	42.1	41.7

Table 4. Insertions losses for TE and TM polarizations on 1x8 splitters.

3.4.c Bends

When light is propagating in a curved waveguide the mode gets shifted toward the outer edge. In sharp strip waveguide bends this effect results in a possibility of mode radiation, reflection due to phase mismatch between the mode in the bend and in the straight section, and enhancement of losses due to increased interaction of the mode with the sidewall surface roughness. The simplest approximation to describe radiation loss [13] shows that bending loss is exponentially dependent on the bend radius R:

$$\alpha = K * \exp(-\beta R(\frac{2\Delta n_{eff}}{n_{eff}})^{\frac{3}{2}}) \qquad (3.2)$$

where K depends on the refractive indices of cladding and core and on waveguide thickness, and β is the mode propagation constant. Δn_{eff} is the difference between the mode effective index n_{eff} and the cladding index. Equation (3.2) assumes that $\Delta n_{eff} / n_{eff}$ is small and that the bending is a small perturbation on the modal intensity profile of the straight guiding mode.

Although more sophisticated methods typically used for calculations of the bending losses, such as beam propagation or mode expansion, become inaccurate for submicron cross-section high index contrast SOI strip waveguides, estimations shows that for R=1µm the bending loss in SOI strip waveguide can be expected to be of the order of 0.1 dB/turn in good correspondence with the experimentally measured number. These estimations do not include, however, the role of the sidewall surface roughness. Observed dependence of bending loss on polarization indicates that the surface roughness is an important factor defining the losses. Analogous polarization dependence was previously observed in Ref. [14, 15], where it was explained by higher interaction of the TM mode with the surface roughness at the bend.

For our experiments, we considered different structures of bends. Fig. 3.11 schematically represents a portion of the design where this kind of structures was realized. Two different structures were studied for a waveguide width of 0.7µm and the results are presented in Table 5. We measured also bends in 0.5µm width waveguides. In both cases the width of the waveguide is 200nm. The results in this case are presented in Table 6. Again we performed measurements for both TE and TM polarization.

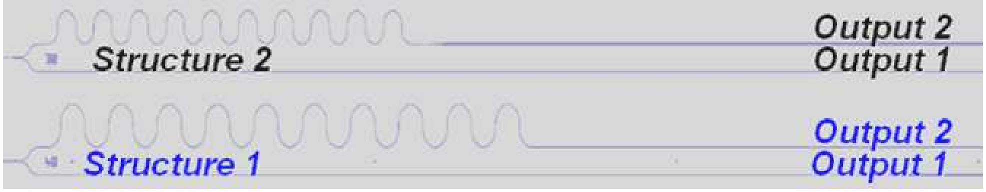

Figure 3.11. A schematic description of the bends 90^{o} structures, the inset numbers refer to the corresponding measured optical losses at 1550nm, as reported in table 5.

Structure	Polarization	TM	TE
1	90^o Bend with R=40μm	0.02 dB/bend	0.04 dB/bend
2	90^o Bend with R=30μm	0.02 dB/bend	0.02 dB/bend

Table 5. Optical losses on 90^o bends.

The more important result is that the losses are very small. We measured losses of about 0.02dB/bend in TM mode for different radius (structures 1 and 2), and similar results have been obtained for TE polarization, within the experimental errors.

By comparing the results of table 5 and 6, one can deduce that TM mode is not transmitted in very thin (0.5μm) and curved bends (R<10 μm), due to higher propagation losses and higher interaction with the surface roughness at the bend, while in larger circuits and larger bends the losses are very small (0.02dB/bend). At the same time a slight dependence on the dimension and the bend radius was observed for the TE mode.

Bend Type	Polarization	
	TM	TE
90^o Bend with R=2μm	---	0.06 dB/bend
90^o Bend with R=5μm	---	0.02 dB/bend

Table 6. Optical losses on 90^o bends for a waveguide width of 0.3 μm

3.5 Conclusion

This chapter was dedicated to optical losses measurements performed at 1550nm in several basic components in Silicon On Insulator waveguides. Structures such as Y-junctions, MMIs and bends were considered. The results show that state of the art processing yields low losses. These results are basic to the development of the SOI-based SCISSOR and CROW structures described in last chapter.

References

[1]. A. W. Snyder and J. D. Love, *Chapman & Hall, New York*, 1983.

[2]. K. Okamoto, *New York: Academic*, 2006.

[3]. H. Hatami-Hanza, P.L. Chu and M.J.Lederer, *IEEE Photonics Technology Letters* **6**, 528-530 (1994).

[4]. A.G Rickman and G.T Reed, *IEE Proc.-Optoelectron* **141**, 391-393 (1994).

[5]. M. H. Hu, J. Z. Huang, R. Scarmozzino, M. Levy, and R. M. Osgood, *IEEE Photonics Technology Letters* **9**, 203-205 (1997).

[6]. H.P. Chan, S.Y. Cheng and P.S. Chung, *Electronics Letters* **32**, 652-654 (1996).

[7]. H. Uetsuka, T. Hakuta, H. Okano, and T. Shiota, *OFC'96 Technical Digest,* 176-177 (1996).

[8]. H. F. Talbot, *London, Edinburgh Philosophical Mag., J. Sci.* **9**, 401407 (1836).

[9]. D. Marcuse, *Light Transmission Optics.* New York: Van Nostrand Reinhold (1972).

[10]. 0. Bryngdahl, *J. Opt. Soc. Amer.* **63**, 41-19 (1973).

[11]. R. Ulrich, *Optics Commun.* **13**, 259-264 (1975).

[12]. R. Ulrich, *Nouv. Rev. Optique* **6**, 253-262 (1975).

[13]. E. A. Marcatili, *Bell Syst. Tech. J.* **48**, 2103 (1969).

[14]. D.R.Lim, PhD thesis, M.I.T. (2000).

[15]. Y. A. Vlasov and S. J. McNab, *Opt. Express* **12**, 1622–1631 (2004).

Chapter four

NanoSi slot waveguides

Si photonics technology has made major advances in terms of design, fabrication, and device implementation [1]. At present days, it is at a turn-around point between technical development and commercial opportunities. The progress in Si photonics fabrication technology has enabled the realization of photonic structures with deep-submicron feature size in ultrahigh-index contrast materials, most prominently, in silicon-on-insulator (SOI). In addition to waveguide structures such as silicon wires [2, 3] and photonic crystal slab waveguides [4], slot waveguides have been proposed [5-7]. As silicon nanocrystals (Si-nc) embedded in SiO_2 have low refractive index (in the range 1.5-2.0 according to the Si excess), their use in conventional waveguides results in large cross-section and weak light confinement. The slot waveguide is a high-index contrast photonic structure with deep-submicron feature size that can help in solving such a problem. It consists of a thin layer of low-index material sandwiched by two high-index walls or layers (for vertical or horizontal configuration, respectively) (Fig. 4.1).

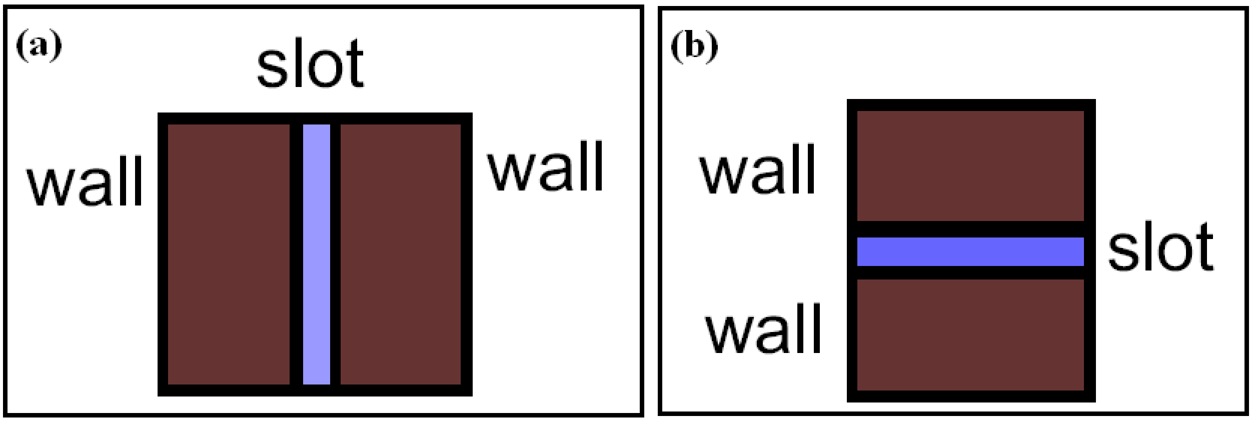

Figure 4.1. Schema of vertical (a) and horizontal (b) slot waveguides

This is the basic principle of the slot waveguide. Compared to conventional waveguides, where the main part of the optical field is confined within the high index core, a large fraction of the guided mode is in the low index layer. This occurs only for the polarization mode whose electric field is perpendicular to the slot interfaces: TM polarization for the horizontal slot and TE polarization for the vertical one. The field is affected by a discontinuity at the slot-wall interfaces and this increases the overlap of the optical field evanescent tails within the slot. If the slot width is smaller than the decay length of the field, it is possible to have a pile-up of the evanescent tails, thus enhancing the field intensity in this region with respect to the field confined in the walls. In this work, we study theoretically and experimentally nano-Si slot waveguide based photonic structures, both waveguides and ring resonators. Horizontal slot waveguides filled with Si-nc have been realized and characterized in terms of propagation losses as a function of the layer deposition conditions (i.e. Si excess and annealing temperature). In a second part, we present experimental results of resonant optical cavities such single and double ring resonators coupled to the horizontal slot waveguides with very high quality factors.

4.1 Theoretical approach of the slot waveguides

The principle of operation of a slot-waveguide is based on the discontinuity of the electric field (E-field) at high-refractive-index-contrast interfaces. Maxwell's equations state that, to satisfy the continuity of the normal component of the electric displacement field **D** at an interface, the corresponding **E**-field must undergo a discontinuity with higher amplitude in the low-refractive-index side. That is, at an interface between two regions of dielectric constants ε_s and ε_w, respectively:

$$D_{\perp w} = D_{\perp s} \rightarrow \varepsilon_w E_{\perp w} = \varepsilon_s E_{\perp s} \rightarrow n_w^2 E_{\perp w} = n_s^2 E_{\perp s} \qquad (4.1)$$

As we have $n^2_w >> n^2_s$, $E_{\perp w} << E_{\perp s}$.

The slot critical dimension (distance between the high-index slabs or strips) is comparable to the exponential decay length of the fundamental eigenmode of the guided-wave structure, the resulting E-field normal to the high-index-contrast interfaces is enhanced in the slot and remains high across it. The power density in the slot is much higher than that in the high-index regions. Since wave propagation is due to total internal reflection, there is no interference effect involved and the slot-structure exhibits very low wavelength sensitivity.

For example, in a case of two coupled waveguides separated by a distance w_s (slot region), the electromagnetic field of the two decoupled waveguides must be matched in the middle of the waveguide separation. When the distance becomes of the order of the decay length of the field, the absolute value in the middle of the slot starts to take a large value. Decreasing further w_s the two exponential tails do not decrease to zero and the field in the middle increases because the continuity condition of the electromagnetic field. Therefore, the amplitude in the slot increases as w_s decreases until to reach the value imposed by the equation 4.1. Figure 4.2 shows an example of the electromagnetic field profile of a Si-based vertical slot waveguide, for different slot thicknesses w_S. From left to right the slot thickness varies from 500nm until 20nm. We noticed that the amplitude of the EM field in the slot region increases as the slot decreases, because the power carried by the EM fields is kept constant. Nevertheless the amplitude of the discontinuity at interface is always equal to n^2_{Si}/n^2_{Air}.

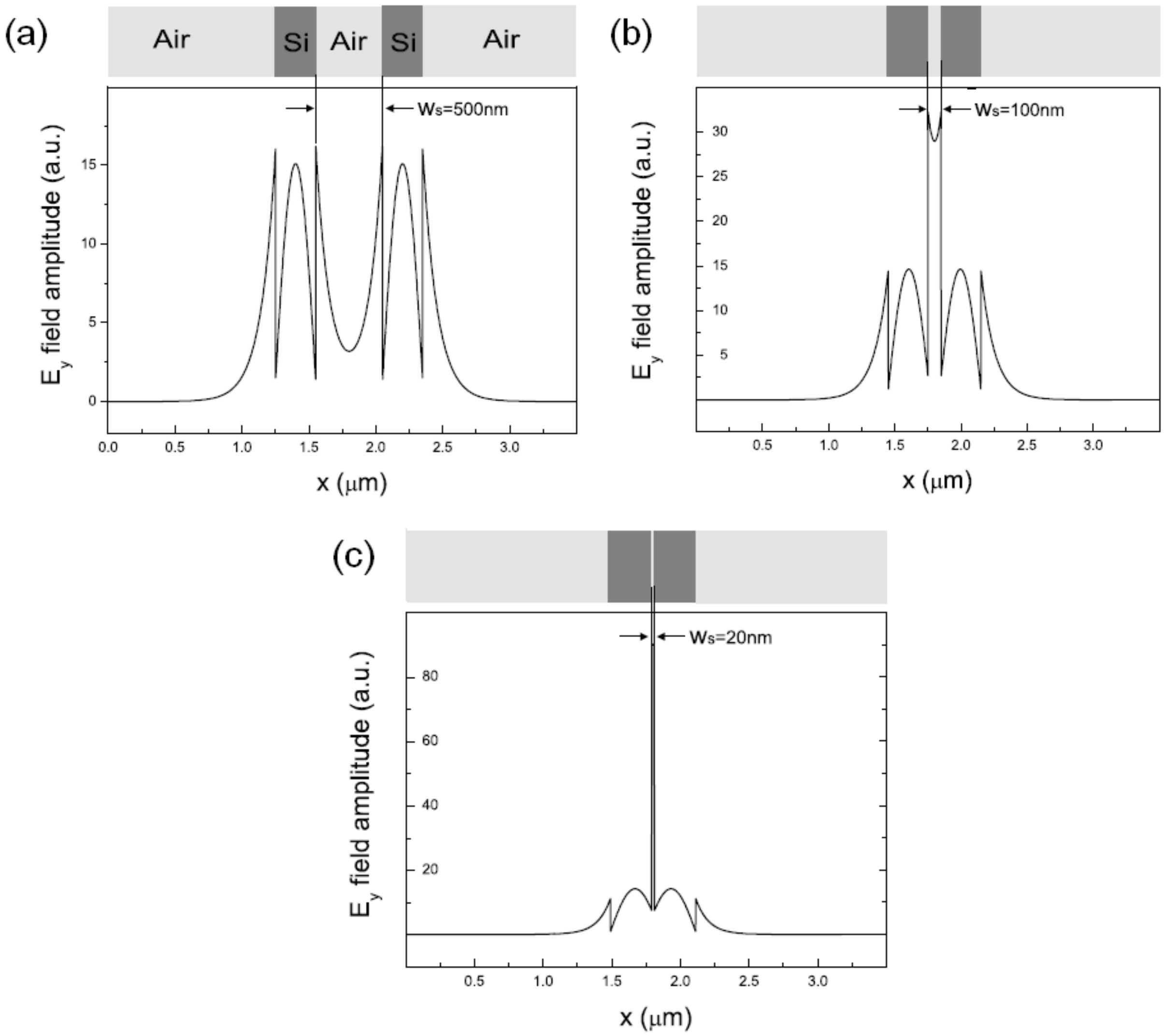

Fig. 4.2. Electromagnetic profiles of the fundamental symmetric mode of a coupled waveguide system for w_S = 500nm (a), 100nm (b) and 50nm (c) (Francesco Riboli Thesis 2005)

4.2 Processing of Slot waveguides

4.2.a Vertical Slot waveguides[3]

The slot waveguide was designed for optimum field enhancement [8]. The optimum design is a 100nm-150nm (W_S) wide slot into a monocristalline silicon waveguide with a width (W) of approximately 500nm and a height (h) of 200-300nm (Fig. 4.3.a). For nonlinear applications the slot is filled with SiO_x. After high temperature annealing the whole structure is finally covered by stoichiometric SiO_2.

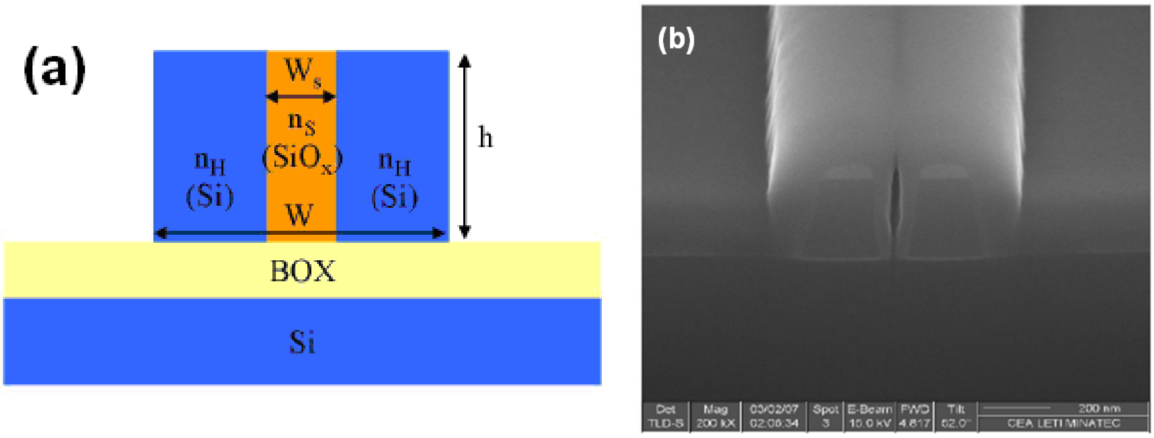

Fig. 4.3. (a) View of a vertical slot waveguide (Ws=100-150nm, h=200-300nm, W=500nm, n_H high index medium : silicon, n_S small index medium : silicon nanocrystals within SiO2); (b) SEM cross-section view of a 500nm wide slot waveguide (Ws=120nm) just after SiOx cladding deposition by LPCVD.

DUV lithography 193nm on ASML equipment was used for the purpose of future mass manufacturing. Starting on wafers with 380nm silicon thickness, 150nm thick SiO_2 was deposited as hard mask. After definition of the patterns and hard mask etching, silicon was etched to the buried oxide. Finally a non-stoechiometric SiO_x layer was deposited by LPCVD or PECVD and annealed at 1100°C in a RTP furnace to induce silicon nanocrystals formation. The fabrication process of these slot waveguides was done on a CMOS fabrication line. For mass manufacturing with acceptable fabrication margins, Deep-UV 193nm lithography on ASM1100 scanner was experimented with different exposition doses. Slot waveguides with slots as thin as 120 and 100nm were successfully defined with high reproducibility.

On Fig. 4.3.b is reported a FIB-SEM cross-section view of a 500nm wide slot waveguide with a 120nm wide slot which has been covered with SiO_x LPCVD. It is obvious that slot waveguide is not filled even if LPCVD deposition shows a better filling ability than PECVD deposition (not showed) since it is more conformal. But the main reason why air bubble is present in the slot comes from the silicon etching step: silicon profiles bowing phenomena occurs and a significant hard mask layer

---

[3] Sample processing and production by Jean Marc Fedeli in CEA-LETI (Grenoble, France)

still remains after etching that, in addition, increases the aspect ratio of the slot and could induce sidewalls roughness. The combination of aspect ratio increase and deposition accumulation at the top of the silicon results in air bubble formation especially if the deposition process is not very conformal such as PECVD.

Thus control of the slopes of the silicon waveguide is one of the key parameters to a good filling of the slot. Further refinements on the etching process and the hard mask optimization should lead to slot waveguides filled with silicon nanocrystals with mass manufacturing process.

4.2.b Horizontal Slot waveguides

In order to reduce processing difficulties encountered in vertical slot waveguides, an alternative process was developed. Design and optimization of the slot geometrical parameters to achieve minimum effective area (i.e. maximum field confinement) have been reported in [8], where the influence of the refractive index in the slot region has been studied too. A minimum effective area of 0.1 μm^2 was found with a slot waveguide width of 350 nm. This waveguide width ensures single mode TM propagation. However surface roughness causes significant losses at this width [9]. Thus to reduce the propagation losses, a width of about 500 nm has been chosen to fabricate the waveguides. At such a width, the second order TM mode is also present. However, it is extremely lossy being very close to the cut-off condition and spatially localized at the waveguide surface.

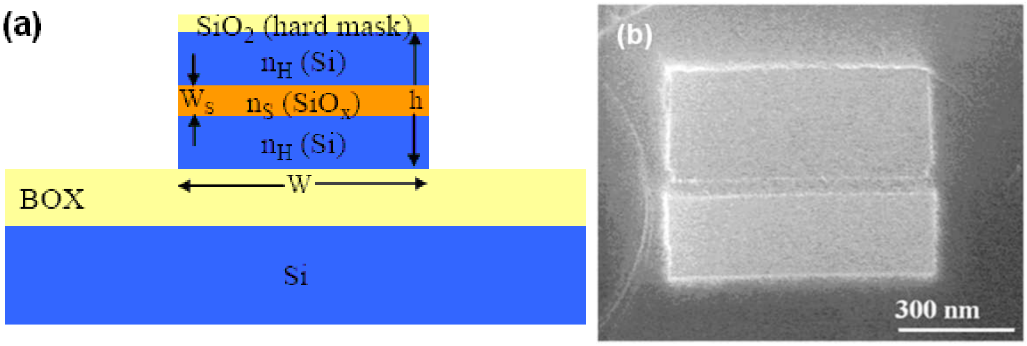

Fig. 4.4. (a) View of a sandwiched waveguide without SiO2 cladding layer;
(b) SEM image (cross section) of an horizontal waveguide.

The horizontal slot waveguide structure is composed by a Silicon-Rich-Silicon-Oxide (SRSO) layer (50-100 nm thick) placed between two silicon waveguides (200-300 nm thick) (Fig. 4.4.a). The starting wafer was a 200 mm SOI wafers with 220 nm thick crystalline silicon and 2 µm thick buried oxide (BOX). SRSO was deposited by plasma enhanced chemical vapour deposition (PECVD) by using different deposition conditions. Reference sample with SiO_2 has been deposited too. Various annealing treatments in inert (N_2) atmosphere (from 600 to 1000°C) were experienced to induce Si-nc formation. Then, low loss hydrogenated amorphous silicon (a-Si) was deposited at 350°C and followed by 150 nm TEOS SiO_2 deposition acting as an hard mask [10]. 193 nm deep-UV lithography and hard mask etching was used to define sub-micrometer wide waveguides. The three layers (amorphous silicon, SRSO, and monocrystalline silicon) were etched sequentially down to the BOX. As a final step, the horizontal slot waveguides were covered by SiO_2. Scanning electron microscopy cross section of a typical horizontal slot waveguide is shown in Fig. 4.4.b. Its geometrical parameters are: 50 nm thick SRSO slot, 555nm waveguide height and 650 nm waveguide width. After an optimisation of the etching procedure, we have obtained horizontal slot waveguides of smaller width, about 500 nm [10].

4.3 Waveguide losses

4.3.a Propagation Losses on Vertical slot waveguides

We made first losses measurements on the vertical slot waveguides. To do the cut-back measurements without cutting the sample, all the guides have a "taper" of 2 μm width in and out, and the length of the slot waveguides vary from 1 to 7mm. Figure 4.5 shows a design of the mask we create to do these measurements (W represents the width of the waveguide). Another function of the tapering is to allow an easy and efficient in and out coupling of the light into the chip.

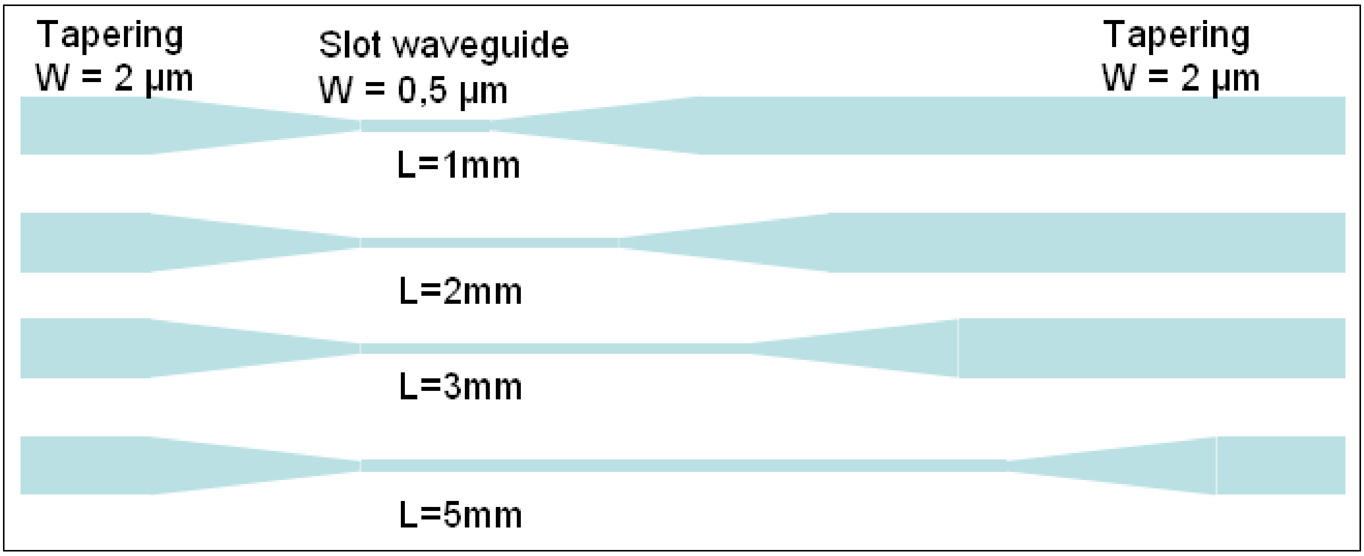

Fig. 4.5. Design of the structures created to measure the losses of the slot waveguides

For this waveguide, the output mode of the waveguide was observed only at the first two lengths: 1mm and 2mm. As the figure 4.6 shows, no signal was observed at lengths larger than 2mm.

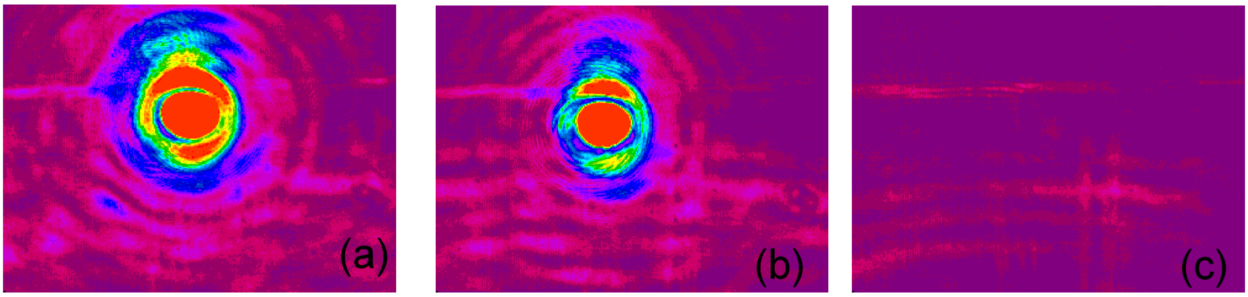

Figure 4.6. Images of the output mode taken by CCD camera for slot waveguides of lengths 1mm (a), 2mm (b) and 3mm (c) (I_0=10mW)

As we have only two points to do the Cut-back measurements, we supposed that the propagation losses in our waveguide are linear. Results are represented in Figure 4.7. We inserted in the Figure a point for the insertions losses at length L=3mm. As we can observe, the insertions losses at this length should be around 45dB, which is very high and by consequence very difficult to be detected by our set-up. We found propagation losses of about 30dB/cm for both polarizations. This implies that most of the losses are due to scattering losses caused by the scarce filling of the slot region.

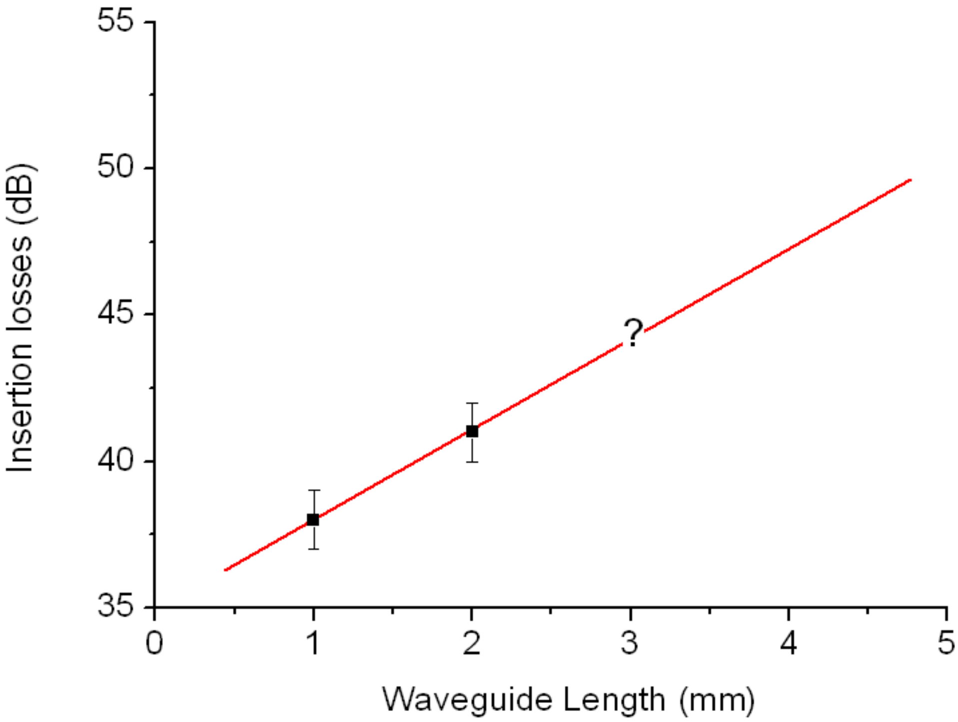

Figure 4.7. Cut-back on vertical slot waveguide

The presence of air bubble inside the slot, as we observe in Figure 4.3.b., can create very high losses inside the waveguide, for both TE and TM modes.

4.3.b Propagation Losses on horizontal slot waveguides

In order to reduce high losses encountered above due to processing problems, horizontal slot waveguides were developed.

A preliminary study on the material (in particular, correlation between refractive index and deposition parameters) has been performed in ref. [11]. Different deposition conditions (i.e. Si excess in the SRSO layer, from 8% to 10%) and thermal annealing treatment (from 600 up to 1000 °C) have been used to correlate already optimized material properties [11] to optical losses within the horizontal slot waveguide configuration. It is worth to remind that high Si content for a fixed annealing temperature or high annealing temperature for a fixed Si excess imply a large refractive index (thus influencing both linear and nonlinear optical properties) [11].

A systematic study/design of the slot geometrical parameters has been already performed aiming at optimizing the modal confinement factor [8], where the percentage of silicon excess inside the slot was studied in order to have the highest value of n_g*FF for the waveguide [12], where n_g represents the group index and FF the filling factor of the slot waveguide (Fig. 4.8). We define FF the *energy filling factor* which measures the degree of concentration of the energy inside the slot waveguide.

$$FF = \frac{\int_A E \wedge H \, dxdy}{\int_D E \wedge H \, dxdy} \tag{4.2}$$

Where A is the slot region, D denotes the whole waveguide, E denotes the electric field, H denotes the magnetic field and $E \wedge H$ denotes the Poynting vector, which represents the energy flux of the electromagnetic field.

The best results were found for slot refractive index values around 1.5, which correspond to a silicon excess of 8-10% and an annealing temperature of about 1000 °C [11].

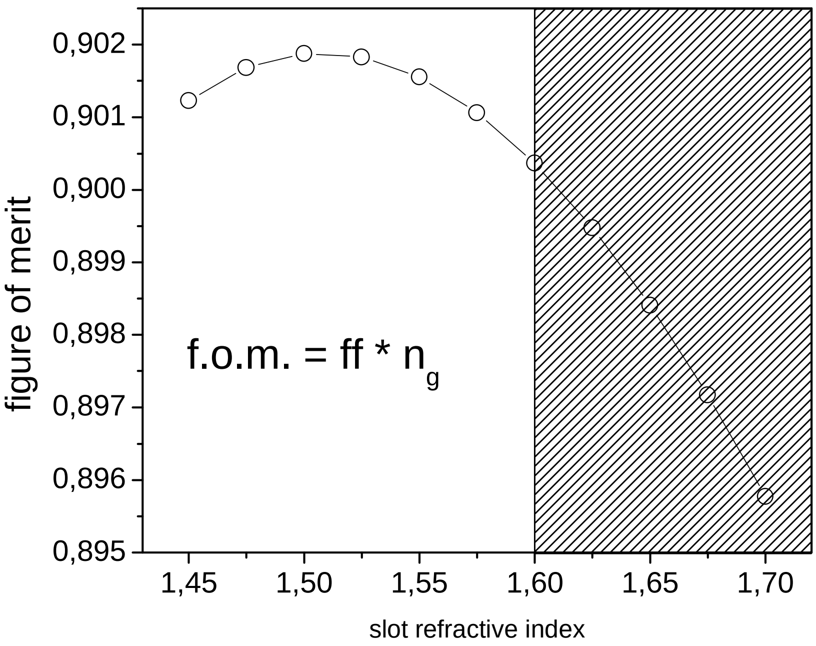

Figure 4.8. Figure of merit of horizontal slot waveguides versus the refractive index of the slot[4]

To further select the optimum Si excess, one has to take into account excited carrier absorption, which depends on Si-nc size and densities [11] and [13-14]. 8-10% is the optimum Si excess for PECVD samples to have low pump-induced losses due to carrier absorption, to show large non-linear properties [13], efficient light emission [15] and low propagation losses.

Propagation losses have been determined from transmission measurements. To control the polarization, a fiber polarizer has been employed between the laser and the input fiber while a polarizer filter has been used in the collection system. Propagation losses of these waveguides have been measured at 1.55 μm. A dedicated layout structure allows the determination of the propagation losses independently on the coupling ones. It is shown in the inset of Fig. 4.9: it consists of a waveguide split into two channels. Since the two channels have different lengths, the ratio of the intensities at the outputs gives the linear propagation losses. Clearly, the balance of the splitter has been carefully checked in waveguides with the same output path length.

---

[4] Calculation courtesy of Alessandro Pitanti

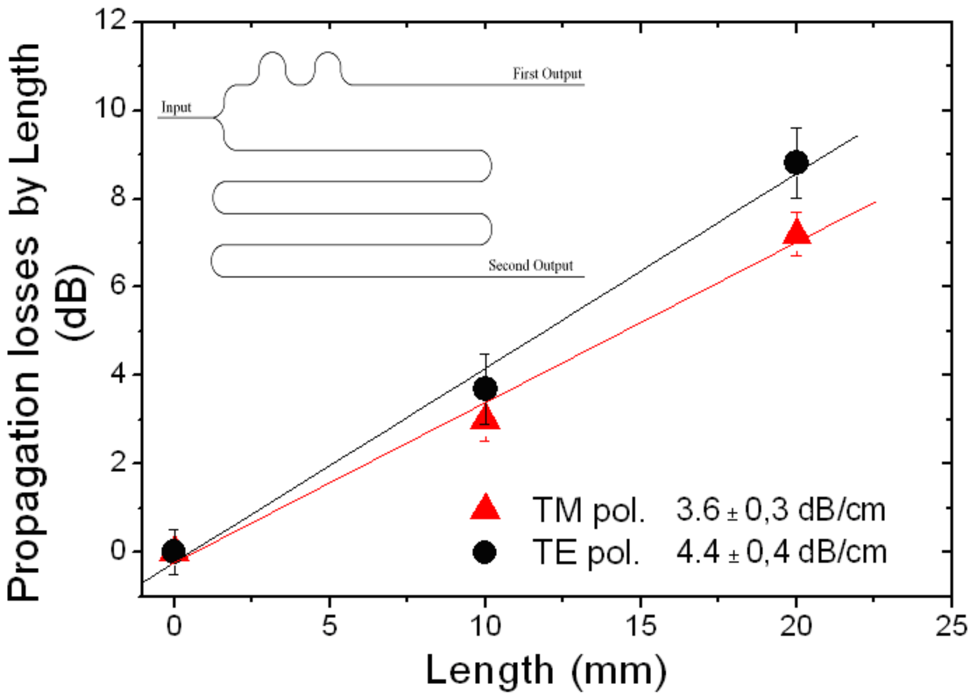

Fig. 4.9. Propagation losses of nano-Si slot waveguide with 8% Si excess annealed at 1000°C measured at 1550nm in TM and TE polarization. Inset: Top-view scheme of the waveguides on the mask.

Fig. 4.9 shows a graph of the measurements for a slot waveguide with 8% Si excess annealed at 1000°C. Propagation losses of 3.6 dB/cm have been measured at 1550 nm for the quasi-TM polarization, while about 4.4 dB/cm for the quasi-TE polarization. Such optical loss values can be attributed to the fact that a large fraction of the optical mode is confined within the slot which reduces the effects of the wall roughness and to the good layer interfaces obtained by the deposition technique used. This is supported by losses of 7.2 dB/cm found for the reference waveguide (slot waveguide with SiO_2). Similar results have been found in single slot waveguides formed by a-Si/SiO_2 [16, 17].

In Table 1, a summary of the waveguide losses as a function of the material parameters is shown.

Si excess	*Annealing temperature (°C)*	*Propagation losses*	
		quasi-TM (dB/cm)	*quasi-TE (dB/cm)*
0% (TEOS SiO_2)	600	7.2 ± 0.1	7.6 ± 0.8
8%	800	4.6 ± 0.3	5.4 ± 0.4
8%	1000	3.6 ± 0.3	4.4 ± 0.4
10%	600	4.7 ± 0.7	5.4 ± 0.6
10%	800	4.4 ± 0.7	-
10%	1000	3 ± 0.2	3.9 ± 1.1

Table 1. Propagations losses for different slot waveguides for quasi-TE and -TM polarization at 1550 nm.

Propagation losses decrease with increasing the Si excess or when the annealing temperature rises. It is worth noting that we were able to reach propagation losses as low as 3 dB/cm for quasi-TM polarization (sample with 10% of excess Si and annealed at 1000 °C), which is the best result reported for slot waveguides of such a small width. This is a consequence of the increasing of the refractive index as well as the result of a material optimization to minimize carrier absorption losses due to the Si-nc [14].

4.4 Ring Resonator

Using standard silicon processing techniques, ring resonators have been developed for chip-scale silicon photonic components including optical fibers, switches, and lasers. Variation of the silicon ring resonator include lateral and vertical coupled rings, disks, toroids, and cascaded resonators. The high Q-factors and small mode volumes of these structures lead to strong electric field enhancement in the resonators. While the overall dimensions of the resonators are of the order of microns, the gap between the resonators and adjacent bus waveguides is typically on the nanometer scale. Light in the bus waveguide can be evanescently coupled through the gap into a whispering gallery mode of the resonator if the proper phase matching conditions exist. Light is trapped within the ring by total internal reflection. Over the past few years, the utility of microring and microdisk resonators has expanded to biological applications. Resonance shifts, intensity changes, and changes to the quality factor have been used, for example, to detect the presence of chemicals or biological molecules attached to microring resonators.

4.4.a Theory of ring resonator

In order to understand the principle of the ring resonators, we will present an analysis of microring resonators. A general design of the microring resonator coupled to a waveguide is shown on Fig. 4.10.

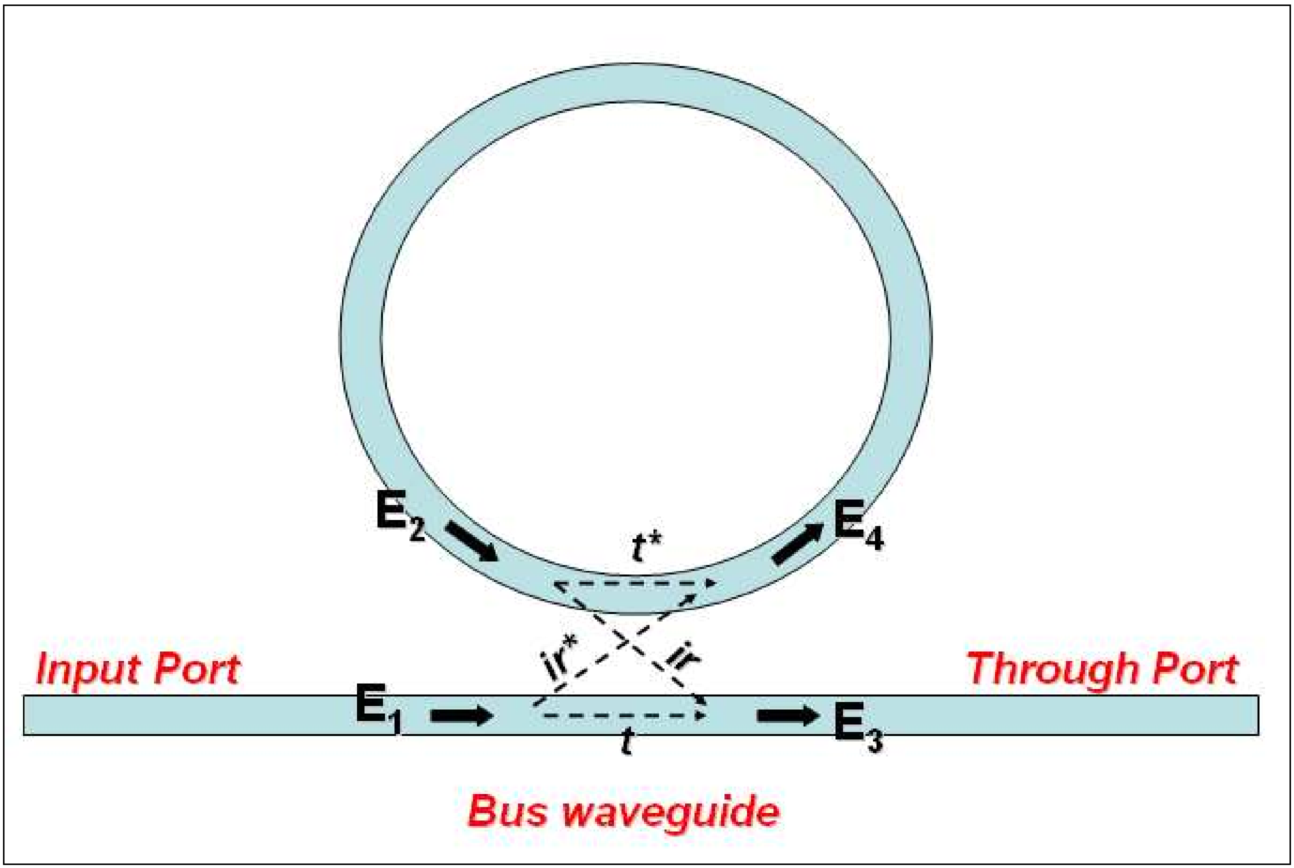

Fig. 4.10. Design of a straight waveguide coupled to a ring resonator

We assume that all waveguides are monomodal and all modes are of the same polarization. The bent-straight waveguide coupler considered is adiabatic, and backreflections are negligible inside this coupler. There is no interaction between the fields of the bus waveguide and the resonator out off the coupling region. We assume that the resonator is symmetric with respect to the x and z axes.

In this case, the model consists of one straight waveguide coupler connected to a segment of the ring waveguide. The variable $E_{1,}$ E_3 (external connections) and E_2, E_4 (ring connections) denote the amplitudes of properly normalized guided modes in the respective coupler port planes (Fig. 4.10). The response of the coupler is characterized by a scattering matrix S. The relationship between coupler input and output amplitudes is given by

$$\begin{pmatrix} E_3 \\ E_4 \end{pmatrix} = S * \begin{pmatrix} E_1 \\ E_2 \end{pmatrix} \text{ with } S = \begin{pmatrix} S_{11} & S_{12} \\ S_{21} & S_{22} \end{pmatrix} = \begin{pmatrix} t & ir \\ ir^* & t^* \end{pmatrix} \qquad (4.3)$$

$S_{i,j}$ represent the coupling from the mode of waveguide j to the mode of waveguide i. They are called cross coupling coefficients. S_{11} or S_{22} are self coupling coefficients. We call t the electric field transmission coefficient and r the electric field reflection coefficient.

Then, if we suppose that t and r are reals:

$$\begin{aligned} E_3 &= tE_1 + irE_2 \\ E_4 &= irE_1 + tE_2 \end{aligned} \tag{4.4}$$

Assuming that the coupling is lossless, t and r are related by

$$|t|^2 + |r|^2 = 1 \tag{4.5}$$

Note that E_2 and E_4 are related by

$$E_2 = e^{-\alpha 2\pi R} e^{i2\pi\beta R} E_4 = a * e^{i2\pi\beta R} E_4 \tag{4.6}$$

Where R is the radius of the ring and β is the mode propagation constant in the ring given by

$$\beta = \frac{2\pi n_{eff}}{\lambda} \tag{4.7}$$

n_{eff} is the effective index for the ring mode and a is the electric field transmission for one round trip in the ring, defined by

$$a = e^{-\alpha 2\pi R} \tag{4.8}$$

α is the loss coefficient given by:

$$\alpha = \alpha_m + \alpha_b + \alpha_w \tag{4.9}$$

α_m is the absorption loss, α_b the radiation loss due to bending and α_w the scattering loss due to wall roughness. The angle $\phi = 2\pi R\beta$ is the phase delay due to propagation around the ring of distance 2πR with an effective index n_{eff}. Solving the equations for E_3 in terms of E_1, we obtain

$$\frac{E_3}{E_1} = \frac{t - ae^{i\phi}}{1 - ate^{i\phi}} \tag{4.10}$$

We also obtain, with the same method, the power transmission $I_3/I_1=|E_3/E_1|^2$

$$\frac{I_3}{I_1} = \frac{a^2 - 2ta\cos(\phi) + t^2}{1 - 2ta\cos(\phi) + t^2 a^2} \qquad (4.11)$$

At the resonance, $\phi = 2m\pi$ where m is an integer, then

$$\frac{I_3}{I_1} = \frac{(a-t)^2}{(1-ta)^2} \qquad (4.12)$$

Figure 4.11 represents the power transmission spectrum of the waveguide (I_3/I_1) as a function of ϕ.

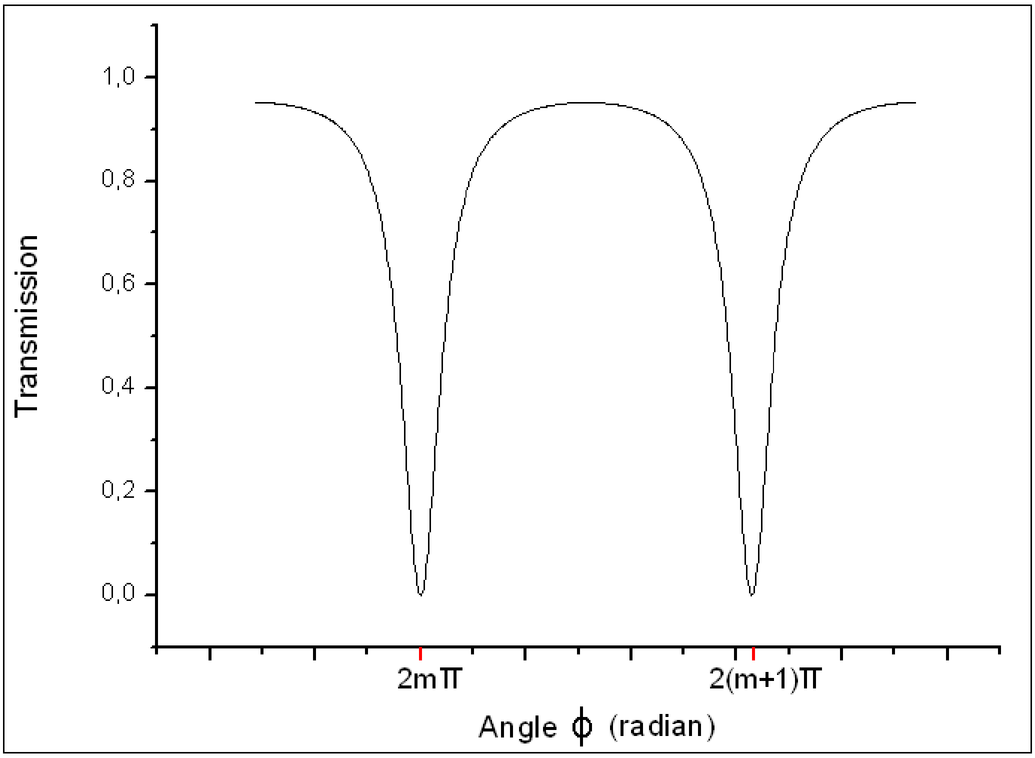

Figure 4.11. Transmission spectrum of a waveguide coupled to a ring resonator for a=t=0,8

Critical coupling occurs when $a = t$. If phase-matching is not achieved in the coupling and r and t are not real, this will shift the resonance to some other value of ϕ but will not otherwise affect the microresonator response. Because of Eq.4.4, it implies a completely destructive interference between the directly transmitted field tE_1 and the internal field coupled into the output waveguide irE_2.

Undercoupling occurs if $a<t$, the transmission spectrum does not vanish at resonance. A smaller amplitude *a* means a larger attenuation loss in the resonator propagation, hence, the spectral dip appears broader than that of critical coupling.

Overcoupling occurs if $a>t$. The transmission spectrum shows a sharper dip when a increases, yet it does not vanish at resonance. Further increase of a increases the transmission at resonance.

At a=1, meaning no attenuation in the resonator at all, *Transparency* occurs. The transmission spectrum becomes unity for all angles ϕ.

When a>1, meaning that *Gain* is introduced into the resonator so the amplitude a is larger than unity, the transmission spectrum is larger than unity and peaks at resonant frequency. Lasing action occurs when $a=1/t$ because I_3/I_1 approaches infinity.

Figure 4.12 represents all these case for a value of t = 0,8.

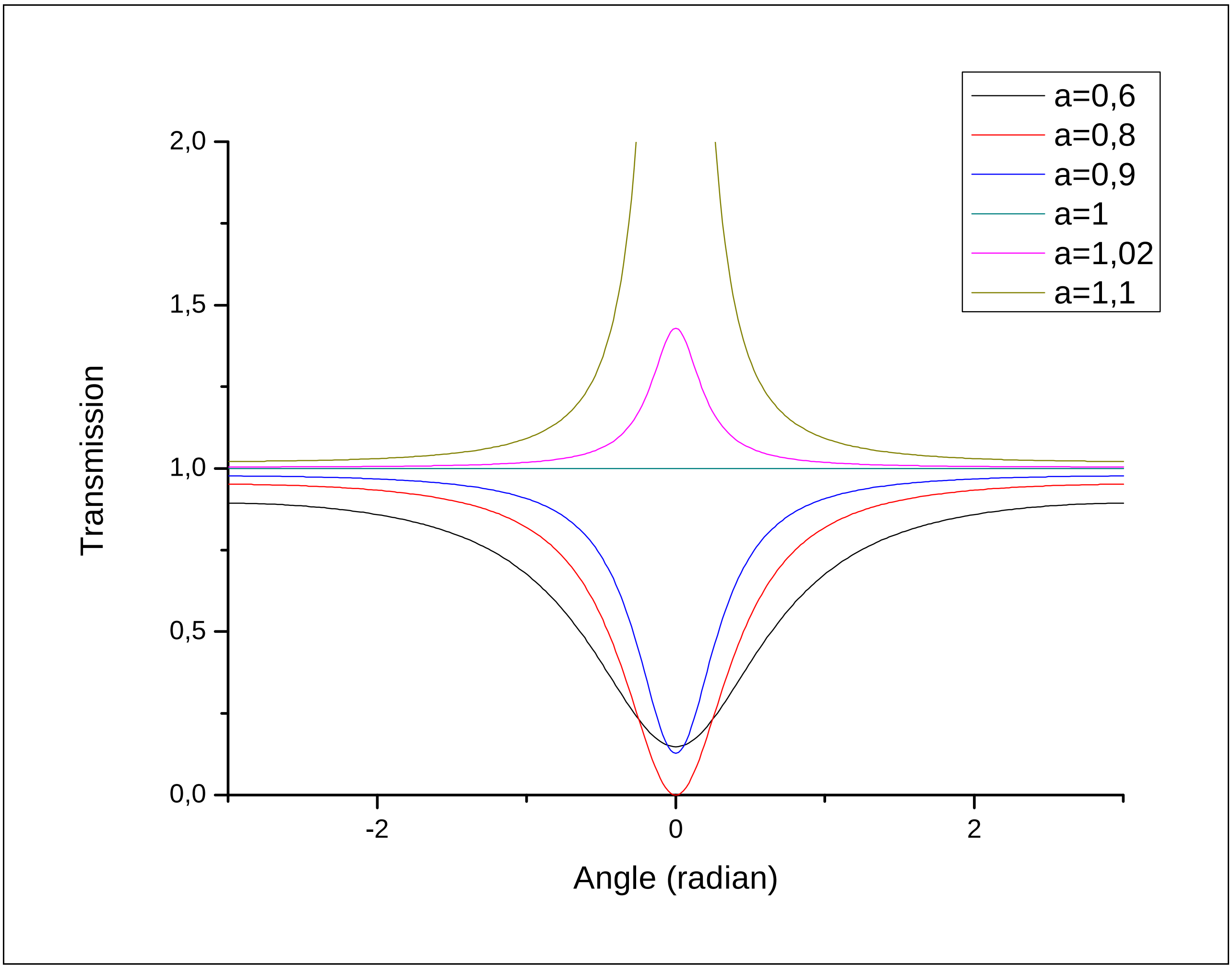

Figure 4.12. Transmission Spectrum near the resonance for various values of a (t=0,8)

4.4.b Free Spectral Range

The free spectral range (FSR) is defined as the wavelength difference Δλ between two successive minima of transmission in the through port. The resonant condition on β is approximated as

$$\beta_{m-1} = \frac{2(m-1)\pi}{2\pi R} = \beta_m - \frac{2\pi}{2\pi R} \approx \beta_m + \left.\frac{\partial\beta}{\partial\lambda}\right|_m \Delta\lambda \qquad (4.13)$$

Where the right hand side is obtained as a first order Taylor series expansion of the propagation constant around the m'th resonance wavelength; Δλ is the difference between the vacuum wavelengths corresponding to the two resonant configurations.

If we write the propagation constant in term of vacuum wavenumber and effective mode index as $\beta = 2\pi n_{eff} / \lambda$ and the wavelength dependence of β or n_{eff} is explicitly incorporated. We can write:

$$\frac{\partial\beta}{\partial\lambda} = -\frac{\beta}{\lambda} + k\frac{\partial n_{eff}}{\partial\lambda} \qquad (4.14)$$

This leads to the expression

$$\frac{\partial\beta}{\partial\lambda} = -\frac{k}{\lambda} n_g \text{ with } n_g = n_{eff} - \lambda\frac{\partial n_{eff}}{\partial\lambda} \qquad (4.15)$$

where n_g is the group index of the cavity mode. Then the free spectral range is given by

$$\Delta\lambda = -\frac{2\pi}{2\pi R}\left(\left.\frac{\partial\beta}{\partial\lambda}\right|_m^{-1}\right) = \frac{\lambda^2}{n_g\, 2\pi R} \qquad (4.16)$$

4.4.c Quality Factor of a ring resonator

The quality factor (Q) is expressed as the ratio of the energy stored in the cavity and the energy lost (or emitted) from the cavity in one period.

The quality factor of a ring is given by the formula:

$$Q_{tot} = \frac{\lambda_0}{\lambda_{FWHM}} \tag{4.17}$$

Where λ_{FWHM} is the full bandwidth at half maximum of the dropped power or transmitted power, and λ_0 is the resonance wavelength. The total quality factor (Q_{tot}) can also be represented, in a first approximation, as:

$$\frac{1}{Q_{tot}} = \frac{1}{Q_r} + \frac{1}{Q_{coupl}} \tag{4.18}$$

where Q_r is the intrinsic quality factor, whereas Q_{coupl} takes into account the losses due to the coupling with the bus waveguide. The latter can be extracted from the extinction ratio at the resonance (T_{min}), as [18]:

$$Q_{coupl} = \frac{2Q_{tot}}{1-\sqrt{T_{\min}}} \tag{4.19}$$

Once Q_r is known, the losses inside the ring α_r can be determined by:

$$\alpha_r = \frac{2\pi n_g}{\lambda Q_r} \tag{4.20}$$

where n_g is the group index.

4.4.d Experimental results

We produced different ring resonators based on the nano-Si horizontal slot waveguides. A resonance of the ring occurs whenever $m\lambda_m = n_{eff}2\pi R$, where n_{eff} is the effective index of the waveguide, λ_m is the resonance wavelength, R is the ring radius and m is an arbitrary integer, also called the longitudinal mode number. It is worth noting that a change of either ring radius or refractive index implies a shift in the resonance wavelength. Testing of these is achieved by coupling a bus nano-Si slot waveguide to the ring (see SEM image in the inset of Fig. 4.13). A preliminary study on horizontal slot waveguides coupled to ring resonators as a function of the ring radius and ring-bus gap has been performed to optimize the bus-resonator coupling for TM polarization. Best results were found for ring-bus gaps of 250 nm independently of the ring radius [9]. Optical transmission spectra trough the bus waveguide were measured in the range 1520−1620 nm by a tunable laser passed through a polarization controller and a tapered fiber.

Fig. 4.13 (inset) shows a transmission spectrum in term of quality factor for both TE and TM polarization of a ring (R=20 μm) coupled to the bus waveguide by a 250 nm wide gap of nano-Si slot waveguide. Since the coupling is optimised for the quasi-TM mode, resonances are observed for TM light and not for TE light. This indicates that no polarization conversion effects occur within the slot waveguide.

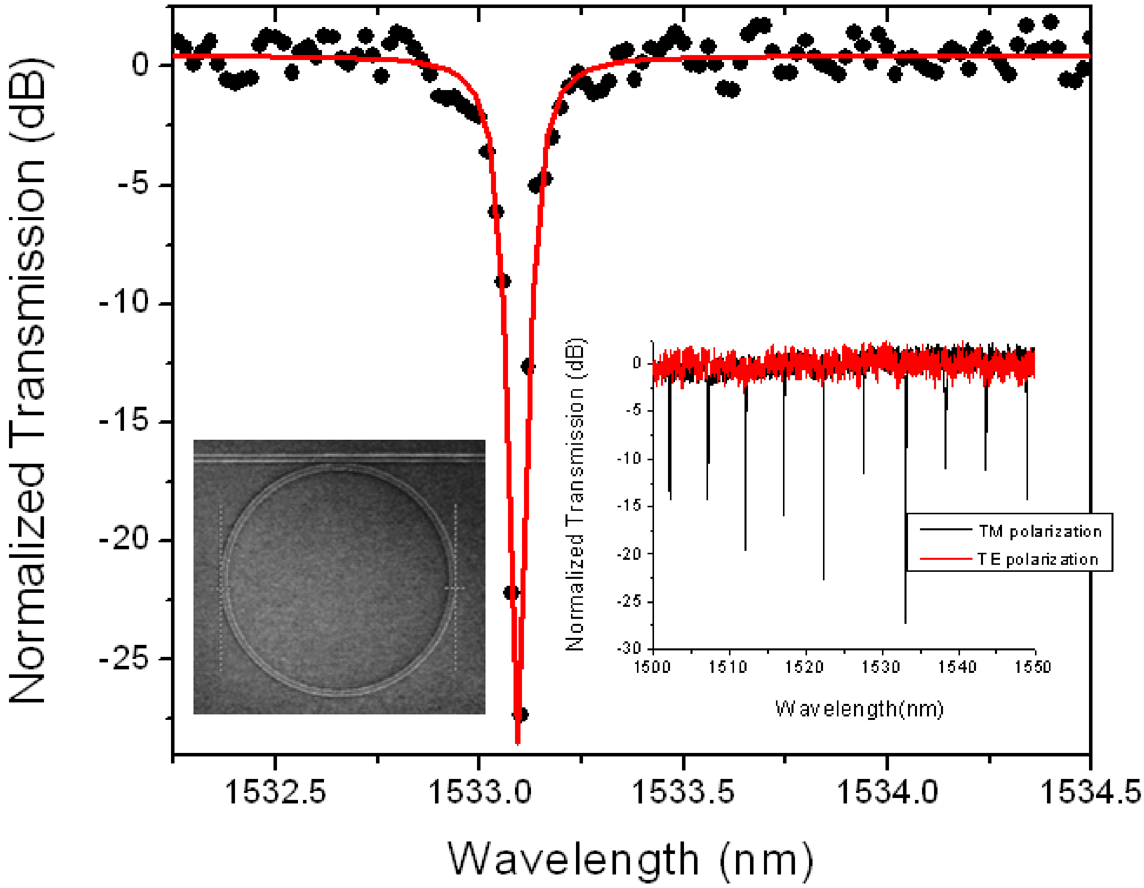

Fig. 4.13. Normalized transmission measurement of a ring resonator with R=20μm and a ring-bus gap of 250nm. A resonance at 1533.8nm is observed with a quality factor Q=12,000. The red line is a lorentzian fit to the dat. (Inset-right) Full spectral interval results for both TE and TM polarization. (Inset-left) SEM image.

Fig. 4.13 shows the detailed spectrum of the resonance at 1533.08 nm. A Lorentzian fit allows the extraction of significant parameters. The resonance extinction ratio is 27 dB. The 3dB bandwidth is λ_{FWHM}=0.13 ± 0.02 nm. This corresponds to a quality factor $Q_{factor} = \lambda/\lambda_{FWHM}$ = 12000 ± 2000 at 1533.08 nm. The best value measured for similar rings is Q_{factor} = 14500 ± 2000. In smaller rings (R=10 μm), Q_{factor} of about 15000 have been found. Free spectral range (*FSR*) of about 11 nm and 5.8 nm have been found for the R=10 and 20 μm rings, respectively. Comparing our results with literature results, we found that Q factors of about 13000 have been reached in similar sized rings (R=10 μm, 150 nm bus gap) [16], while Q factors of about 82000 have been obtained in larger rings (R=100 μm) [17].

In order to compare the losses inside the cavity with the linear propagation losses, we have extracted from the Lorentzian fit parameters the “intrinsic quality factor” of the resonators.

Table 2 reports Q_r and α_r found in samples with and without Si-nc at different input powers. The measured Q factors are similar within the experimental errors bars independently of the Si-nc parameters.

	P_{in} <0.5mW		P_{in} =3mW	
Slot waveguide filled by:	Q_r	α_r (dB/cm)	Q_r	α_r (dB/cm)
SiO_2	15500 ± 3000	41 ± 8	17700 ± 3000	36 ± 8
Si-nc	17000 ± 3000	38 ± 8	18500 ± 3000	35 ± 8

Table 2. Q_r and α_r in coupled rings (R=20μm) with and without Si-nc at different input powers at λ=1533nm.

The values of α_r are much more larger than those found in the correspondent straight waveguides (see Table 1) because they include both linear and bending-induced contributions as well as mode-mismatch losses at the coupling region. Losses inside the rings are similar for both samples. This is in contrast with the linear losses, which differ by about 3-4 dB/cm. It looks like that the processing used to form the rings causes high additional losses which mask the role of the slot region composition in α_r.

In addition, the large error bars in the Q_{factor} measurements causes an indetermination on α_r which is higher than the difference of propagation losses between the waveguides with and without Si-nc.

4.4.e Effect of Si-nc in ring resonators

Nevertheless, Si-nc in the ring resonators are still clearly affecting their properties. Indeed, a shift of the resonance peak position with increasing the light power in the nano-Si and not in the silica ring resonators is observed (Fig. 4.14).

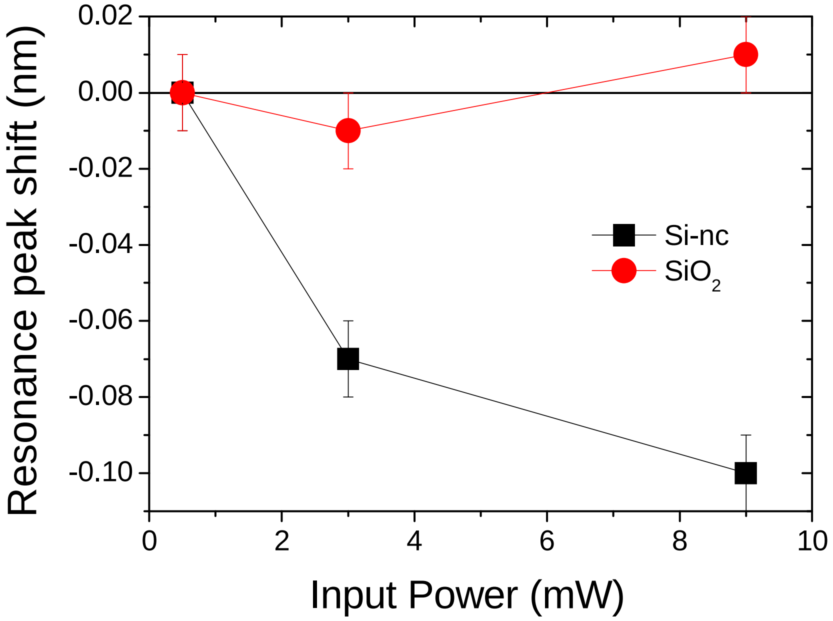

Fig. 4.14. Shift of the resonance peak position as a function of the input power.

As we observe a blue shift of the resonance peak position, the effective index of the propagating mode is decreased ($\Delta n=10^{-4}$) due to free carrier refraction effects in Si-nc. Free Carriers are generated by two photon absorption which is sizeable in Si-nc [13]. Usually, free carriers cause absorption losses in Si-nc waveguides of a few dB/cm [14].

In fact, the refractive–index change (Δn) and the optical absorption coefficient change ($\Delta\alpha$) of Si-nc produced by a change in the concentration of free carriers (ΔN) and at 1,55µm follow the expression [19]:

$$\begin{aligned}\Delta n &= -8{,}8.10^{-22}\,\Delta N - 8{,}5.10^{-18}\,\Delta P^{0{,}8}\\ \Delta\alpha &= 8{,}5.10^{-18}\,\Delta N + 6{,}0.10^{-18}\,\Delta P\end{aligned} \tag{4.21}$$

where ΔP is the density variation of free holes. From $\Delta n/n = \Delta\lambda/\lambda$, we deduce $\Delta n=10^{-4}$, which gives $\Delta N \approx 10^{17}\text{cm}^{-3}$. Consequently, $\Delta\alpha \approx 1\text{cm}^{-1}$, which is not observed in Table 2 because it is within the errors bars.

Non-linear optical effects due to free carriers cannot be the responsible of such a behaviour because the power density in the slot waveguides (about few hundreds of kW/cm^2) will induce a wavelength shift of the order of 10^{-6} µm [13]. In fact, the change in the index of refraction Δn due to nonlinear effects can be approximated by the formula

$$\Delta n = n_2 * I \tag{4.22}$$

where n_2 is the nonlinear refractive index and I is the irradiance (in W.cm^{-2}). From the literature, we found that in case of Si-nc, n_2 can reach values as high as 10^{-12}cm^2.W^{-1}[13]. In our case, the maximum irradiance used was of the order of 10^6 W.cm^{-2} (1mW.μm^{-2}). Using Eq. (4.22), we found that the maximum shift due to nonlinear effects should be of the order of 10^{-6} μm.

4.4.f Group index

From the FSR, it is possible to deduce the group index n_g by Eq. (4.16) for the quasi-TM modes in the wavelength range from 1500 to 1550 nm. In Fig. 4.15, we compare both the values of n_g measured experimentally and the values found by simulations.

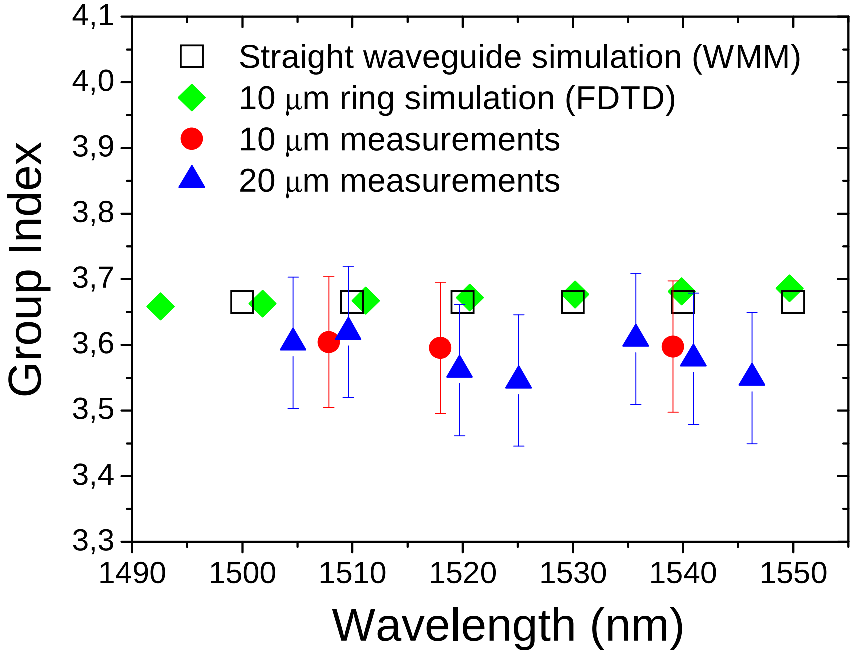

Fig. 4.15. Group index measurements and simulations.[5]

The calculated values, included for comparison, were determined by Eq. (4.15) where the effective indices are calculated from the slot-waveguide parameters with a full-vectorial WMM solver. The simulated values of n_g have been obtained for a straight slot waveguide and a 10 μm radius ring by a FDTD code, where Eq. (4.16) has been used. Very good agreement is found between the experimental values (which are the same within the error bars) and with the simulated ones (less

---

[5] Simulations by Alessandro Pitanti

than 2% difference). This small difference has been found also in Ref. [16]. It can be due either to the uncertainty in the fabricated slot waveguide size and indices or to the fact that the profile of the refraction index in the slot region is supposed to be flat, which might be not the case.

4.5 Double ring resonators

Double ring resonators offer the possibility of realizing a "box-like" filter characteristic which is favorably used in optical networks. Another advantage, also from the point of characterization, is the fact that if two rings are coupled in series, they can have the drop port in the same direction as the input port, which is very convenient for interconnection of many 2 × 2 devices. Serially and parallel coupled ring resonator configurations have been described in detail in the literature [20-21].

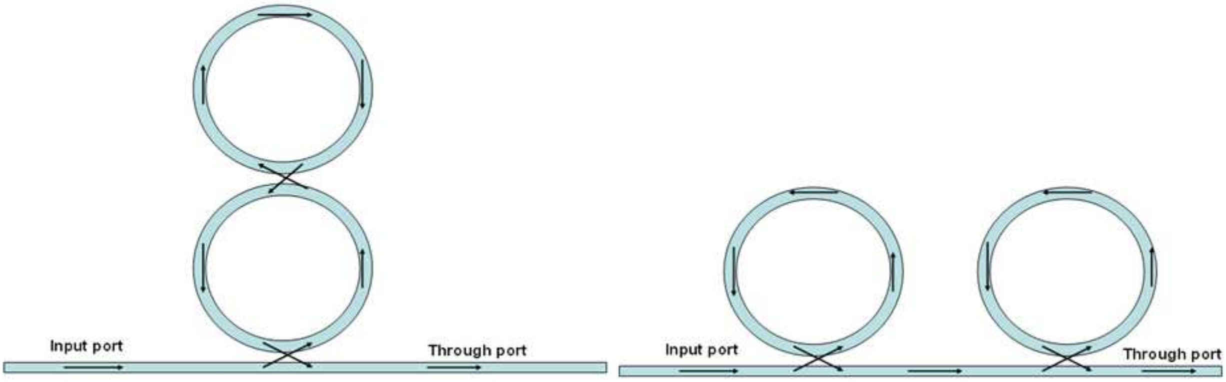

Figure 4.16. Double ring resonators in configuration serially (left) and parallel coupled (right)

There are two different configurations to coupled two rings together (Fig. 4.16). In the serially coupled configuration, each ring resonator is coupled to one another, and a signal that is to be dropped from the input port to the drop port must pass sequentially through each resonator. Because of this sequential power transfer, all resonators must be precisely resonant at a common wavelength. The resulting resonant line shape in the series configuration is determined physically by the separations between the ring resonators. In our case, we will use this configuration.

In the parallel-coupled configuration, all resonators are coupled to the input port waveguide, but usually not directly to one another (the resonators can also be coupled to one another resulting in a wavelength selective reflector, which will be described in the next chapter). The resonators are instead indirectly coupled to each other by the optical path lengths along the input and output waveguides that interconnect them. These lengths determine the details of the resonant line shapes. An optical signal in the parallel configuration passes through all ring resonators simultaneously.

This softens the requirement that the resonances of each rings have to be precisely identical. Nonaligned resonant frequencies instead lead to multiple peaks, or ripple in the lineshape.

4.5.a Experimental results

Double coupled rings have been realized to increase the field enhancement of the optical cavity. This would allow the build-up of the intensity inside the optical resonator, thus improving the optical fluences at values sufficient to give rise to optical non-linear effects. In Fig. 4.17, the resonances of single and double ring resonators are compared. The splitting of the resonances demonstrates the good coupling between the two-rings. In fact, the whispering gallery modes in coupled microresonators are split symmetrically when the individual resonators have the same optical path length (OPL). It's due to the fact that the light must pass through a coupler twice, acquiring a net π phase shift before interfering with the light in the first resonator. When the OPL's of the two rings is the same, such that $\Phi_1= \Phi_2= \Phi$ (where Φ is the round-trip phase shift) the absorbance presents a minimum at the single-ring resonances ($\Phi_{mod}(2\pi) = 0$), resulting in the peak splitting [22]. This effect will be much more detailed in the next chapter. For these double ring resonators, we found very high Q-factors: around 32000 for R=10 µm, which is larger than the corresponding single ring Q of about 15000.

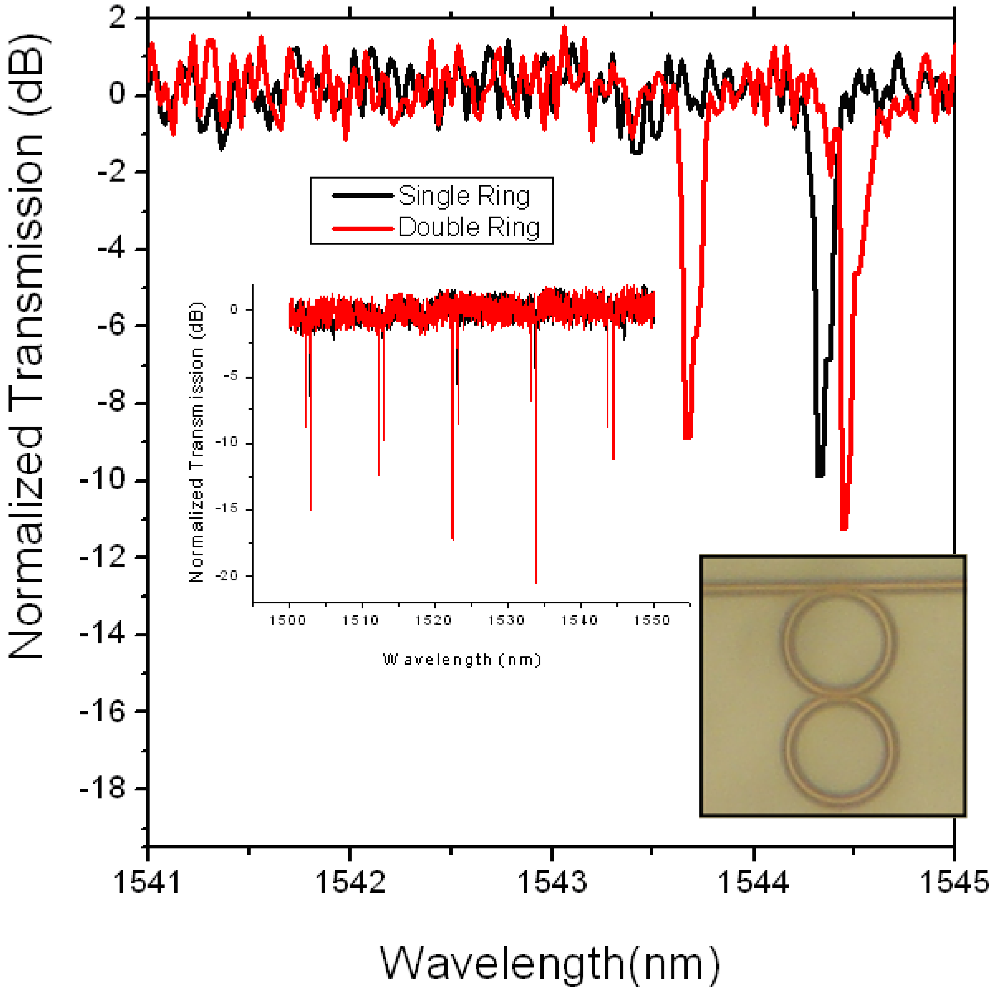

Fig. 4.17. Resonance at 1543.97nm for double (red) and at 1544.3nm for single (black) ring (R=10μm with gaps of 250nm). Inset left: transmission spectra in a large wavelength range (1500-1550nm). Inset right: Optical image of the R=10μm doubled coupled ring resonators.

4.6 Slow light effect in Slot waveguides

The velocity of a pulse of light propagating in any medium is determined by the group index n_g. From this definition, the group velocity $v_g=c/n_g$ where c is the speed of light in the vacuum, is determined not only by the refractive index of the medium but also by the dispersive characteristics of the structure $\omega(dn/d\omega)$, where ω is the optical frequency, in other words the dependence of the refractive index on the optical frequency. This dependence can create significant difference between the group and the phase velocity (c/n) as a function of the properties of the medium where the light propagate.

Although materials can be highly dispersive close to an electronic resonant transition, such transitions are typically accompanied by large absorption. This absorption can be eliminated by an effect called electromagnetically induced transparency (EIT), which will be described in the next chapter, to demonstrate slow light. Unfortunately, it is not simple to implement it in practical system.

Another approach is to realize large structural dispersion by appropriate engineering of the structure in which the light propagates. It is the case of optical periodic structures like coupled resonator optical waveguide (CROW). The CROW is a periodic structure that comprises a chain of resonators in which the light propagates by virtue of the coupling between adjacent resonators. In the case of Fabry-Perot cavities, the slowing of light is achieved by letting it bounces back and forth. Figure 4.18 represents a design of this structure.

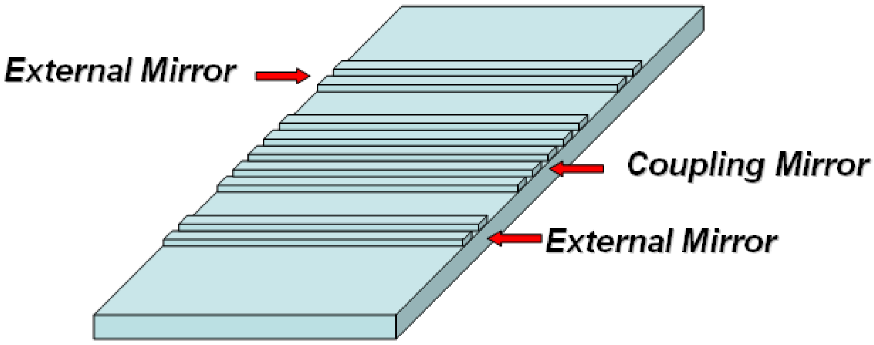

Figure 4.18. Design of Coupled Fabry-Perot Cavities

By combining a “slow structure” like a CROW with the effect of the slot waveguide, which concentrate the field intensity inside the *slot*, it is possible to increase the non-linear effects of the Si-nc increasing the interaction time between the material and the electromagnetic fields propagating inside the waveguide [23]. To exploit this possibility in a low-index guiding waveguide, we have designed a CROW based on slot waveguide structures with Si-nc and working at 1.55 μm[6].

4.6.a Slow light in vertical slot waveguide

Different ways to realize the photonic crystals have been considered, like air slits which cut the whole slot waveguide, air slits interrupted at the slot region, air slits not extending up to the slot region and pattern formed by periodic enlargements of the slot region. The last design (Fig.4.19.a) was finally preferred, due to the fact that this geometry maintains a waveguide structure all along

---

[6] The specific design is due to Alessandro Pitanti and Paolo Bettotti

the periodic modulation and the modulation overlaps with the intensity maximum of the optical mode propagating in the slot region, which produces large photonic gaps. For these reasons, this geometry has been preferred in realizing photonic devices in slot waveguides [24]. A first optimization of these CROW devices shows a group velocity of more than c/10 at 1.55 µm by simulation.

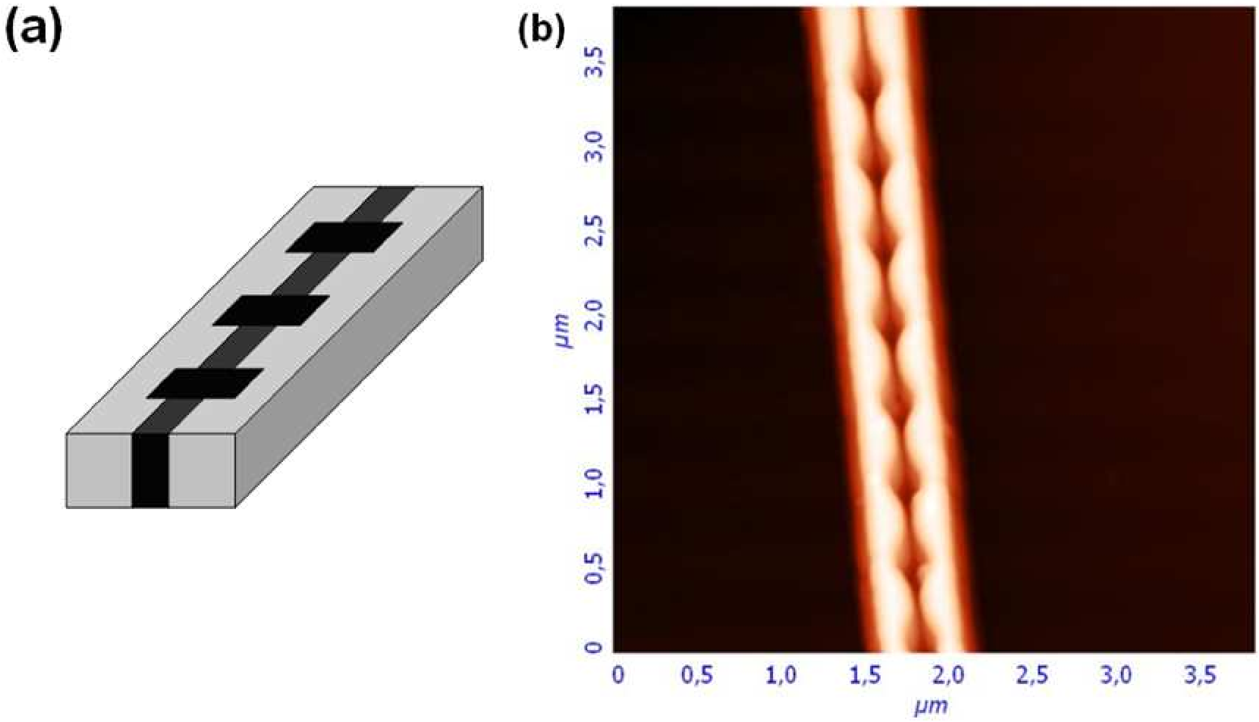

Fig. 4.19. Schema of a cavity create by periodic enlargements in the slot region (a) and AFM image of the cavity

Unfortunately, we didn't measure any significant results. This can be explained by two reasons. First of all, this geometry is very difficult to produce. Fig. 4.19.b represents an AFM image of a slot waveguide with 1D photonic cavity not covered by Silica. As shown by the image, the periodic enlargements are not well defined, due to their very small size and the resolution used to define the sample. But the main reason is the losses of the vertical slot waveguides. As explained in chapter 4.3.a, the losses measured for the vertical slot waveguides were very high (around 30dB/cm), and the creation of a cavity inside the slot creates additional losses to the waveguide. In order to reduce processing difficulties encountered above, another "slow cavity" was envisaged for horizontal slot waveguides.

4.6.b Slow light in horizontal slot waveguides

We created a slot 1D photonic crystal inside our horizontal slot waveguide with a photonic band gap (for wavevectors along the guide propagation direction) around 1.55 µm. To design a “Fabry Perot cavity”-like inside our horizontal slot waveguide, we inserted periodic trenches along the entire section of the waveguide, which as the same behaviour as a Bragg mirror (Fig. 4.20). From this design, a 5-coupled-cavities device has been fabricated and optically characterized. From a point of view of the fabrication, this design is easily reproducible, even if the trenches create high losses inside the waveguide. The shape of the mirror was defined by two geometric parameters, the trench width and the period of the structure. The final device consists in 5 coupled cavities each one separated by a 16-period mirror. On Fig. 4.20, we represent the final design only with two coupled cavities. To get a good matching with the input waveguide, the first and the last mirrors were of 8-periods, as well as an adiabatic tapering of the first and last periods of each mirror was used. All the measurements have been performed in quasi-TM polarization as on the other hand, quasi-TE polarized light showed no sign of any photonic features.

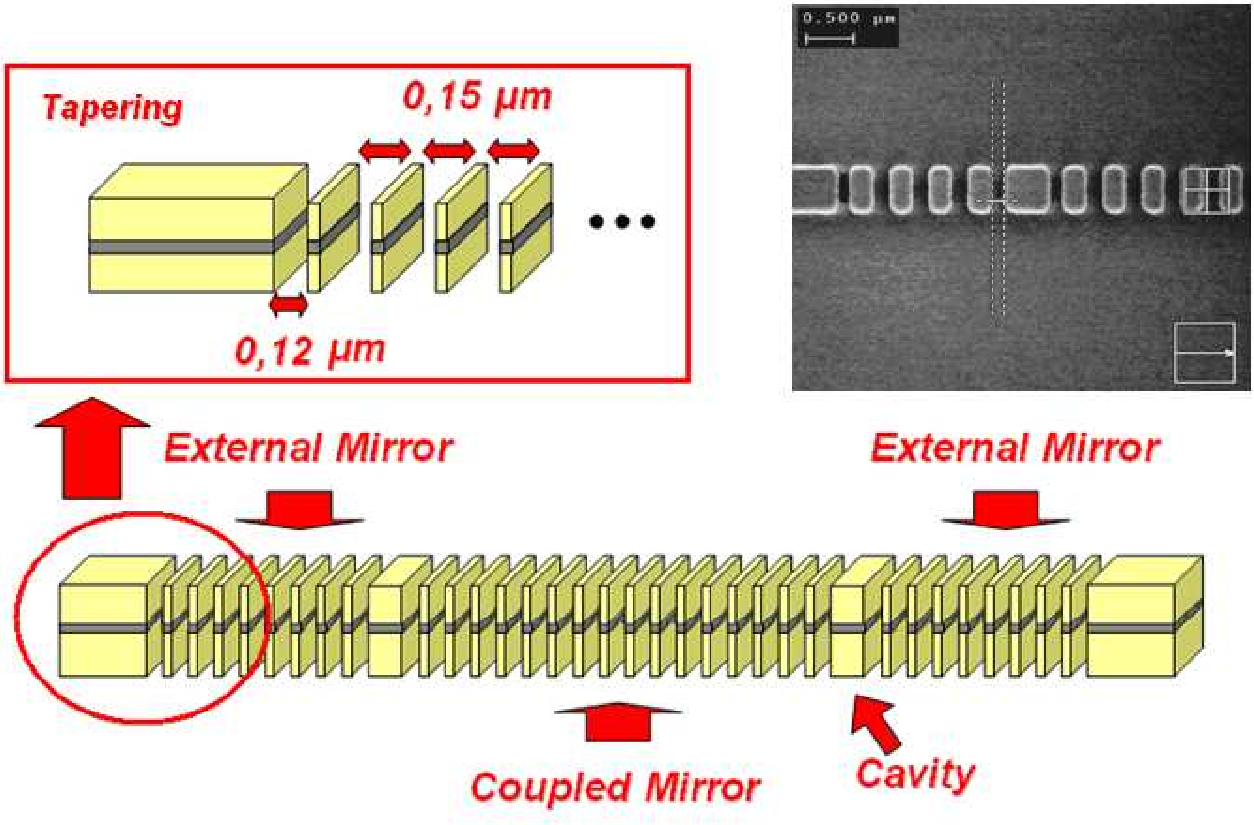

Fig. 4.20. Design of the coupled cavities based horizontal slot waveguide with a zoom on the adiabatic tapering; (Inset right) SEM image of the photonic structure before SiO$_2$ deposition

The transmission measured is showed in Fig 4.21. Note that the transmission spectra have been normalized with the straight slot waveguide and the wavelengths normalized to the central wavelength of the gap (λ_0=1.45 µm).

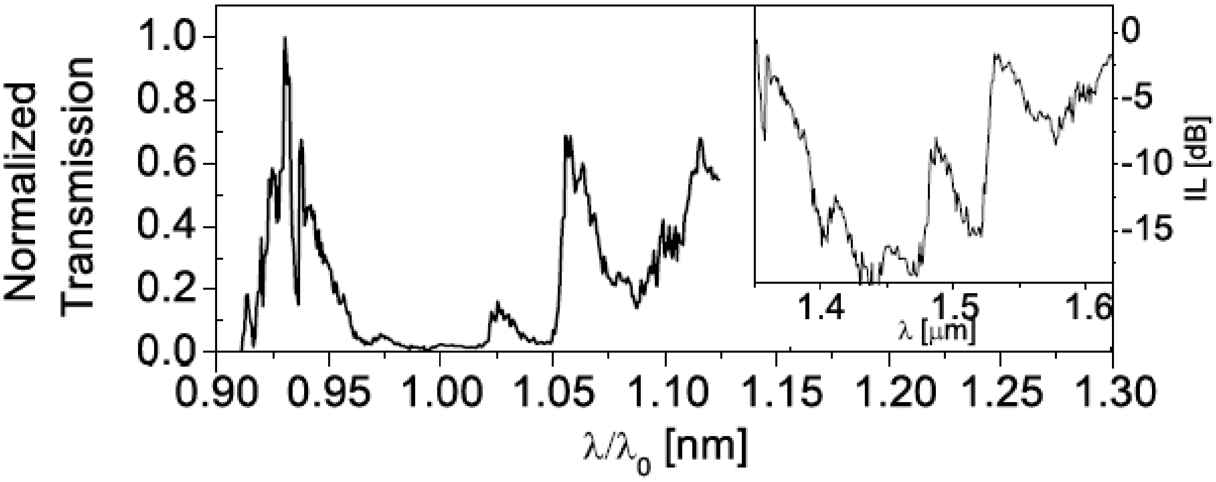

Fig. 4.21. Transmission spectrum normalized in function of the central wavelength of a 5 coupled-cavities device; (Inset right) Broad transmission spectrum in dB scale

A shift of about 100nm is present between the simulated [25] and experimental data, due to a disagreement between the nominal and real photonic structure. Nevertheless, the spectral features of the photonic gap are quite similar. The peak at 1.05 λ/λ_0 is the edge of the bang gap, also found in the simulation of a simple Bragg mirror[7] (Fig. 4.22). The cavity peak is found at λ/λ_0=1.02. Unfortunately, the coupling between the cavities is not strong enough to resolve the five different cavity peaks. We can just observe a single and broadened peak. Another very interesting result is the important extinction ratio measured experimentally in the band gap, which is more than 15 dB.

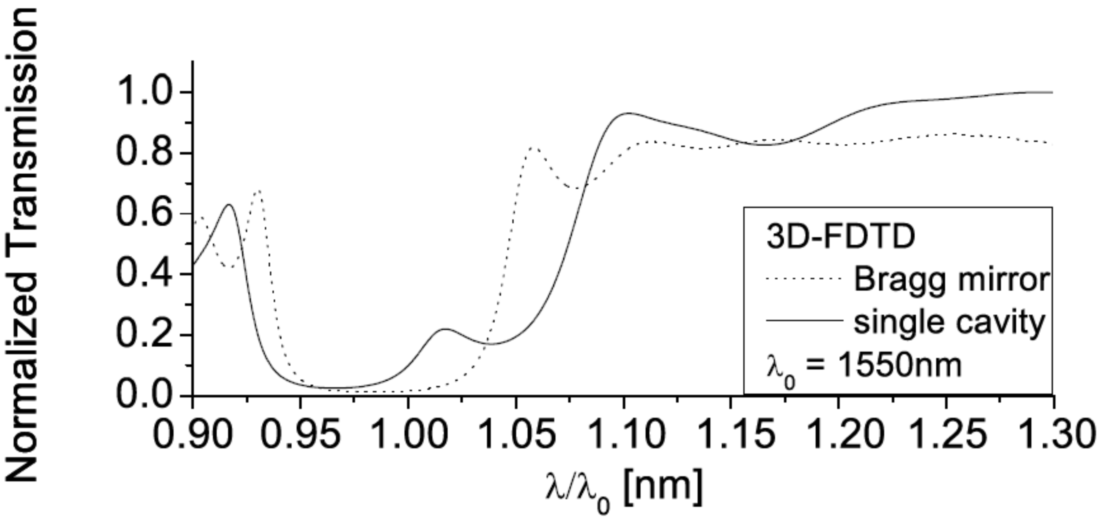

Fig. 4.22. 3D FDTD simulation of the device with one single cavity and a Bragg Mirror

---

[7] Simulations were made by Alessandro Pitanti

4.7 Conclusion

We have demonstrated low losses nano-Si slot waveguides and high-quality factor coupled ring resonators. The importance of this works relies on the fact that by optimizing the annealed SRSO (i.e. Si-nc) in the slot, we have significantly reduced the propagation losses and at the same time we can add new functionalities related to the Si-nc optical properties (i.e. light emission and/or non-linear optical effects). A one-dimensional photonic crystal structure based on horizontal slot waveguide with a photonic band gap around 1.55 μm has also been designed and optically characterized. The high-quality factors demonstrated in single and double ring resonators, if associated to the sizeable non-linear effect of nano-Si in the slot, can enable all optical switches and tunable telecommunications filters.

References

[1]. Proceeding of the IEEE special issue "*Silicon Photonics*," Vol. **97**, No. 7 (July 2009).

[2]. Y. Vlasov and S. McNab, *Opt. Express* **12**, 1622–1631 (2004).

[3]. K. Yamada, T. Tsuchizawa, T. Watanabe, J. Takahashi, E. Tamechika, M. Takahashi, S. Uchiyama, H. Fukuda, T. Shoji, S. Itabashi, and H. Morita, *IEICE Trans. Electron.* **E87–C**, 351–357 (2004).

[4]. S. McNab, N. Moll, and Y. Vlasov, *Opt. Express* **11**, 2927–2939 (2003).

[5]. V. Almeida, Q. Xu, C. Barrios, and M. Lipson, *Opt. Lett*. **29**, 1209–1211 (2004).

[6]. C.A. Barrios, *Electron. Lett.* **40**, 862-863 (2004).

[7]. C.A. Barrios, B. Sànchez, K. B. Gylfason, A. Griol, H. Sohlström, M. Holgado, and R. Casquet, *Opt. Express* **15**, 6846-6857 (2007).

[8]. P. Sanchis, J. Blasco, A. Martinez and J. Martì, *J. Lightw. Technol.* **25**, 1290-1305 (2007).

[9]. Y. Lebour, R. Guider, E. Jordana, J.-M. Fedeli, P. Pellegrino, S. Hernandez, B. Garrido, N. Daldosso, and L. Pavesi, *Proc. of 5th IEEE Int. Conf. on Group IV Photonics*, 215-217 (2008).

[10]. E. Jordana, J.-M. Fedeli, P. Lyan, J.P. Colonna, P. Gautier, N. Daldosso, L. Pavesi, Y. Lebour, P. Pellegrino, B. Garrido, J. Blasco, F. Cuesta-Soto, and P. Sanchis, *Proc. of 4th IEEE Int. Conf. on Group IV Photonics*, 217-219 (2007).

[11]. S. Hernandez, P. Pellegrino, A. Martinez, Y. Lebour, B. Garrido, R. Spano, M. Cazzanelli, N. Daldosso, L. Pavesi, E. Jordana and J.M. Fedeli, *J. Appl. Phys.* **103**, 064309 (2008).

[12]. J. T. Robinson, K. Preston, O. Painter, and M. Lipson, *Opt. Express* **16**, 16659-16669 (2008).

[13]. R. Spano, N. Daldosso, M. Cazzanelli, L. Ferraioli, L. Tartara, J. Yu, V. Degiorgio, E. Jordana, J.M. Fedeli, L. Pavesi, *Optics Express* **17**, 3941-3950 (2009).

[14]. D. Navarro-Urrios, A. Pitanti, N. Daldosso, F. Gorbilleau, R. Rizk, G. Pucker, L. Pavesi, *Appl. Phys. Lett.* **92**, 051101 (2008).

[15]. N. Daldosso and L. Pavesi, *Laser & Phot. Rev.* **3**, 508–534 (2009).

[16]. R. Sun, P. Dong, N. N. Feng, C. Y. Hong, J. Michel, M. Lipson, and L. Kimerling, *Opt. Express* **15**, 17967-17972 (2007).

[17]. K. Preston and M. Lipson, *Opt. Express* **17**, 1527-1534 (2009).

[18]. M. Borselli, T. J. Johnson, and O. Painter, *Opt. Express* **13**, 1515-1528 (2005).

[19]. R. A. Soref and B. R. Bennett, *IEEE J. Quantum Electron.* **QE-23**, 123-129 (1987).

[20]. B. E. Little, S. T. Chu, H. A. Haus, J. Foresi, and J.-P. Laine, *J. Lightwave Technol.* **15**, 998–1005 (1997).

[21]. A. Melloni, *Opt. Lett.* **26**, 917-919 (2001).

[22]. D.D. Smith, H. Chang, K. A. Fuller, A. T. Rosenberger, and R. W. Boyd, *Phys. Rev. A* **69**, 063804 (2004).

[23]. M. Soljacic, S. G. Johnson, S. Fan, M. Ibanescu, E. Ippen, J. D. Joannopoulos, J. *Opt. Soc. Am. B* **19**, 2052-2059 (2002)

[24]. F. Riboli, P. Bettotti and L. Pavesi, *Opt. Express* **15**, 11769 (2007)

[25]. A. Pitanti, P. Bettotti, E. Rigo, R. Guider, N. Daldosso, J.M. Fedeli and L. Pavesi, *Group IV Photonics, 5th IEEE International Conference*, 17-19 Sept. 2008.

Chapter five

Silicon on Insulator coupled-resonators measurements

As we explain in the last chapter, microresonators are expected to play a key role in the large-scale integration of photonic devices as a consequence of their compact geometry and tailorable dispersive and nonlinear optical properties. In this chapter, we will measure and compare the characteristic of different sequences of microring (or whispering-gallery microdisk) resonators.

On a first time, we will study the serially coupled configuration, where each ring resonator is coupled to another one. For this structure, we restrict our attention to two ring/disk based units. This configuration is called CROW. The second configuration that we will study is the SCISSOR (Side-Coupled Integrated Spaced Sequence of Resonators) configuration. In this case, all resonators are coupled through the input and drop port waveguides. Recent theoretical analysis of coupled microresonators has revealed that coherent effects in coupled resonator systems are remarkably similar to those in atoms [1–3], where electromagnetically induced transparency (EIT) occurs due to quantum interference effects induced by coherently driving the atom with an external laser [4-6]. Induced transparency can also occur in a photonic resonator system where coherent interference between coupled resonators is instead enforced by the geometry of the nanophotonic structure.

5.1 Serially coupled ring resonator theory

The first configuration that will be discussed is the basic ring resonator add–drop configuration, consisting of one input, one output waveguide and the ring resonator (Fig. 5.1). The four ports of the ring resonator are referred to in the following as input port, through port, drop port and add port.

5.1.a Add-Drop configuration

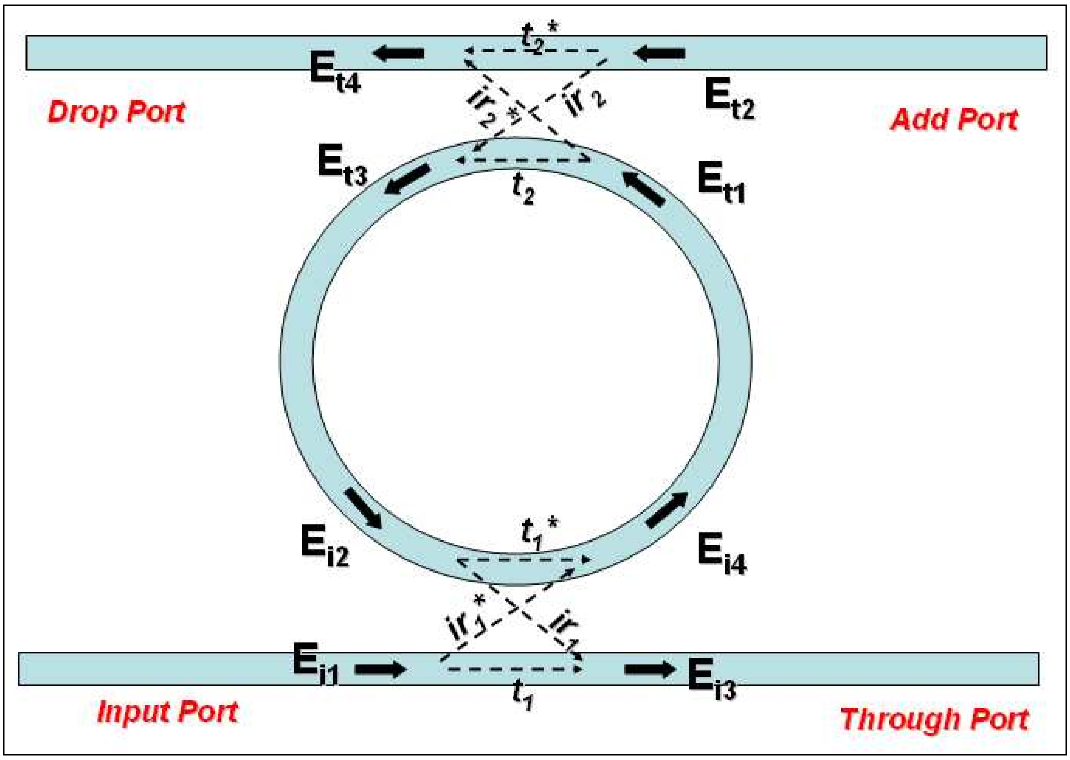

Fig. 5.1. Add-Drop ring resonator filter

Using the same model as the last chapter, we found that

$$\begin{pmatrix} E_{i3} \\ E_{i4} \end{pmatrix} = \begin{pmatrix} t_1 & ir_1 \\ ir_1^* & t_1^* \end{pmatrix} * \begin{pmatrix} E_{i1} \\ E_{i2} \end{pmatrix} \text{ and } \begin{pmatrix} E_{t3} \\ E_{t4} \end{pmatrix} = \begin{pmatrix} t_2 & ir_2 \\ ir_2^* & t_2^* \end{pmatrix} * \begin{pmatrix} E_{t1} \\ E_{t2} \end{pmatrix} \tag{5.1}$$

$$E_{t1} = e^{-\alpha\pi R} e^{i\pi\beta R} E_{i4} = a_{1/2} * e^{i\pi\beta R} E_{i4} \tag{5.2}$$

$$E_{i2} = e^{-\alpha\pi R} e^{i\pi\beta R} E_{t3} = a_{1/2} * e^{i\pi\beta R} E_{t3} \tag{5.3}$$

Where $a_{1/2} \equiv \sqrt{a}$, r_1 and t_1 are the E field reflections and transmission coefficients for the input coupling, and r_2 and t_2 are the E field and transmission coefficient for the output coupling, respectively.

Due to the linearity and the symmetry of the device, it is sufficient to consider an excitation in only one of the external ports, in our case E_{i1}. If we suppose that r_1 r_2 and t_1 t_2 are real, we can rewrite eq. 5.1 as

$$\begin{pmatrix} E_{i4} \\ E_{i2} \end{pmatrix} = \frac{1}{ir_1} \begin{pmatrix} -1 & t_1 \\ -t_1 & 1 \end{pmatrix} * \begin{pmatrix} E_{i1} \\ E_{i3} \end{pmatrix} \text{ and } \begin{pmatrix} E_{t4} \\ E_{t2} \end{pmatrix} = \frac{1}{ir_2} \begin{pmatrix} -1 & t_2 \\ -t_2 & 1 \end{pmatrix} * \begin{pmatrix} E_{t1} \\ E_{t3} \end{pmatrix} \tag{5.4}$$

We can also rewrite Eq. 5.2 and 5.3 as a matrix product, like

$$\begin{pmatrix} E_{t1} \\ E_{t3} \end{pmatrix} = \begin{pmatrix} a_{1/2}e^{i\frac{\phi}{2}} & 0 \\ 0 & \dfrac{1}{a_{1/2}}e^{-i\frac{\phi}{2}} \end{pmatrix} * \begin{pmatrix} E_{i4} \\ E_{i2} \end{pmatrix} \tag{5.5}$$

where $\phi = 2\pi R\beta$. So, by combining (5.4) and (5.5), we obtain

$$\begin{pmatrix} E_{t1} \\ E_{t3} \end{pmatrix} = \begin{pmatrix} -\dfrac{a_{1/2}}{ir_1}e^{i\frac{\phi}{2}} & \dfrac{t_1 a_{1/2}}{ir_1}e^{i\frac{\phi}{2}} \\ -\dfrac{t_1}{ir_1 a_{1/2}}e^{-i\frac{\phi}{2}} & \dfrac{1}{ir_1 a_{1/2}}e^{-i\frac{\phi}{2}} \end{pmatrix} * \begin{pmatrix} E_{i1} \\ E_{i3} \end{pmatrix} \tag{5.6}$$

And by multiplying (5.6) by (5.4), we obtain the relation between E_{t4}, E_{t2} and E_{i1}, E_{i3}.

$$\begin{pmatrix} E_{t4} \\ E_{t2} \end{pmatrix} = \begin{pmatrix} \dfrac{t_1 t_2 e^{-i\frac{\phi}{2}} - ae^{i\frac{\phi}{2}}}{r_1 r_2 a_{1/2}} & \dfrac{t_1 ae^{i\frac{\phi}{2}} - t_2 e^{-i\frac{\phi}{2}}}{r_1 r_2 a_{1/2}} \\ \dfrac{-t_2 ae^{i\frac{\phi}{2}} + t_1 e^{-i\frac{\phi}{2}}}{r_1 r_2 a_{1/2}} & \dfrac{t_1 t_2 ae^{i\frac{\phi}{2}} - e^{-i\frac{\phi}{2}}}{r_1 r_2 a_{1/2}} \end{pmatrix} * \begin{pmatrix} E_{i1} \\ E_{i3} \end{pmatrix} \tag{5.7}$$

As there is no input from E_{t2}, we can write $E_{t2}=0$. Then the through mode amplitude E_{i3}/E_{i1} is

$$\frac{E_{i3}}{E_{i1}} = \frac{t_2 ae^{i\frac{\phi}{2}} - t_1 e^{-i\frac{\phi}{2}}}{t_1 t_2 ae^{i\frac{\phi}{2}} - e^{-i\frac{\phi}{2}}} = \frac{t_2 ae^{i\phi} - t_1}{t_1 t_2 ae^{i\phi} - 1} \tag{5.8}$$

And by combining (5.7) and (5.8), we obtain for the drop port mode amplitude E_{t4}/E_{i1}

$$\frac{E_{t4}}{E_{i1}} = \frac{ae^{i\frac{\phi}{2}}\left(1 - t_1^2 - t_2^2 + t_1^2 t_2^2\right)}{r_1 r_2 a_{1/2}\left(t_1 t_2 ae^{i\phi} - 1\right)} \tag{5.9}$$

Since $t_1^2+r_1^2=1$, $t_2^2+r_2^2=1$ and $a^2_{1/2}\equiv a$,

$$\frac{E_{t4}}{E_{i1}} = \frac{r_1 r_2 a_{1/2} e^{i\frac{\phi}{2}}}{t_1 t_2 a e^{i\phi} - 1} \tag{5.10}$$

The power transmission in the through $I_{i3}/I_{i1}=|E_{i3}/E_{i1}|^2$ and in the drop $I_{t4}/I_{i1}=|E_{t4}/E_{i1}|^2$ will be

$$\frac{I_{i3}}{I_{i1}} = \frac{{t_2}^2 a^2 - 2t_1 t_2 a\cos(\phi) + {t_1}^2}{{t_1}^2 {t_2}^2 a^2 - 2at_1 t_2 \cos(\phi) + 1} \quad \text{and} \quad \frac{I_{t4}}{I_{i1}} = \frac{{r_1}^2 {r_2}^2 a}{t_1^2 t_2^2 a^2 - 2t_1 t_2 a\cos(\phi) + 1} \tag{5.11}$$

At the resonance, $\phi = 2m\pi$ where m is an integer, the drop-put becomes

$$\frac{I_{t4}}{I_{i1}} = \frac{\left(1 - {t_1}^2\right)\left(1 - {t_2}^2\right)a}{\left(1 - t_1 t_2 a\right)^2} \tag{5.12}$$

The through port mode signal I_{i3}/I_{i1} (5.11) will be zero at resonance for identical symmetrical couplers $t_1 = t_2$ if $a = 1$, which indicates that the wavelength on resonance is fully extracted by the resonator. The value of $a = 1$ can only be achieved by the implementation of gain incorporated in the ring resonator to compensate the waveguide losses. The value of the loss coefficient α is fixed in a purely passive ring resonator. A possibility of achieving minimum intensity ($I_{i3}/I_{i1} = 0$) at resonance of the output transmission at the throughput port is to adjust the coupling parameters t_1, t_2 to the loss coefficient α. From 5.11, we obtain $a=t_1/t_2$. If the ring resonator is lossless ($a = 1$), then the couplers have to be symmetric in order to achieve minimum intensity. An example of spectrum for an Add-Drop structure is shown in Fig. 5.2.

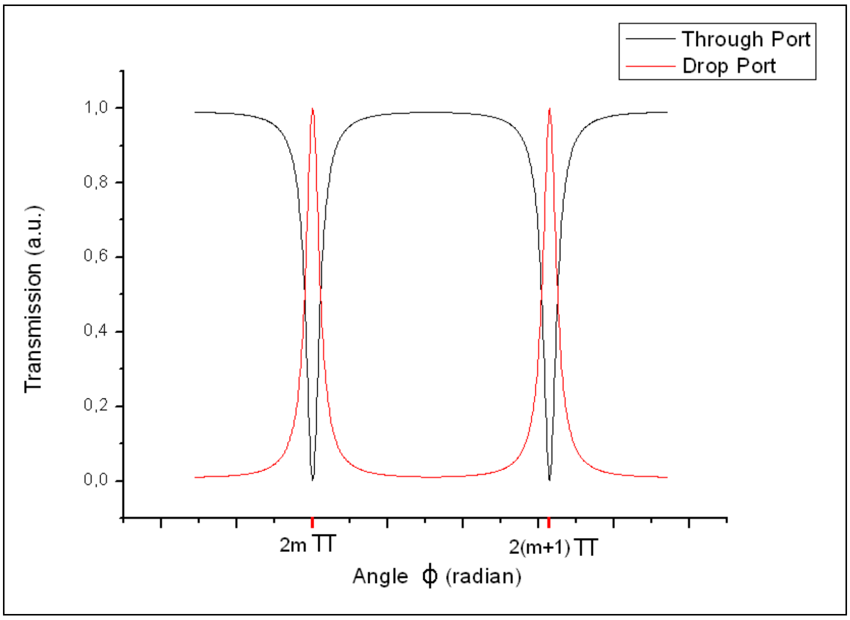

Figure 5.2. Spectrum of an Add-Drop ring resonator structure for $t_1=t_2=0{,}9$ and $a=1$

5.1.b Serially double coupled-ring

After having describe the principle of an add drop filter, the analysis of a coupled ring resonator using both drop and through ports is very similar. A schema of a serially coupled double ring resonator is shown in Fig. 5.3. Using the same procedure as in the last section, the fields depicted in Fig. 5.3 can be easily calculated. Note that we change the names of the outputs for an easier comprehension.

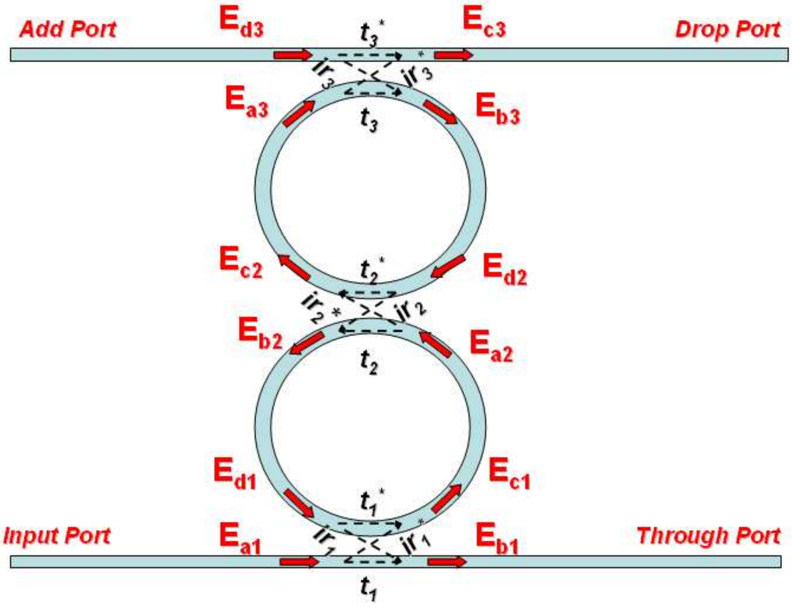

Fig. 5.3. Schema of an Add-Drop double-ring resonator filter

In the last paragraph, we found the relations between the output E_{a1} E_{b1} and E_{a2} E_{b2}. We can write exactly the same relations between E_{a2} E_{b2} and E_{a3} E_{b3}.

$$\begin{pmatrix} E_{a2} \\ E_{b2} \end{pmatrix} = \begin{pmatrix} -\frac{a_{1/2}}{ir_1} e^{i\frac{\phi}{2}} & \frac{t_1 a_{1/2}}{ir_1} e^{i\frac{\phi}{2}} \\ -\frac{t_1}{ir_1 a_{1/2}} e^{-i\frac{\phi}{2}} & \frac{1}{ir_1 a_{1/2}} e^{-i\frac{\phi}{2}} \end{pmatrix} * \begin{pmatrix} E_{a1} \\ E_{b1} \end{pmatrix} \qquad (5.13)$$

and

$$\begin{pmatrix} E_{a3} \\ E_{b3} \end{pmatrix} = \begin{pmatrix} -\frac{a_{1/2}}{ir_2} e^{i\frac{\phi}{2}} & \frac{t_2 a_{1/2}}{ir_2} e^{i\frac{\phi}{2}} \\ -\frac{t_2}{ir_2 a_{1/2}} e^{-i\frac{\phi}{2}} & \frac{1}{ir_2 a_{1/2}} e^{-i\frac{\phi}{2}} \end{pmatrix} * \begin{pmatrix} E_{a2} \\ E_{b2} \end{pmatrix} \qquad (5.14)$$

Using also the relation

$$\begin{pmatrix} E_{c3} \\ E_{d3} \end{pmatrix} = \frac{1}{ir_3} \begin{pmatrix} -1 & t_3 \\ -t_3 & 1 \end{pmatrix} * \begin{pmatrix} E_{a3} \\ E_{b3} \end{pmatrix} \qquad (5.15)$$

And the fact that $E_{d3}=0$, it's easy to find the relation between E_{c3} and E_{a1}. With the same method, we can also analyze a multiple coupled-ring resonator structure.

5.2 Electromagnetically-induced transparency (EIT) and Coupled Resonator Induced Transparency (CRIT)

Electromagnetically-induced transparency (EIT) is a phenomenon that can occur in atomic systems as a result of the destructive interference between excitation pathways to the upper level. This interference occurs in single atoms but manifests itself at the macroscopic level. Naturally, one is led to ask whether EIT-like effects can occur in a classical system. In fact, EIT-like effects can be established in coupled optical resonators due to classical destructive interference. *Yariv et al.* have shown that extensive mode splitting occurs in coupled-resonator optical waveguides (CROW's), leading to the formation of photonic bands [7]. In addition, we have found that whispering gallery modes (WGM's) in coupled microresonators are split symmetrically when the individual resonators have the same optical path length (OPL), due to the fact that light must traverse a coupler twice, acquiring a net π phase shift before interfering with light in the initial resonator [8]. But, contrary to the EIT, the splitting in coupled (mechanical, electrical, or, as in the case examined here, optical) resonators is the result of an internal coupling between individual oscillators. For this reason, coupled-resonator-induced transparency (CRIT) does not suffer from the propagation scaling limitations of EIT as a result of control field absorption.

5.2.a. EIT in an atomic configuration

In order to understand better our system, let's study the EIT in an atomic three-level configuration. The quantum states |1> and |2> represent the two ground states of the atom and the state |3> is the excited atomic level.

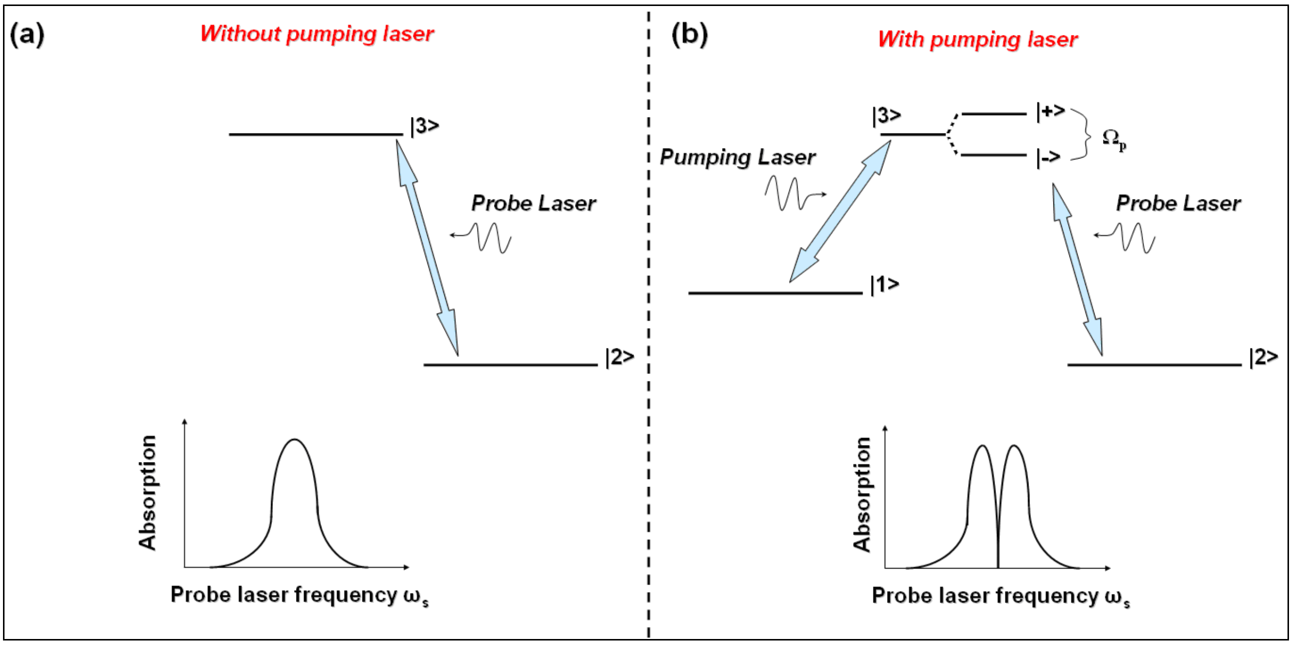

Fig. 5.4. Energy diagram of a three level atoms interacting with two laser fields and Absorption spectra of the probe laser without pumping laser (a) and with pumping laser (b).

Without any pump laser, if we scan the frequency of the probe laser, we measure a standard absorption resonance peak, define by transition from |2> to |3> (Fig. 5.4.a).

When a strong control field is resonantly applied to the |1>-|3> transition, the excited state |3> splits into the dressed states |+> and |->, which are a combination of the states |1> and |3>, separated by the Rabi frequency of the pumping field Ω_p (Fig. 5.4.b). The probe beam will therefore couple the ground state |2> to two other states instead of one. As the splitting varies linearly with the Rabi frequency, when Ω_p increases, the splitting becomes more pronounced. When the splitting is smaller than the excited state width, the two levels are indistinguishable, and we can observe quantum interference in the probe absorption spectrum. The splitting in the absorption spectrum is also called the Autler-Townes doublet.

Simultaneously, this narrow peak in transmission corresponds to a steep variation in the refractive index $n(\omega)$ (and therefore the group velocity for the signal pulse) as a function of signal field frequency. This is why the signal field “slows down” in an EIT medium. Both the width of the EIT resonance and the value of the dispersion ($dn/d\omega$) are proportional to the intensity of the control field, which (at least theoretically) means that EIT can be used to make a lossless and completely controllable optical delay element.

5.2.b. Coupled resonators induced transparency

The analogy between the serially double-coupled ring resonators and the three-level configuration studied above is easy to do. In this case, the role of the transitions between the ground state |2> and the excited state |3> is played by the second ring resonators, and the role of the transitions between the ground state |1> and the excited state |3> by the first ring resonator. When the Optical path length’s of the two rings are identical, such that $\Phi_1 = \Phi_2 = \Phi$, the transmission spectrum of the drop port displays a *minimum* at the single-ring resonances $\Phi[2\pi] = 0$, resulting in a splitting of the resonance peak. The transmission coefficient of the first coupler, t_2, is analogous to the coupling Rabi frequency Ω_p and determines the spacing between the split modes, i.e. the CRIT line width. For $t_2>0$, a splitting occurs, which leads to a minimum in the absorption. The phase difference between the split modes increases with t_2 taking its maximum value when $t_2 \rightarrow 1$, at which point the spectrum simply becomes identical to that of a ring with twice the optical path length of the individual rings. In this strong-coupling limit, interference between the normal modes of the structure has no significant effect on the resonant features. The absorption at the single-ring resonance is minimized simply because the splitting is large. In the weak-coupling limit, on the other hand, the modes become close together and, if not for interference, their independent overlap would result in significant absorption. In this limit, therefore, it is the interference of light circulating in one ring with that in the adjacent ring that leads to induced transparency.

It has been demonstrated that for *n*-level cascaded atomic systems, the atomic resonance splits into $n-1$ submodes, as a result of the interference between one- and multiple-photon effects, such that $n-2$ dark states occur in the gaps between the resonances [9]. Similarly, for *N* identical coupled microresonators, the resonance frequency splits into *N* submodes, as a result of interference between one- and multiple-ring paths.

Another very important application of the induced transparency effects is in the slow light field. In simple two level atomic systems, slow light occurs at the wings of atomic resonances because the refractive index increases rapidly with frequency across the resonance; i.e., normal dispersion occurs. In fact, on resonance, single over coupled resonators result in slow light. Larger group delays are associated with smaller EIT linewidths. The same is true for CRIT, and one way to obtain larger dispersion and group delays is simply to use large resonators.

EIT is often limited by absorption of the control field, for CRIT there is no collapse of the splitting with propagation since there is no control field to be absorbed. The CRIT line width may be decreased by using larger ring of equal size (analogous to degenerate three-level EIT), by using large resonators of unequal size where the optical path length of the large resonator is an integer multiple of that of the smaller one (analogous to non-degenerate three-level EIT), or by using large numbers of equal-sized resonators (analogous to multilevel EIT).

5.3 Ring and Disk Resonators

The first measurements that we made were on disk resonators. All the equations that we wrote in the last sections for the ring resonators are also true in the case of the disk resonators. The main advantage of using a disk resonator instead of a ring is to the higher quality factors for disk resonators. In fact, the higher Q factor of the disk resonator result from the reduced scattering loss arising from the lack of an inner rim.

Another important property of the microdisk is the fact that the mode size supported by the adjacent waveguide must match the whispering gallery mode width propagating in the disk. Proper mode matching will support single-mode behaviour within the disk and optimize disk-to waveguide coupling.

There is also an effect on the Free Spectral Range, as it’s wider in the case of a disk resonator in comparison to a ring of the same size. It arises because of the lack of the inner rim allows the effective diameter to be smaller for the fundamental whispering-gallery modes of the disk than for the ring. In a disk, as the order of the radial mode increases, the peak of the mode moves toward the center of the disk. In fact, the Free Spectral Range of the disk decreases as the wavelength decreases. In an ideal disk, the low-order modes have the highest Q factors. But since the lowest order mode is confined most closely to the perimeter of the disk, it is most sensitive to side-wall roughness.

5.4 Experimental Results

5.4.a Sample Description

The devices are based on Silicon on Insulator technique. In our case, the layer sequence is a SiO_2 buffer of 1.52 µm, a Si core of 0.205 µm and finally a SiO_2 top cladding of 0.745 µm. The width of the waveguide will be 0.5 µm in all the case. The sizes of the disk/ring are varied. The whole fabrication has been carried out at the CEA-LETI.

5.4.b Ring/disk comparison

We first study the difference between coupled disk resonators and coupled ring resonators. The structure is composed by two coupled disk/ring resonators of 10 µm diameters. The gap between the disks/rings and the waveguide and the resonator is 400nm. Figure 5.5. represents a schema of the structure, and Fig. 5.6. shows an optical image of the sample.

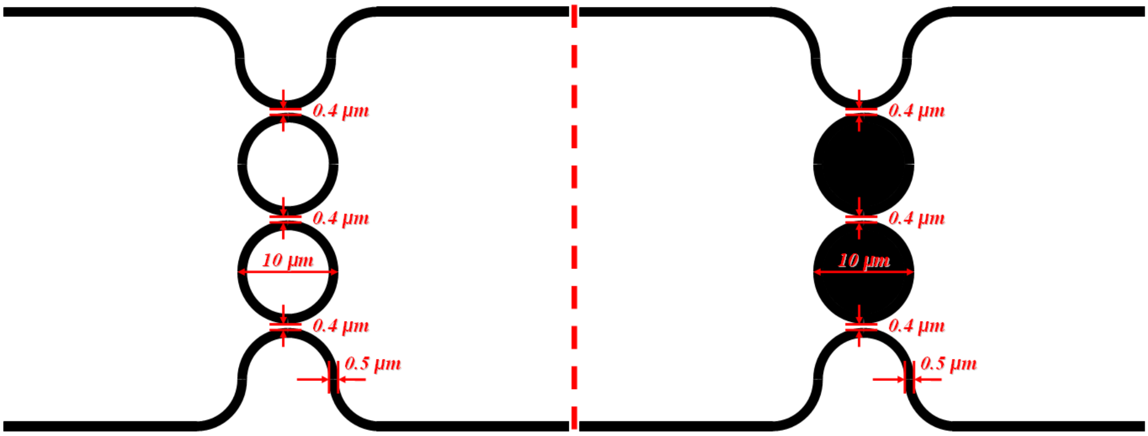

Figure 5.5. Schema of a Double Coupled Ring/disk resonators

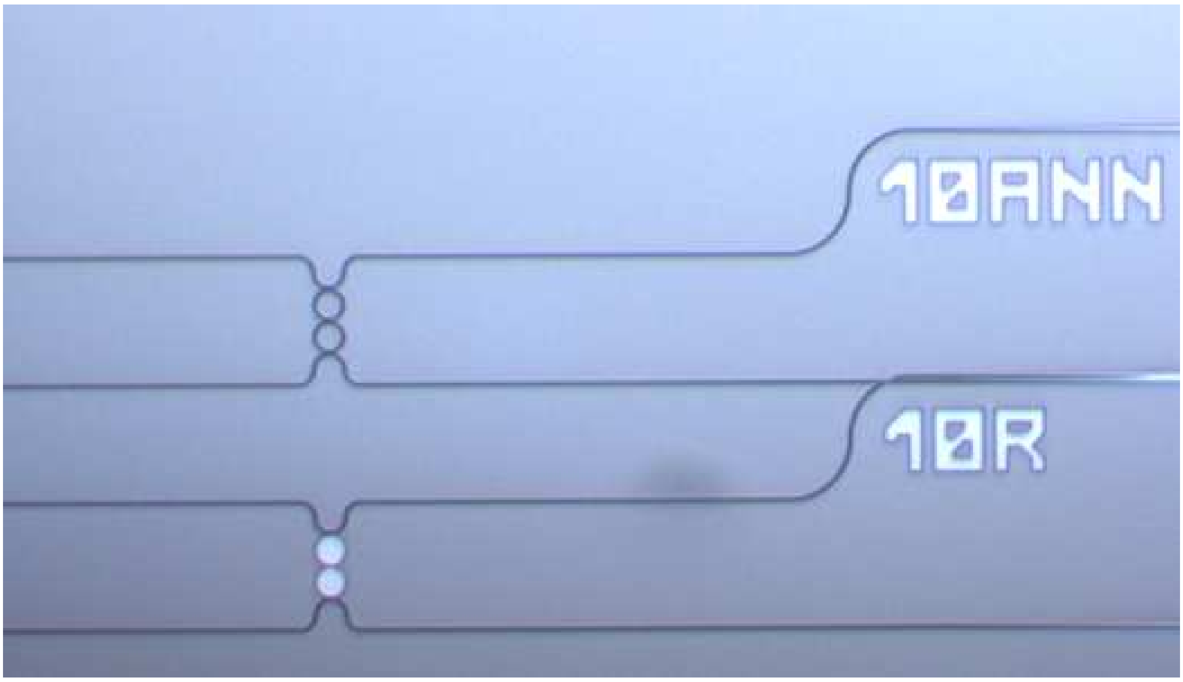

Figure 5.6. Optical image of the structure

In order to facilitate the mode matching, i.e. coupling between the waveguide and the resonator, the waveguide was curved close the resonator. Unfortunately, we observed that this structure generate a lot of losses due to this bending (around 8dB losses more than a structure without curve). But as, in this case, we just want to compare the behavior of coupled ring and disk resonator, this will not affect our study. In figure 5.7 we report a transmission spectrum of the drop port for the two different structures in a large wavelength range for the TM polarisation, where the structures where designed.

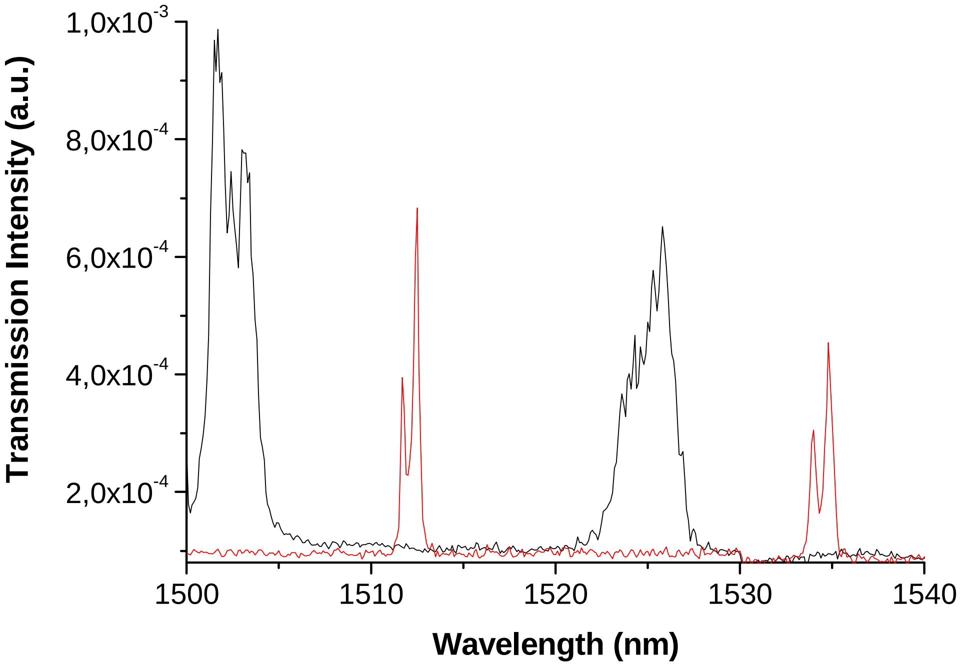

Figure 5.7. Transmission spectrum of the drop in case of two coupled ring resonators (black curve) and disks resonators (red curve)

Disk resonators show high Q resonances, due to the reduced scattering loss arising from the lack of the inner rim. This behaviour is clearly verified in this case, as the width of the resonance peak is almost twice narrower in case of the disks than for the ring.

The free spectral ranges are similar in case of both structures. For example, in the wavelength range of 1500nm-1570nm, we found $\Delta\lambda = 23.6 \pm 0.3$ nm for the 10μm disks resonators and $\Delta\lambda = 24.1 \pm 0.6$ nm in case of the rings resonators. This yields to a group index of 3.22 ± 0.05 for the disks resonators and $n_g = 3.12 \pm 0.1$ for the rings.

5.4.c Coupled Disks resonators

The second structure that we will study is composed of two coupled disk resonators of 8 μm diameters. The gap between the disks/rings and between the waveguide and the resonator is 400nm. Figure 5.8 represents a schema of the structure, and inset of Fig. 5.8. shows an optical image of the sample.

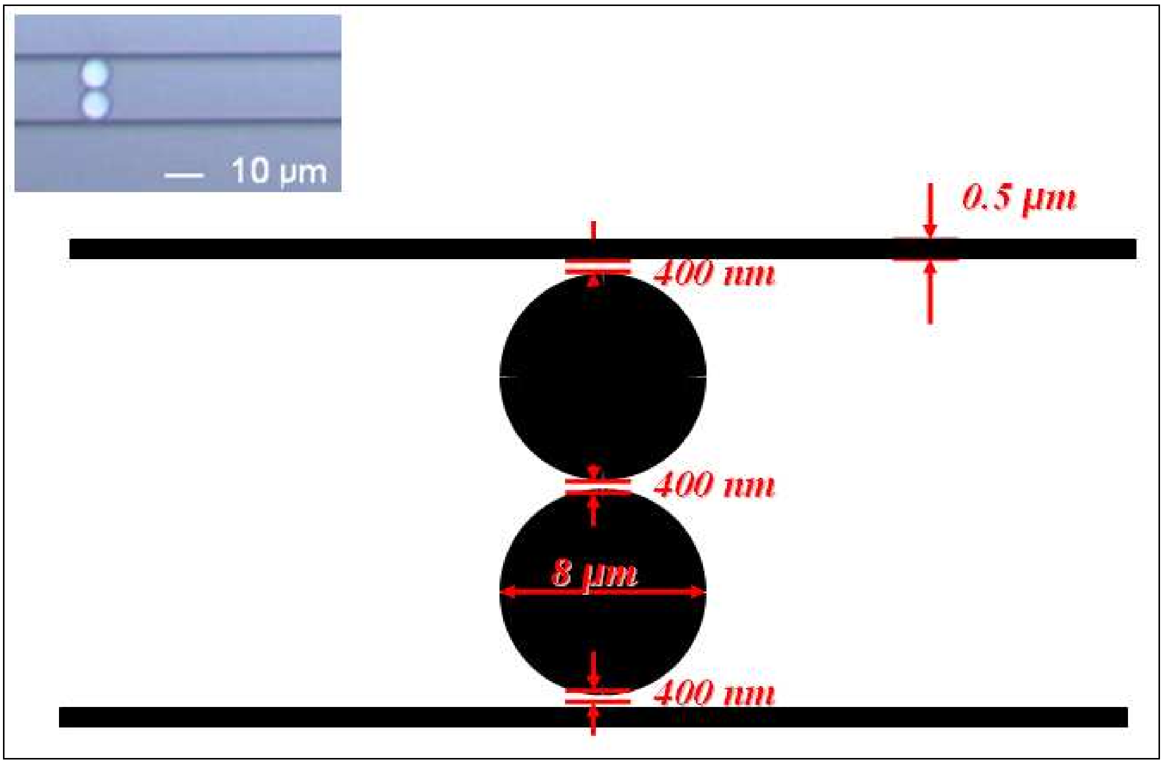

Figure 5.8. Serially coupled 8 μm-disk resonators; (Inset) Optical image of the structure.

Figure 5.9 represents the transmission spectrum of the drop port for both TM and TE polarizations. As the structure was optimized for TM polarization, we didn't see any resonance in the TE polarization. For the TM polarization, we observe various set of resonances, corresponding to multiple-order radial modes of the disk. The most intense peaks correspond to the first order radial mode of the disk (indicated by an arrow in the figure), and the others to the higher order radial modes of the disk. As the radial order increases, we observe that the transmission characteristics worsen.

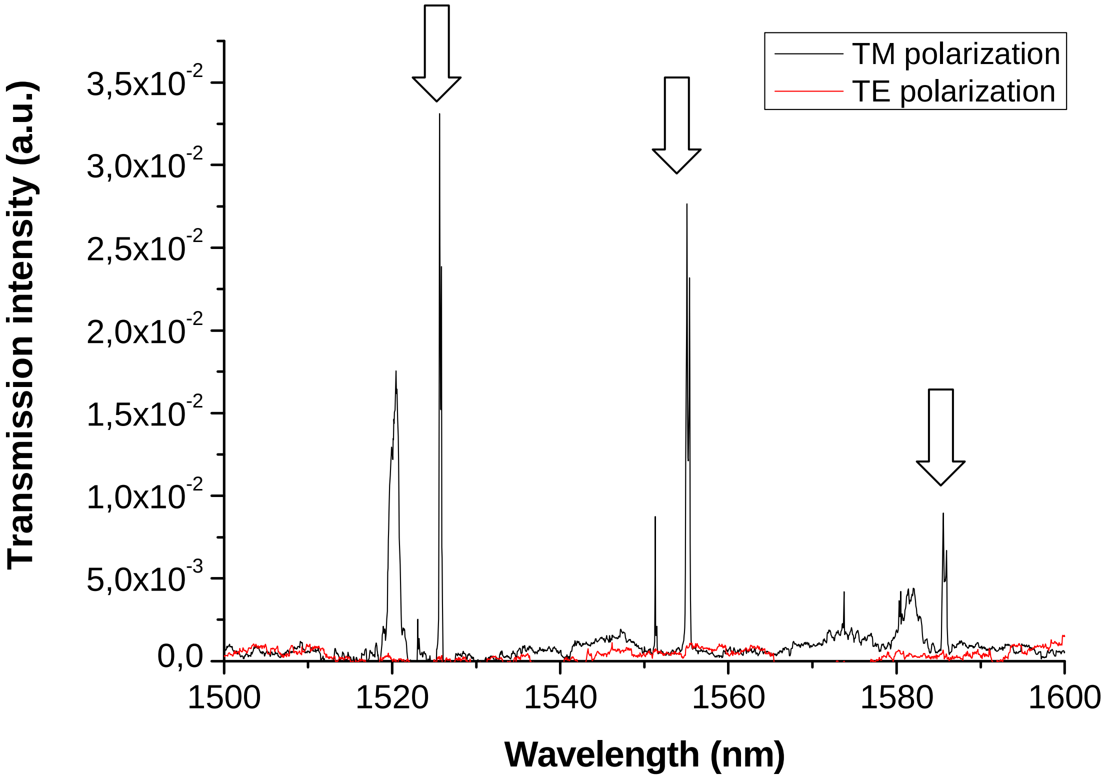

Figure 5.9. Transmission spectrum of the drop port in case of two coupled 8 μm disks resonators for the TM (black curve) and TE (red curve) polarization.

Figure 5.10 represents the double-peak resonance at the drop port at different wavelengths. The abscissa of the figure is normalized to the central frequency of the resonance. We can observe that as the wavelength increase, the width of the resonance peak increases, and the quality factor decreases. At 1525nm, the highest value of Q_{factor} found was 13000 ± 2000, and at 1617nm, the best value measured was 5600 ± 1000.

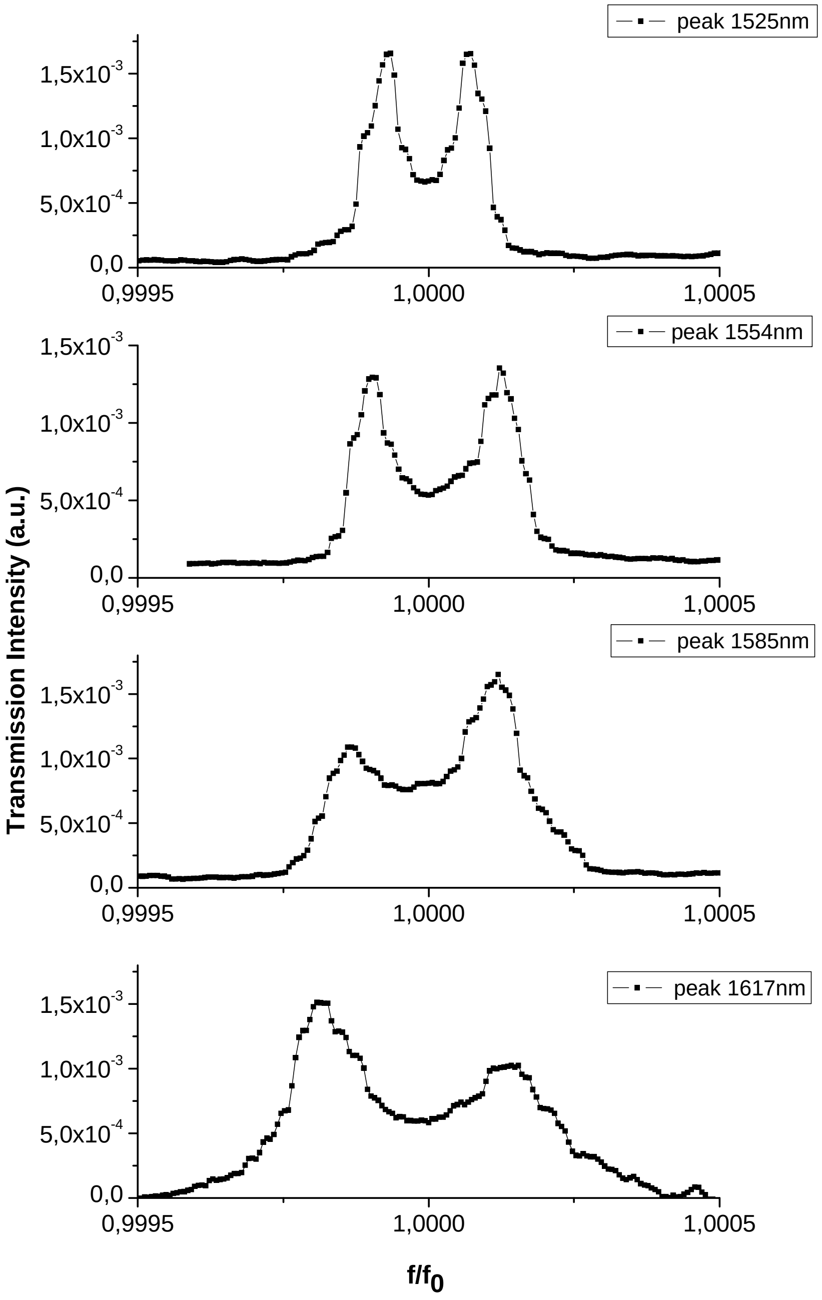

where f_0 is the frequency of the center of the pic

Figure 5.10. Resonance peak of the drop port taken at different resonance wavelengths

From the Free Spectral Range, it's possible to deduce the group index n_g by the equation

$$FSR = \frac{\lambda^2}{2\pi R * n_g} \qquad (5.16)$$

Figure 5.11 represents the values of n_g and FSR measured in a large spectral range.

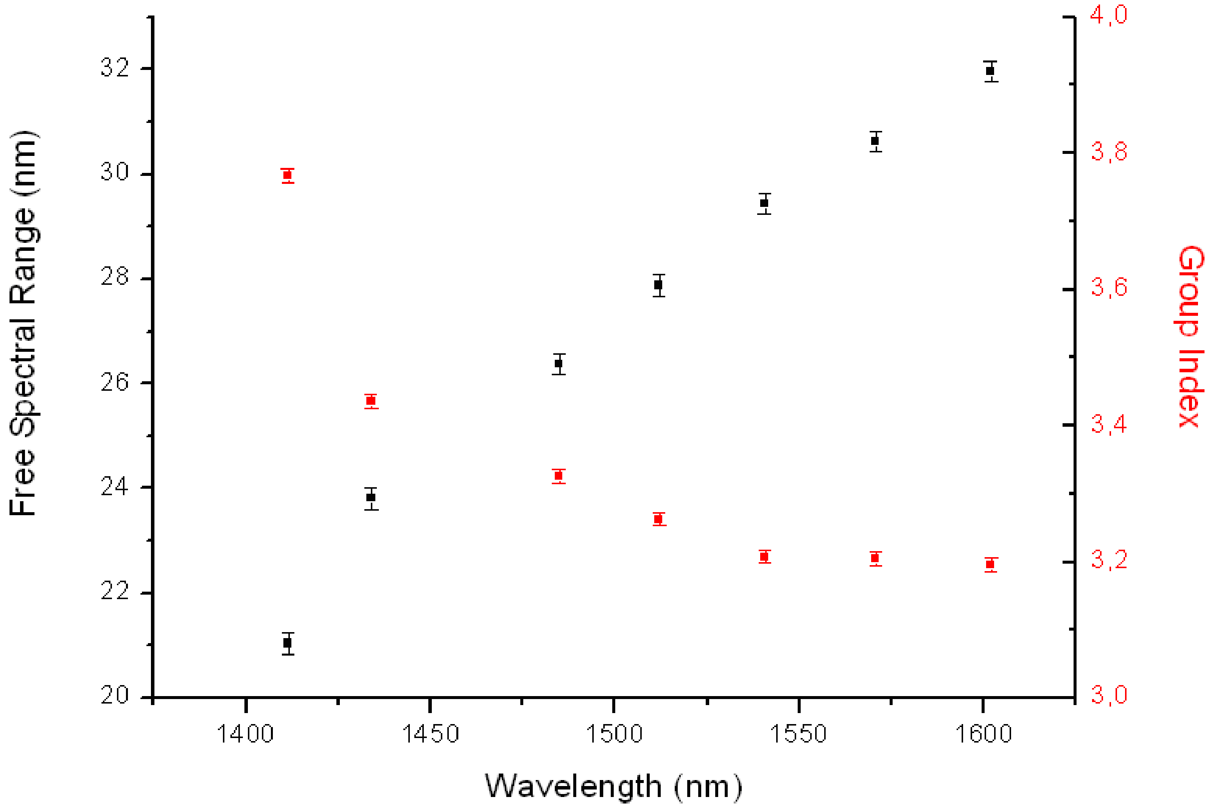

Figure 5.11. Free Spectral Range and Group index for a double 8μm disk resonators structure

We observe an important change in the Free Spectral range as a function of the wavelength. This is due to the decrease of the group index from 3.8 to 3.2. This explains the higher Q factors observed at short wavelength than at large wavelength. In fact, the fundamental mode is much more confined inside our disk resonator, and therefore suffers less losses due to the surface roughness at the wall of the disk. The larger mode confinement also explains the increase of the group index in our system. In simple terms, the mode which is more confined fills more the silicon than the silica. Thus, the effective and group indexes increase.

This result is very interesting also regarding the group velocity of our mode. As we increase n_g, we decrease v_g, the light slow down.

5.4.d CRIT in a double-disk resonators structure

The third structure that we study is composed by two coupled disk resonators of 4 µm diameters. The gap between the disks/rings and between the waveguide and the resonator vary from 400nm to 260nm. Figure 5.12 represents a schema of the structure.

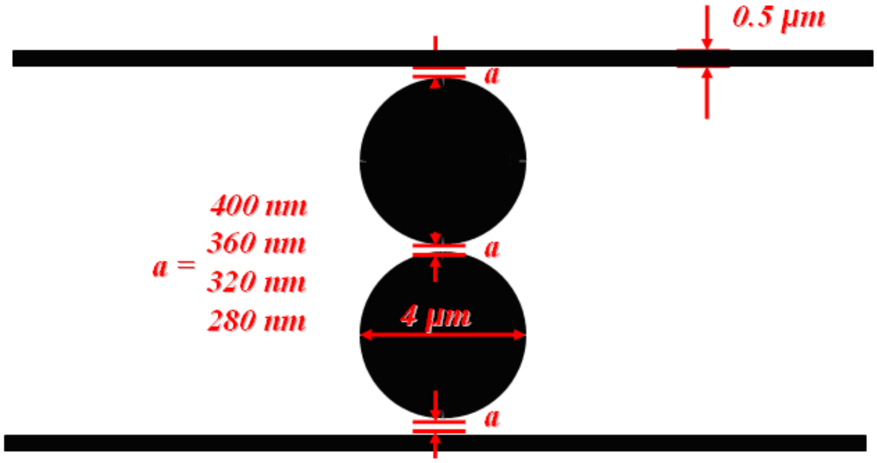

Figure 5.12. Serially coupled 4 µm-disk resonators with different gaps design.

We already discussed that the transmission coefficient between the two resonators is analogous to the coupling Rabi frequency Ω_p in an EIT system, and determines the spacing between the split modes, i.e. the CRIT line width. The transmission coefficient between two disks is directly related to the gap between the disks. Figure 5.13 reports the transmission spectra for the drop port in a large wavelength range for the TM polarization of coupled disks with different gaps.

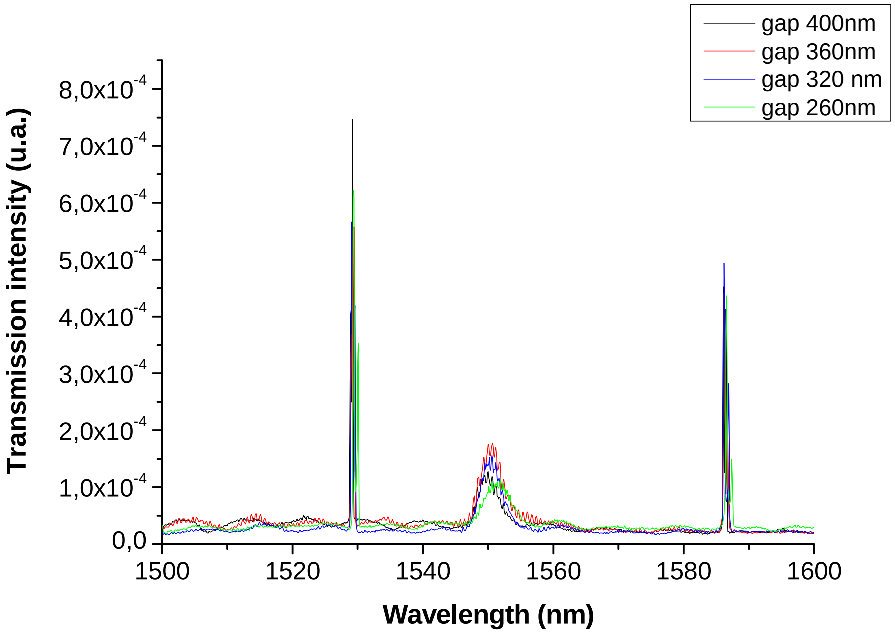

Figure 5.13. Transmission spectrum of the drop port in case of two coupled 4 µm disks resonators for the TM polarization for gap of 400nm (black curve), 360nm (red curve), 320 nm (blue curve) and 260nm (green curve).

We observe, at λ=1550nm, the second order radial peak of the disk. The Free Spectral Range of all structures is similar, as the graphs overlap.

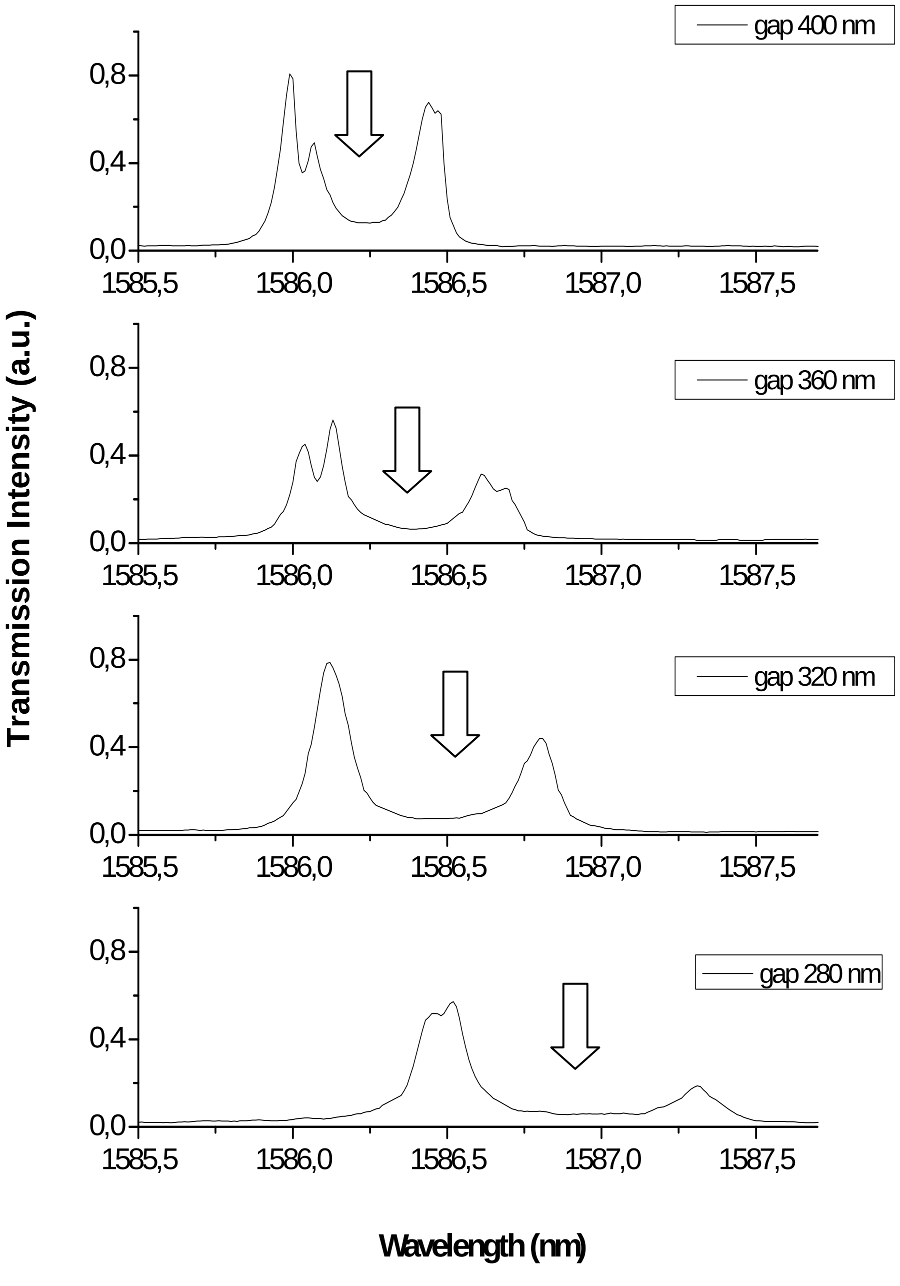

Figure 5.14. Zoom of a resonance of the transmission spectrum of the drop port in case of two coupled 4 μm disks resonators for the TM polarization for gap of 400nm, 360nm, 320 nm and 260nm.

Figure 5.14 shows a blow up of the resonance in transmission for various values of the gap between the two disks (arrows in the graph). The resonance is split in two peaks, with a peak-to peak separation which depends on the gap value. The splitting of the resonance is an evidence of destructive interference between signals coupled into the two disks. The coupling between the disks increases which causes an increase in the two peaks separation. This effect in atomic systems is called the Autler-Townes doublet [10]. Fig. 5.14 shows a proof of CRIT in a system of double-disk resonators, which was already report in the literature in more complex systems, like SCISSOR [11].

5.5 Side-Coupled Integrated Spaced-Sequence of Resonators (SCISSOR)

5.5.a Description and principle of a SCISSOR

In the previous paragraphs, we study a sequence of directly coupled rings, often termed a coupled-resonator optical waveguide (CROW). Another way to couple the rings is through a common waveguide, as depicted in Fig. 5.15. This is the case in a side-coupled integrated spaced sequence of resonators, or SCISSOR [12].

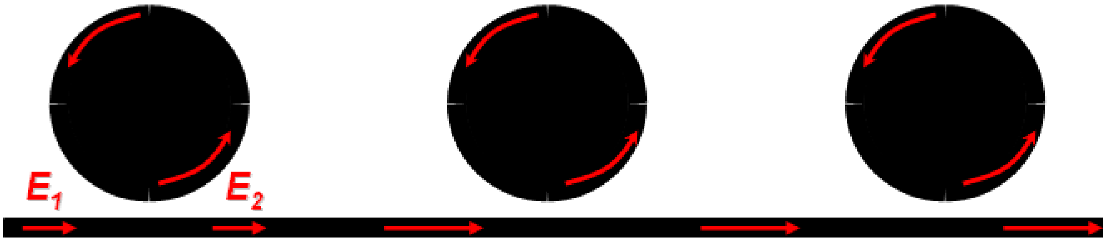

Figure 5.15. Schema of Side-Coupled Integrated Spaced-Sequence of Resonators

In a resonator, the output field E_2 is related to the input field E_1 by the formula

$$E_2(\omega) = e^{i\Phi(\omega)} E_1(\omega) \tag{5.17}$$

where Φ represents the transmitted phase shift. For a sequence of microresonators with unit spacing d, the additional phase imparted by the microresonators modifies the propagation constant of the unloaded waveguide, which becomes $k_{\mathrm{eff}}=n_{eff}\omega/c+m\Phi/d$, where m is the number of resonators. The dispersion relation (k_{eff} vs ω) is thus altered periodically. Near resonance, the resonator contribution Φ/d to the propagation constant becomes sensitively dependent frequency, leading to a reduced group velocity, $v_g=dk_{\mathrm{eff}}/d\omega$.

Then a densely packed collection of high-Q factors resonators, a light wave spends much more time circulating within each resonator than in propagating between resonators, and the group velocity becomes very low. Because the time delay acquired in interacting with each resonator depends critically on the detuning of the optical wave from the resonance frequency, this device displays tailorable dispersion with a magnitude much larger than that of conventional materials.

The addition of a second common coupling channel to a SCISSOR as depicted in Fig. 5.16 enables distributed feedback. In contrast to the single-channel case, the spacing between resonators d is now important because resonances can develop not only within the resonators but also among them.

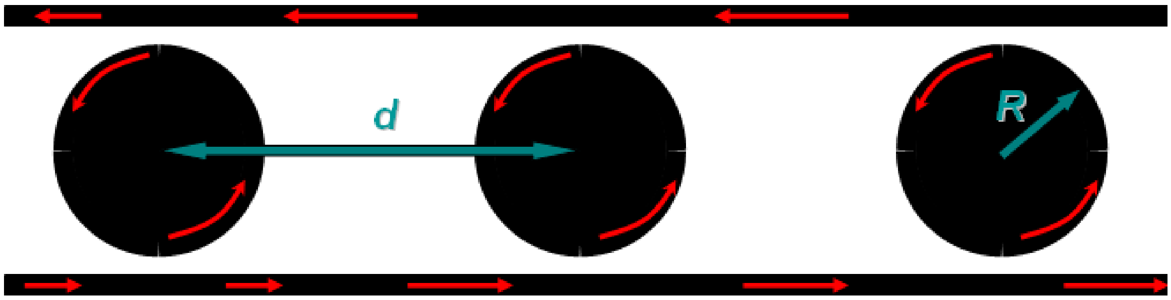

Figure 5.15. Design of a Double channel SCISSOR

When the circumference of the microresonator is an integer multiple of the wavelength ($2\pi R = m_R\lambda/n_{eff}$, with m_R an integer), the light goes inside the resonator, as in the previous case. But in this structure the presence of the drop waveguide allows another periodicity to become relevant; that provided by the periodic sequence of disks. When the signal wavelength satisfies the Bragg condition, $2d = m_B\lambda/n_{eff}$, with m_B an integer, constructive interference occurs on the drop waveguide and the signal is reflected back along the drop waveguide. Finally, if the wavelength satisfies both $\lambda = 2\pi R n_{eff}/m_R$ and $\lambda = 2d n_{eff}/m_B$, we have the occurrence of CRIT: the signal is transmitted to the through port. A supermode among nearly disks occurs. Fig. 5.16 summarizes these three cases.

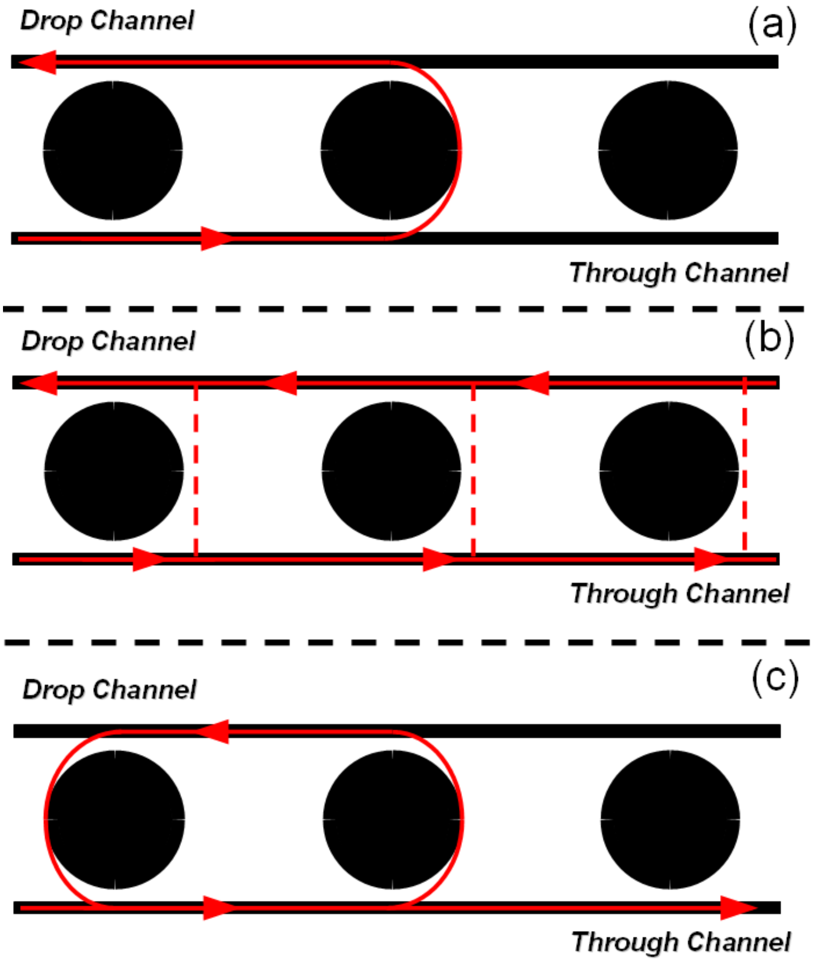

Figure 5.16. Double channel SCISSOR when λ verifies the condition of resonance on the resonator (a), when λ verifies the Bragg condition of the structure (b), and when λ verifies the condition of resonance of the resonator and the Bragg condition (c)

5.5.b Single channel SCISSOR

The first studied SCISSOR structure is composed by eight coupled disk resonators of 14 µm diameters. The disks are coupled only via the input waveguide. The gap between the disks and the waveguide is 300 nm. The distance between each resonator is 22 µm. Figure 5.17 represents a schema of the structure.

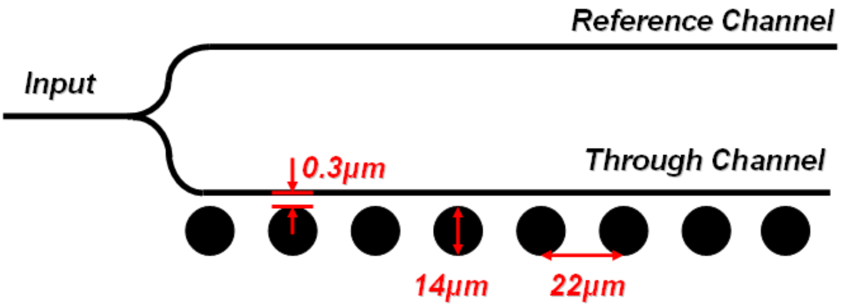

Figure 5.17 Schema of a 14 μm-microdisk SCISSOR "single channel"

By dividing the response of the through channel by the reference channel, the transmission can be measured. Figure 5.18.a represents the normalized spectra of the through channel for TM polarization. Figure 5.18.b represents also the normalized spectra of the through port, but centred on a resonance and on a smaller range. As the structure was optimized for TM polarization, we didn't see any resonance in the TE polarization. In a large range, we observe in the spectrum various resonances due to the SCISSOR. By taking a look at a single resonance in Fig 5.18.b, we observe various peaks and dips inside the resonance. The disks show many resonant modes, each one with a very high Q factor. The division of the resonance band is due to the different resonances of the SCISSOR system. As the disks have quite large diameter, a difference of some nanometers in the size can split the resonance of some angstroms. As the Q factor is very high (best value 35000 ± 5000), the resonances of the eight disks are not superposed but shifted by a few angstroms.

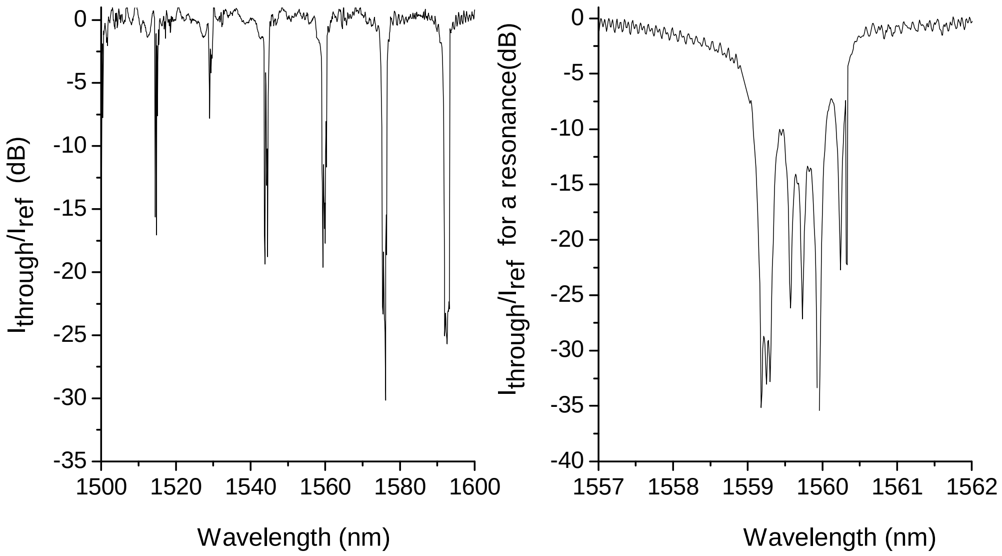

Figure 5.18 Normalized spectra of the through port as a function of the wavelength in a large range (a) and a single resonance (b)

Figure 5.19 represents the normalized spectra of the through port for the single waveguide SCISSOR structure with ring resonators. As the Q factors of the ring resonators are smaller than those of disk resonators, the extinction ratio is smaller (8dB vs 30dB). In this case, no splitting of the resonances is observed.

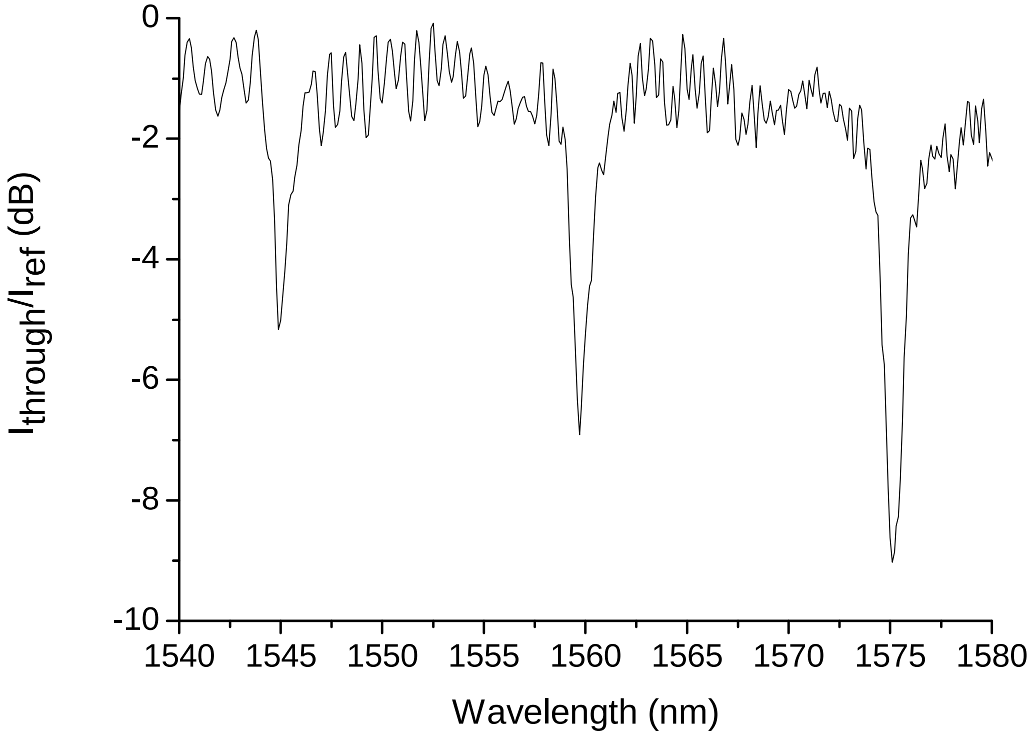

Figure 5.19 Normalized spectra of the through port in function of the wavelength in a large range for a single waveguide SCISSOR structure in case of ring resonators

5.5.c Double Channel SCISSOR

The second studied SCISSOR structure is composed by eight coupled ring resonators of 14 µm diameters coupled with both an input waveguide, the through port, and with an output waveguide, the drop port. The gap among the rings and the waveguides is 300 nm. The resonators are spaced 22 µm apart. Figure 5.20 represents a scheme of the structure.

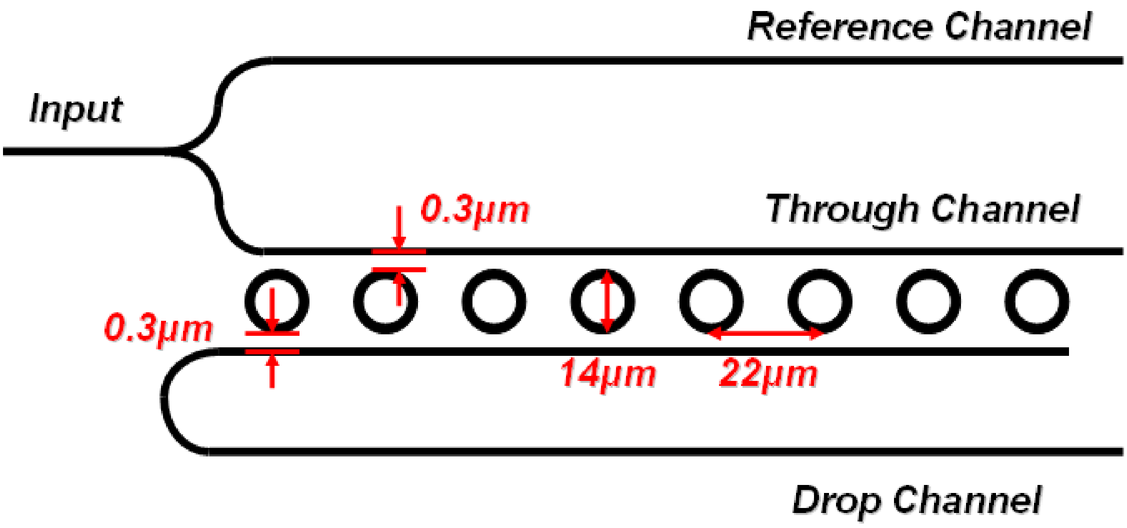

Figure 5.20. Scheme of a 14 µm-microring SCISSOR "double channel"

In order to have constructive interference between each resonator, we choose the distance *d* in order to have a π phase-shift for a signal propagating along this distance. This is the same phase-shift for a mode passing trough a half-disk. Thus a signal which goes along two nearly ring has a 2π phase shift with respect to a signal which is propagating along the through channel.

Figure 5.21.a shows the transmission spectrum of the through and the drop channels in a large wavelength range for TM polarization. Figure 5.21.b represents in more details a resonance. We observe first that both resonances are perfectly aligned, which means that the transmission between the waveguides and the rings is well optimized. When we take a look at Fig. 5.21.b, it seems that the resonance peak of our structure is splitting in two. In a large wavelength range, this splitting increases when we go to higher wavelengths. This means that two different phenomena happen in this structure. As we discussed in the previous section, a huge signal at the drop port is caused by wavelengths which satisfy the Bragg conditions and wavelengths which satisfy the single conditions. The two intervals are observed in fig. 5.21 and indicated by the corresponding arrows.

In Fig. 5.21.b, in the huge drop signal resonances, we can observe very high Q factor dips ($Q_{\text{factor}} \approx 30000$) in the drop port. These dips are due to EIT. In fact, at the wavelengths where two or more rings are completely resonant, we can have a condition of transparency (large transmitted signal). As this effect is very dissipative, the signal is affected by large losses and the transmission at the output of the through port is negligible. This explains why no peaks are observed in the through port.

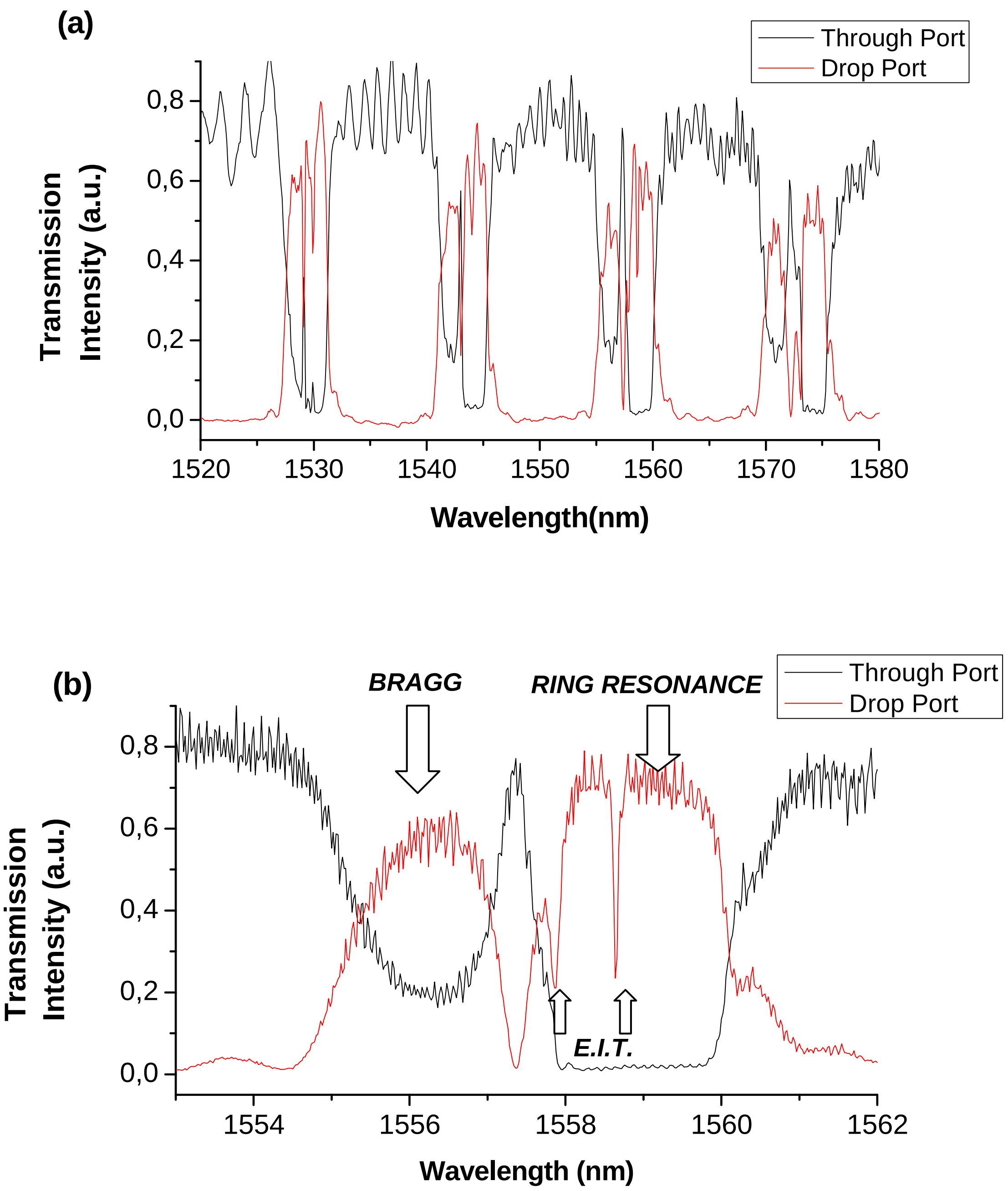

Figure 5.21. Transmission spectrum of the through port (black curve) and the drop port (red curve) for a double-channel SCISSOR in a large wavelength range (a) and for a resonance of the structure (b)

It is worth noting that the splitting between the Bragg region and the resonance region have a wavelength dependence. The coupling coefficient between the resonators and the waveguides affects the Free Spectral Range of the resonators, as we observed in paragraph 5.4.c. for double-disks resonators. On the opposite, the Free Spectral Range of the Bragg resonances remains constant as a function of the wavelength. Then at low wavelengths, an overlap of these two effects is observed in the transmission spectra (Fig. 5.21.a).

5.6 Top-view system[8]

5.6.a Description of the Set-up

In order to observe the scattered light, we implemented a new set-up to collect this light with an infrared camera. A scheme of the set-up is shown in Fig.5.22. As the working distance of the objectives is short, we just used a 10x objective connected to the zoom, in order to facilitate the alignment of our set-up.

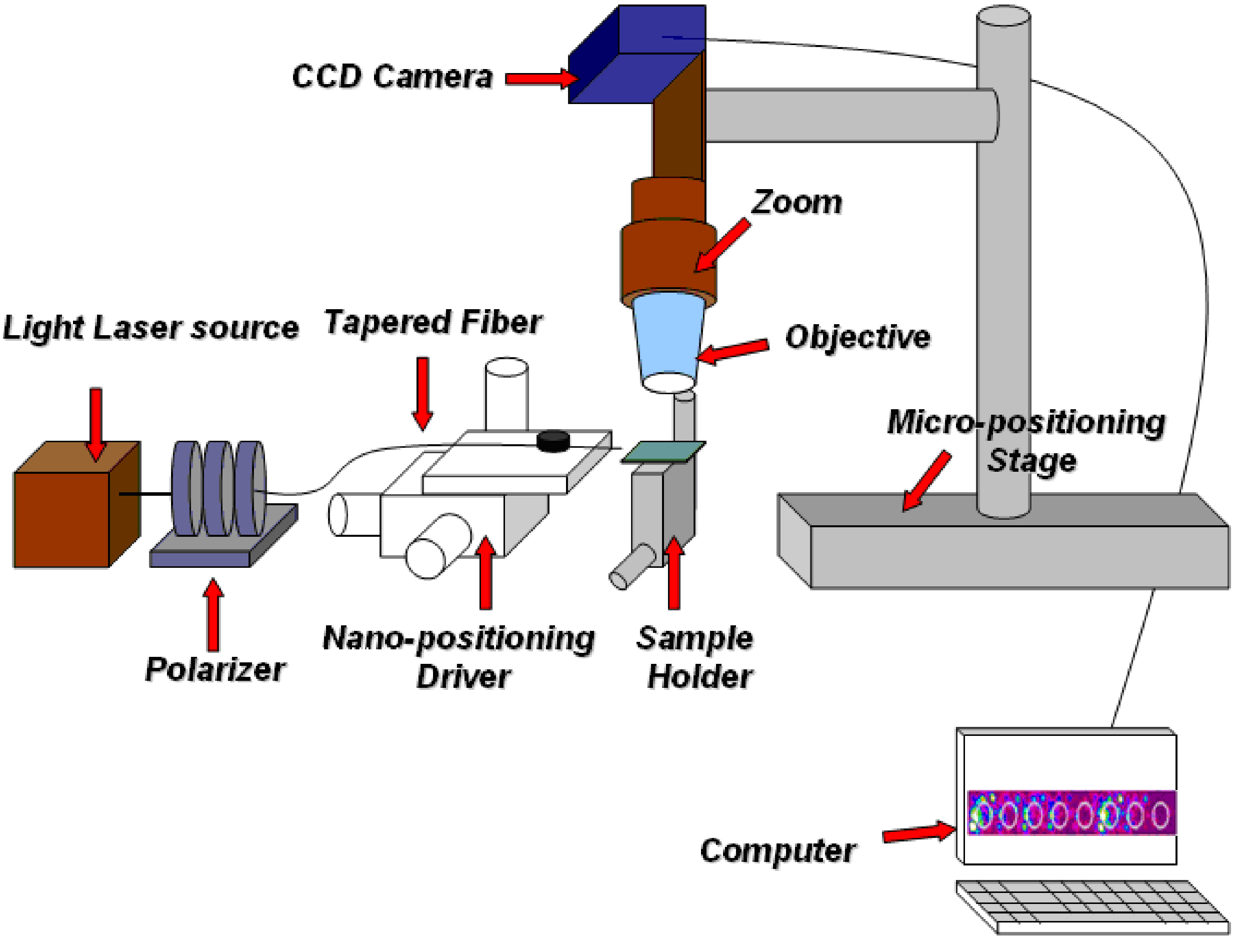

Figure 5.22. Experimental set-up created to measure the top-scattering from the samples

All the collection system was connected to a micro-positioning stage in order to select the structure and be able to zoom on each resonator. By changing the wavelength of the signal, we can measure how the disks scatter as a function of the input wavelength. Figure 5.23 represents a top-view image of the double channel SCISSOR structure at a certain wavelength. We insert white circles

---

[8] This set-up was developed by Mattia Mancinelli and me within his Master Thesis [Caratterizzazione di sequenze di risonatori accoppiati in ottica integrata in silicio]

where the rings are in order to understand better the figure. We observe at this wavelength a large scattering due to the third and fourth resonators, some scattering from the first and the second resonators and no scattering from the others.

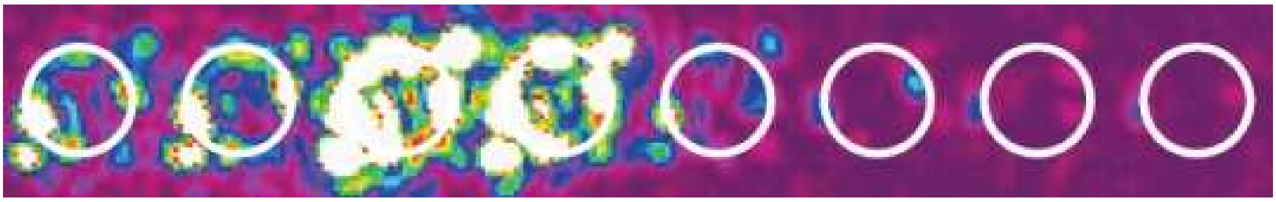

Figure 5.23. Top-view image of a double channel SCISSOR

A software was also installed on the computer to register movies showing the evolution of the structure in function of the wavelength.

5.6.b Experimental results

Fig. 5.24 represents the transmission spectrums for the through and the drop ports in case of a resonance of the structure and the light scattered from this structure in the same wavelength range. The scattered light signal is acquired by integration of the camera counts over the whole observation region.

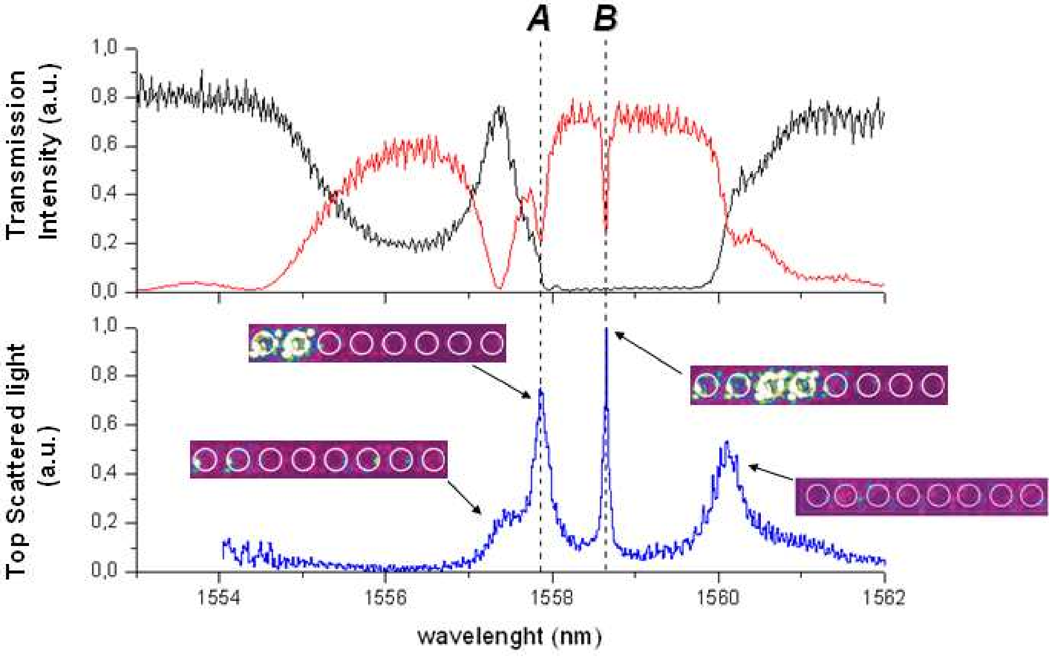

Fig. 5.24. Transmission spectrum for through (black curve) and drop (red curve) ports for a resonance of the structure and top scattered light from all the structure (blue curve) in the same wavelength range.

We remember that the resonance of our structure is divided in two: one is due to the Bragg effect (from λ=1554.5 to λ=1557.2nm) and the other is due to the resonances of our ring resonators (from λ=1557.5 to λ=1560.1nm). We observe that out of the EIT-like peaks, the SCISSOR scattered light only at the edge of the resonance peak of our resonators (λ=1557.5 and λ=1560.1nm). At this wavelengths, the group velocity decreases. This effect is very dissipative and so the scattering increases. If we observe the top scattered light image at these wavelengths, we do wee a quite homogeneous image which is due to the light scattered by all the rings. As all the structure is very dissipative at this wavelength, the value of the scattered light can reach quite important value.

For the EIT-like peaks, we observe that only few rings scattered light (two for the peak A and fours for the peak B). This is due to the random fluctuations in the range diameters and coupling gaps which allow resonant coupling of only a few of them.

As this effect is very dissipative, we do not observe any signal at the output of the through port. This is also confirmed by the top scattered images. We observe that the losses due to scattering are very high when EIT occurs, which means that the signal suffers very high losses at these wavelengths.

5.6.c Effects of structural disorders on the EIT-like peaks

In order to conclude our work on this structure, we study the resonance peaks for various samples in order to verify the reproducibility of the EIT-like effects on our system. Figure 5.25 represents the transmission spectrum of the drop port for the EIT peaks in three different samples.

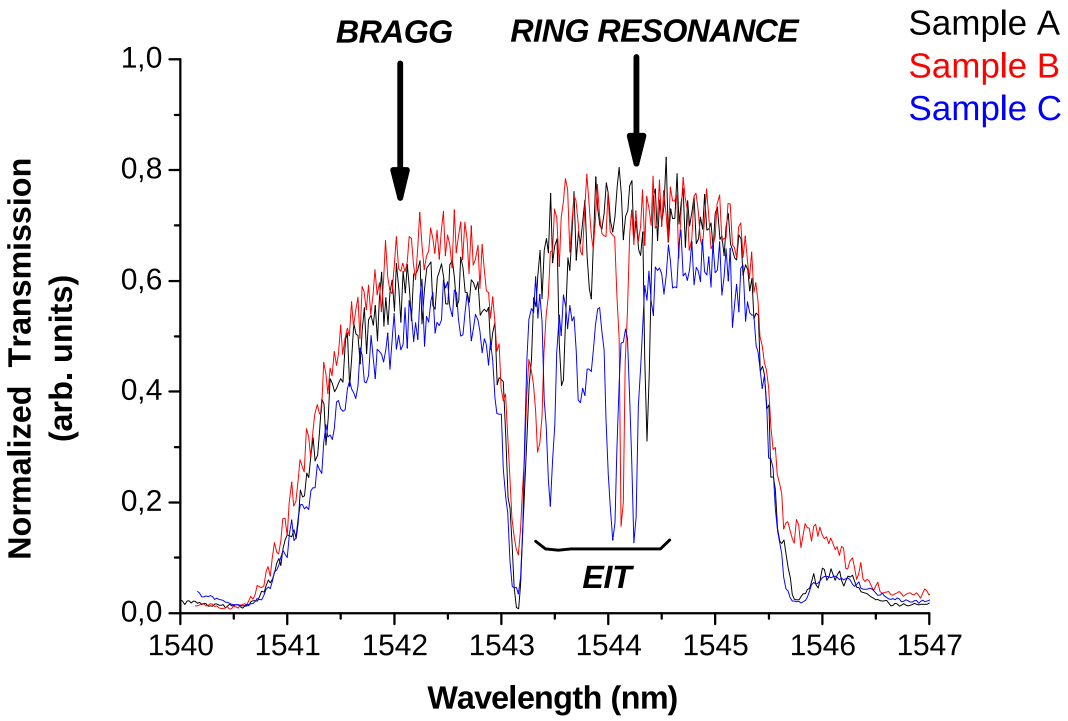

Fig. 5.25. Transmission spectrum the drop port for a resonance of the structure in case of three different samples

All show the two characteristics Bragg and resonator regions at almost the same wavelengths. What they differ from is for the fine structure associated to the EIT. In fact, due to the random errors in the fabrication, resonant coupling occurs for a different number of rings in the various samples. Thus the number of EIT dips is different.

The Bragg-band is not affected by these disorders, due to the fact that the Bragg-effect is caused by the entire structure. The high Q-factors EIT-like peaks are very sensitive to small disorders in the structure, like the variation of the gap between each ring or the change of the diameter of the ring, both of the order of some nanometers. These ones can affect both the position of the peak, but also the value of the Q-factor of the peak. If we take a top scattered image of this resonance, we can also observe that for the three samples, the rings affected by the EIT-effect are different in each case, which confirm the presence of small disorders in our structure.

5.7 Conclusion

In this work, we studied various configurations of coupled disk/ring resonators. With these various structures, we observed the differences in the transmission spectrum between rings and disks resonators, we noticed the whispering gallery modes and the effect of the gap in the CRIT effect for a serially double-disks resonator.

We have also characterized the behaviour of complex SCISSOR devices, composed by multiple microrings. For the first time we demonstrate the presence of EIT-like band even in complex structures. Extremely small differences between adjacent rings can give rise to the appearance of EIT states, spanned over only few rings at a time and showing great Q-factor and strong out-of-plane scattering.

References

[1]. Rosenberger, *Phys. Rev. A* **71**, 043804 (2005).

[2]. D. D. Smith, H. Chang, K. A. Fuller, A. T. Rosenberger, and R.W. Boyd, *Phys. Rev. A* **69**, 063804 (2004).

[3]. Q. Xu et al., *Phys. Rev. Lett.* **96**, 123901 (2006).

[4]. W. E. Lamb and R. C. Retherford, *Phys. Rev.* **81**, 222 (1951).

[5]. P. R. Hemmer and M. G. Prentiss, *J. Opt. Soc. Am. B* **5**, 1613 (1988).

[6]. G. L. Garrido Alzar, M. A. G. Martinez, and P. Nussenzveig, *Am. J. Phys.* **70**, 37 (2001).

[7]. A. Yariv, Y. Xu, R. K. Lee, and A. Scherer, *Opt. Lett.* **24**, 711 (1999).

[8]. D. D. Smith, H. Chang, and K. A. Fuller, *J. Opt. Soc. Am. B* **20**, 1967 (2003).

[9]. D. McGloin, D. J. Fulton, and M. H. Dunn, *Opt. Commun.* **190**, 221 (2001).

[10]. S. H. Autler, C. H. Townes, *Phys. Rev.* **100**, 703 (1955).

[11]. Q. Xu, S. Sandhu, M. L. Povinelli, J. Shakya, S. Fan, and M. Lipson, *Phys. Rev. Lett.* **96**, 123901 (2006).

[12]. J. E. Heebner, R. W. Boyd, and Q.-H. Park, *J. Opt. Soc. Am. B* **19**, 722 (2002).

General Conclusion

In this conclusion, we will summarize the main results about the various Si-based materials and devices studied during these three years.

First, we characterized SiOC films produced via polymer pyrolysis of sol-gel derived films. The objective was to achieve bright emission and high external quantum efficiency in high-quality thin film. We wanted thin films for possible applications in waveguides. We were able to observe a very bright yellow photoluminescence from our samples, due to the formation of SiC and C clusters into SiO_2 matrix at high temperature, confirmed by Fourier-transform infrared (FTIR) spectroscopy and X-ray photoelectron spectroscopy (XPS). This photoluminescence was quantified with the measure of the External Quantum Efficiency. Values of 5% were found for T^HD^H2 films and 11.5% for T^H films. These values are very encouraging as they compare to the best results reported in the literature about Si nanomaterials so far.

In the second part, we characterized several Silicon On Insulator basic building blocks like Y-junctions, MMIs and bends. This preliminary study is needed to develop Silicon Microphotonics components and circuits on SOI platform. The optimised structures are then used to make various devices based on coupled disk/ring resonators and to observe the difference between rings and disks resonators. For the first time we demonstrated the presence of EIT-like effect even in complex structures, like complex SCISSOR devices, composed by multiple microrings.

Finally, we have demonstrated low losses nano-Si slot waveguides and high-quality factor coupled ring resonators. In fact, by optimizing the annealed SRSO (i.e. Si-nc) in the slot, we have significantly reduced the propagation losses and at the same time we add new functionalities due to the Si-nc optical properties (i.e. light emission and/or non-linear optical effects). For example, the high-quality factors demonstrated in single and double ring resonators, if associated to the sizeable non-linear effect of nano-Si in the slot, can enable all optical switches and tunable telecommunications filters. Finally, we were able to design and characterize a one-dimensional photonic crystal structure based on horizontal slot waveguide, which, by concentrating the field intensity inside the *slot*, allow us to increase the non-linear effects of the Si-nc increasing the interaction time between the material and the electromagnetic fields propagating inside the waveguide.

As a final outcome, this Thesis shows that many optical devices can be engineered in silicon-based materials, using their characteristic properties like the high visible luminescence in case of the SiOC or the high refractive index difference in case of the Silicon on Insulator, which causes an high spatial confinement of the optical mode. All these properties are also exploited and improved with the addition of new structure, like the slot waveguides, or materials, like Si-nc, in order to demonstrate novel physical effects.

Appendix 1: MMI Theory

In this paragraph we recall the basic principles of MMI theory explained by L. B. Soldano and E.C.M. Pennings[9]. The central structure of an MMI device is a waveguide designed to support a large number of modes (typically ≥ 3). In a step-index multimode waveguide of width W_M, ridge (effective) refractive index n_r and cladding (effective) refractive index n_c. The waveguide supports m lateral modes with mode numbers v = 0, 1 ... (m-1) at a free-space wavelength λ_o. The propagation constant is noted β_0. We note the "effective" width W_{Ev}, takes into account the (polarization-dependent) lateral penetration depth of each mode field, associated with the Goos-Hähnchen shifts at the ridge boundaries. For high-contrast waveguides, the penetration depth is very small so that $W_E \approx W_M$. In general, the effective widths W_{Ev}, can be approximated by the effective width W_{E0}, corresponding to the fundamental mode. We note W_E for simplicity.
By defining L_π as the beat length of the two lowest-order modes as

$$L_\pi = \frac{\pi}{\beta_0 - \beta_1} \approx \frac{4 n_r W_e^2}{3\lambda_0} \qquad \text{(A.1)}$$

We can note the propagation constants as

$$(\beta_0 - \beta_v) \approx \frac{v(v+2)\pi}{3L_\pi} \qquad \text{(A.2)}$$

Where v is the mode number. An input field profile $\Psi(y, 0)$ imposed at $z = 0$ and totally contained within W_e (Fig. 4.10), will be decomposed into the modal field distributions $\psi_v(y)$ of *all* modes:

$$\Psi(y,0) = \sum_v c_v \psi_v(y) \qquad \text{(A.3)}$$

where the summation should be understood as including guided as well as radiative modes. The field excitation coefficients c_v, can be estimated using overlap integrals

---

[9] L. B. Soldano and E.C.M. Pennings "Optical multi-mode interference devices based on self-imaging: principles and applications," IEEE J. Lightwave Technol. **13**, 615-627 (1995)

$$c_v = \frac{\int \Psi(y,0)\psi_v(y)dy}{\sqrt{\int \psi_v^2(y)dy}} \tag{A.4}$$

Based on the field-orthogonality relations.

If the input field Ψ(y, 0) does not excite radiative modes it can be decomposed in terms of the m guided modes only:

$$\Psi(y,0) = \sum_{v=0}^{m-1} c_v \psi_v(y) \tag{A.5}$$

The field profile at a distance *z* can then be written as a superposition of all the guided mode field distributions

$$\Psi(y,z) = \sum_{v=0}^{m-1} c_v \psi_v(y) \exp\left[j(\omega t - \beta_v z)\right] \tag{A.6}$$

A useful expression for the field at a distance z = *L* is then found by substituting (A.2) into (A.6)

$$\Psi(y,z) = \sum_{v=0}^{m-1} c_v \psi_v(y) \exp\left[j \frac{v(v+2)\pi}{3L_\pi} L\right] \tag{A.7}$$

It will be seen that, under certain circumstances, the field Ψ(y, L) will be a reproduction (self-imaging) of the input field Ψ(y, 0). Let's write some useful equality.

$$\begin{gathered} v(v+2) = \text{even for } v \text{ even, or odd for } v \text{ odd} \\ \psi_v(-y) = \psi_v(y) \text{ for } v \text{ even, or} -\psi_v(y) \text{ for } v \text{ odd} \end{gathered} \tag{A.8}$$

By inspecting (A.7), we notice that Ψ(y, L) will be an image of Ψ(y, 0) if

$$\exp\left[j \frac{v(v+2)\pi}{3L_\pi} L\right] = 1 \text{ or -1} \tag{A.9}$$

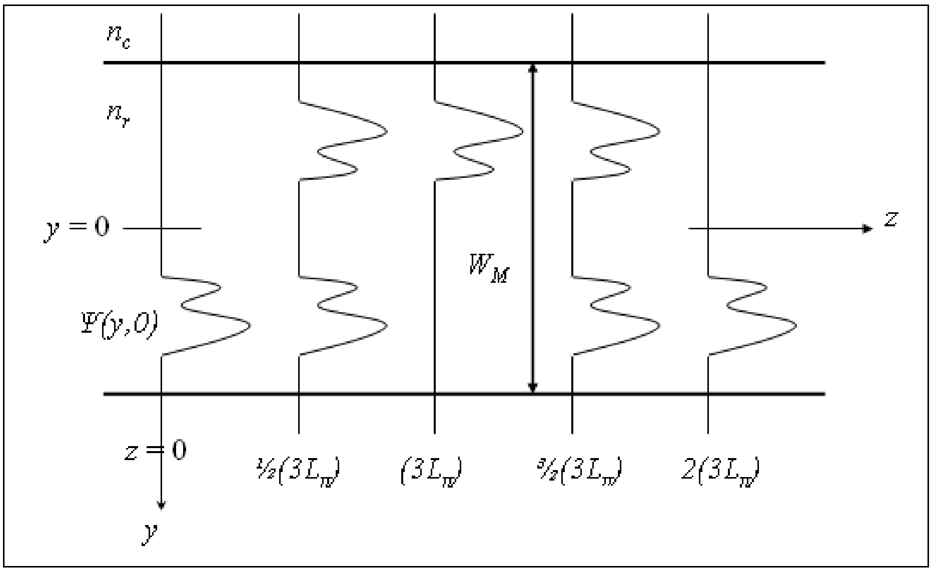

Fig. A.1. Multimode waveguide showing the input field Ψ(y, 0), a mirrored single image at (3L_π), a direct single image at 2(3L_π,) and two-fold images at 1/2(3L_π) and 3/2(3L_π).

The first condition means that the phase changes of all the modes along *L* must differ by integer multiples of 2*π*. In this case, all guided modes interfere with the same relative phases as in *z* = 0; the image is thus a direct replica of the input field.

The second condition means that the phase changes must be alternatively even and odd multiples of *π*. In this case, the even modes will be in phase and the odd modes in antiphase. Because of the odd symmetry stated in (A.8), the interference produces an image mirrored with respect to the plane y = 0.

Taking into account (A.8), it is evident that the first and second condition of (A.9) will be fulfilled at $L = p(3L_\pi)$ with p=0, 1, 2 … for p even and p odd, respectively.

In addition to the single images at distances given above, multiple images can be found as well. Let us first consider the images obtained half-way between the direct and mirrored image positions, i.e., at distances $L = \frac{p}{2}(3L_\pi)$ with p=1,3,5…The last equation represents a pair of images of Ψ(y, 0) in quadrature and with amplitudes 1/√2, at distances *z* = 1/2(3L_π), 3/2(3L_π), . . . as shown in Fig. A.1. This two-fold imaging can be used to realize 2x2-3dB couplers.

Publications

In international peer-reviewed scientific journals (submitted, in press and published):

- R. Guider, A. Karakuscu, G. D. Sorarù and L. Pavesi, “Optical characterization of SiOC thin films prepared by pyrolysis of sol gel precursors”, submitted to *Thin Films Solids* (2009).

- R. Guider, N. Daldosso, A. Pitanti, E. Jordana, J. M. Fedeli and L. Pavesi, “NanoSi low loss horizontal slot waveguides coupled to high Q ring resonators”, *Optics Express* **17**, 20762–20770 (2009).

- A. Karakuscu, R. Guider, L. Pavesi and G. D. Sorarù, “White luminescence from sol-gel derived SiOC thin films”, *Journal of American Ceramic Society* **92**, 2969-2974 (2009).

- Z. Yuan, A. Anopchenko, N. Daldosso, R. Guider, D. Navarro-Urrios, A. Pitanti, R. Spano and L. Pavesi, “Silicon nanocrystals as an enabling material for silicon photonics”, special issue on Silicon Photonics edited by D. Lockwood, L. Tysbeskov, and M. Ichikawa, *Proceedings of the IEEE* vol. 97 n. 7, 1250-1268 (july 2009).

- R. Adamo, A. Anopchenko, P. Bettotti, M. Cazzanelli, E. D'Amato, N. Daldosso, L. Ferraioli, E. Froner, Z. Gaburro, R. Guider, S.M. Hossain, D. Navarro-Urrios, A. Pitanti, S. Prezioso, M. Scarpa, R. Spano, M. Wang, L. Pavesi, “Low dimensional silicon structures for photonic and sensor applications”, *Appl. Surf. Sci.* **255**, 624 (2008).

Books contributions

- A. Anopchenko, N. Daldosso, R. Guider, D. Navarro-Urrios, A. Pitanti, R. Spano and L. Pavesi, “Photonics application of Silicon nanocrystals”, Silicon Nanocrystals; Fundamentals, Synthesis and Applications, edited by L. Pavesi and R. Turan (Wiley-VCH Verlag GmbH, Berlin 2009)

- O. Anopchenko, P. Bettotti, M. Cazzanelli, N. Daldosso, L. Ferraioli, Z. Gaburro, R. Guider, D. Navarro-Urrios, A. Pitanti, S. Prezioso, R. Spano and L. Pavesi, “Low dimensional silicon to enable silicon photonics, Highlights on Spectroscopies of Semiconductors and Nanostructures”, Conference Proceedings - Italian Physical Society, Editrice Compositori; 1999, vol. 94, pages 231-242, ISSN 1122-1437 (2007)

Conference proceedings and contributions

- A. Karakuscu, R. Guider, L. Pavesi and G. D. Sorarù, “SiCO Thin Films: a Novel LED Material”, 33rd International Conference & Exposition on Advanced Ceramics and Composites (2009)

- Y. Lebour, R. Guider, E. Jordana, J.M. Fedeli, P. Pellegrino, S. Hernandez, B. Garrido, N. Daldosso and L. Pavesi, “High quality coupled ring resonators based on silicon clusters slot waveguide” Group IV Photonics, 5th IEEE International Conference, 17-19 Sept. 2008.

- A. Pitanti, D. Navarro-Urrios, R. Guider, N. Daldosso, L. Khomenkova, F. Gourbilleau, C. Oton, W. Loh, R. Rizk, O. Jambois, B. Garrido and L. Pavesi, “Er3+ coupled to Si nanoclusters rib waveguides”, Group IV Photonics, 5th IEEE International Conference, 17-19 Sept. 2008.

- A. Pitanti, P. Bettotti, E. Rigo, R. Guider, N. Daldosso, J.M. Fedeli and L. Pavesi, “Coupled cavities in one-dimensional photonic crystal based on horizontal slot waveguide structure with Si-nc”, Group IV Photonics, 5th IEEE International Conference, 17-19 Sept. 2008.

- A. Pitanti, D. Navarro-Urrios, R. Guider, N. Daldosso, F. Gourbilleau, L. Khomenkova, R. Rizk and L. Pavesi, “Further improvements in Er3+ coupled to Si nanoclusters rib waveguides”, SPIE Photonic Europe 2008 Proceedings, 4669-44 (2008).

- A. Karakuscu, R. Guider, L. Pavesi and G. D. Sorarù, “Synthesis and Optical Properties of SiC_n/SiO_2 Nanocomposite Thin Films”, 32rd International Conference & Exposition on Advanced Ceramics and Composites (2008)

- O. Anopchenko, P. Bettotti, M. Cazzanelli, N. Daldosso, L. Ferraioli, Z. Gaburro, R. Guider, S. Minhaz, D. Navarro-Urrios, A. Pitanti, S. Prezioso, R. Spano, J. Wang e L. Pavesi, “Nanocristalli di Silicio: potranno permettere una fotonica basata sul Silicio”, FOTONICA 2007, 21-23 May 2007.